The Dissertation Committee for Shen Hu Certifies that this is the approved version of the following dissertation:

Crystalline Perovskite Epitaxial Growth on Germanium (001) by Atomic Layer Deposition

Committee:

John G. Ekerdt, Supervisor

Alexander A. Demkov

Edward T. Yu

Roger T. Bonnecaze

Gyeong S. Hwang

Crystalline Perovskite Epitaxial Growth on Germanium (001) by Atomic Layer Deposition

by

Shen Hu

Dissertation

Presented to the Faculty of the Graduate School of

The University of Texas at Austin

in Partial Fulfillment

of the Requirements

for the Degree of

Doctor of Philosophy

The University of Texas at Austin

December 2017

Dedication

To my beloved family

Acknowledgements

The road to study aboard is a great challenge for me, but I'm extremely fortunate to pursue the Ph.D. study in Dr. Ekerdt's group at University of Texas at Austin. I feel really grateful for so many individuals' support and guidance during my graduate studies. First, I would like to express my most sincere thanks to my advisor, Professor John G. Ekerdt, for his continuous support, encouragement and patience during my whole Ph.D. study. The first thing Dr. Ekerdt taught to me is to be a teacher in my research field. I don't dare to claim that I have been a qualified teacher in this field already but in the past three years I did learn a lot in my research or my life. That memo note he wrote to remind me to challenge everything in the science research has been hanging over my desk ever since and I will always keep that in mind in the future. Ph.D. study is a process of facing new issues and thinking up the solution to solve them. It's a hard journey but really worth the fight. Through the process, I gained my greatest wealth – to learn not to be afraid of issues and also the ability to think independently and execute immediately. And that is all thanks to my advisor who gave me the opportunity and fully supported me.

I would like to have special thanks to Prof. Alexander A. Demkov. He has been much like my co-advisor to support and always give the insightful discussions for my research. I really enjoy the research experience in Materials Physics Lab. I would also like to thank Prof. Edward T. Yu, Prof. Roger T. Bonnecaze, and Prof. Gyeong S. Hwang for their valuable insight and feedback as my dissertation committee members. I'm also extremely grateful for my mentor, Martin D. McDaniel. He guided me through the beginning of my research when I was totally green in this field and patiently trained me for the equipment operation and data analysis. Another special thanks to our lab manager and

brilliant research scientist, Dr. Agham Posadas. Who is also very like my second mentor. His rich knowledge and experience in materials science, vacuum science and equipment maintenance have helped me a lot through my research and he is always happy to answer my numerous questions in detail. Without any one of them, I would definitely have taken many more detours in my Ph.D. study.

I would like to have my special thanks to my friend Zizhou Zhang. We have known each other since we were in Tianjin University. Without his help and encouragement I might not have the chance to study in UT Austin and this wonderful group. The research life in basement office has been a really fun experience with his company. Thanks to Himmi Nallan's numerous suggestions for my atomic deuterium chamber building. He is a very clever and interesting man and I really enjoy the time with him. I won't forget that he is the first man to get me drunk in USA. Also thanks for Pei-Yu Chen's help for the atomic deuterium chamber building. Her brilliant ideas and effort has helped speed up the progress much more. I would also like to give my thanks to every former and current group member, Tuo Wang, Joe M. McCrate, Thong Ngo, Dan Bost, Brad Leonhardt, Wen Liao, Sonali Chopra, Edward Lin, Bryce Edmondson, Brennan M. Coffey, Di Li and Xin Yang for all their support and help! My thanks are also extended to the Materials Physics Lab members including Patrick Ponath, Kristy Kormondy, Elliott Ortmann, Tobias Hadamek, Jackie Kremer, Wei Guo and Marc Reynaud.

Through my research, I'm also glad to have the opportunities to collaborate with several groups. I would like to have my thanks to Prof. David Smith and HsinWei Wu at Arizona State University for their professional transmission electron microscopy images. I would also like to express my special thanks to Li Ji and Heng-Lu Chang from Prof. Edward Yu's research group for their great efforts in electrical measurements. Also thanks

Ali Hamze from Prof. Alexander Demkov's research group for his contribution in density functional theory (DFT) calculations.

I would like to express my thanks to the University of Texas at Austin and the Cockrell School of Engineering for providing me such a great opportunity to pursue my Ph.D. degree. Plenty faculty and staff members in the McKetta Department of Chemical Engineering have given me valuable assistance during my Ph.D. study. I would like to thank Shallaco McDonald, Jason Barborka, Randy Rife, Kevin Haynes, Benjamin Hester, Kate Baird, Jim Smitherman and Laura Mondino. And also thanks to Dr. Steve Swinnea for x-ray diffraction training.

I would like to acknowledge National Science Foundation for funding my Ph.D. research projects (Awards CMMI-1437050, DMR – 10006725 and DMR – 1207342).

Last but not the least, my acknowledgement also goes to my parents and all my friends. It is your love and encouragement that supports me to where I am now.

Crystalline Perovskite Epitaxial Growth on Germanium (001) by Atomic Layer Deposition

Shen Hu, Ph.D.

The University of Texas at Austin, 2017

Supervisor: John G. Ekerdt

Crystalline perovskites (ABO_3) have aroused widespread attention in material science due to their multiple properties. This research uses atomic layer deposition (ALD) to achieve perovskite oxides (ABO_3) deposition on Ge (001) for gate oxide applications in microelectronics devices. In particular, this work is mainly focused on the study of crystalline Sr-based perovskites $SrMO_3$, where M = Ti, Zr, Hf.

In this research work, the mechanism for the initial growth of perovskites on Ge by ALD has been studied. High resolution scanning transmission electron microscopy (STEM) images have shown that both of molecular beam epitaxy (MBE)-grown $BaTiO_3$ films and ALD-grown $SrHfO_3$ films have the same interface structure, which has a 2×1 periodicity and with the alkaline earth metal (AEM) atoms between the Ge dimer rows. This result indicates that the ALD growth proceeds by forming the same Zintl-template layer that is purposely formed in MBE through formation of a 0.5-monolayer (ML) exposure to the AEM. The *in situ* XPS analysis has shown the same surface core level shift (SCLS) behavior results from half-cycle Sr or Ba precursor dosing on a bare Ge (001) surface as is observed following 0.5 -ML Sr or Ba exposure on Ge by MBE. These observations support the conclusion drawn from the STEM images.

Based on the previous study of $SrTiO_3$ (STO) and $SrHfO_3$ (SHO) on Ge (001), there is a trade-off between dielectric constant and leakage current in STO and SHO. This research has also studied $SrHf_xTi_{1-x}O_3$ (SHTO) films with different Hf content *x* to see how composition and lattice constant affected the crystallization behavior. Crystalline $SrZrO_3$ films have also been deposited by ALD on Ge. The C-V and I-V measurements indicate that the $SrZrO_3$ yield the best results for dielectric properties compared to STO, SHO and SHTO. A new combined approach of oxygen plasma pre-treatment, Zintl template formation and atomic deuterium post treatment has been applied on this work to minimize the interface trap density, which has achieved $8.56\times10^{11}cm^{-2}eV^{-1}$.

Table of Contents

List of Tables

List of Figures

Chapter 1: Introduction and overview

1.1. Overview

Over the past decades the increasing speed and lowering power consumption demands in microelectronics chips have been driving forces in complementary metal oxide semiconductor (CMOS) device research. So to satisfy the future developments on higher performance Complementary Metal Oxide Semiconductor (CMOS) devices monolithic integration is investigated herein. Figure 1.1 shows a schematic of a metal-oxide semiconductor field-effect transistor (MOSFET) structure.

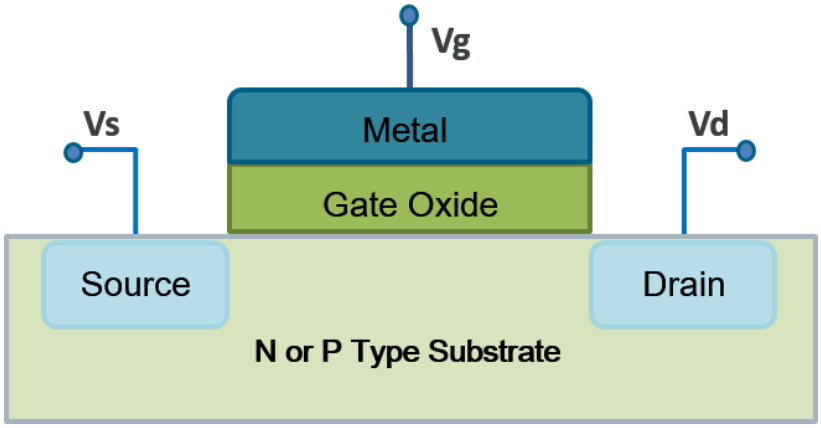

Figure 1.1. Schematic of a MOSFET structure.

In a MOSFET, the saturation drive current (I_{on}) is a critical performance metric.[1] Since the charge component, such as electrons or holes, of I_{on} is dominated by the gate capacitance, better performance transistor requires higher gate capacitance, c, given by:

$$C=\frac{kA\varepsilon}{d}$$

Where c is the gate capacitance, k is the dielectric constant of gate oxide, A is the covered area of the gate oxide, ε is the permittivity of free space and d is the gate thickness. As the transistor feature sizes continue to scale smaller, the traditional gate oxide silica (SiO_2) can no longer be employed due to unacceptably high leakage current in ultrathin (< 1 nm) SiO_2.[2,3] So to achieve higher capacitance and maintain the same or more densely integrated transistors there has been a transition away from the use of SiO_2 to the high dielectric constant k materials to satisfy future developments in CMOS devices.

Besides the high-k materials for gate oxides, the channel materials are also important for transistor performance. Silicon is the most common substrate in the semiconductor industry due to its low cost and the manner by which the gate oxide can be grown. But further transistor scaling requires the channel materials to have higher mobility than Si, which can also lead to a higher driving current.[1,4] Based on the 2012 International Technology Roadmap for Semiconductors (ITRS), channels with high mobility are expected to be introduced by 2018.[5] Compared to Si, the electron and hole mobility for Ge are 3900 vs 1400 cm^2/Vs and 1900 vs 470 cm^2/Vs, respectively, which makes Ge viable to become the next generation channel material.[1,6–8] Additionally, Ge has a more unstable oxide than Si and it's easy to remove the native oxide on Ge to achieve a clean surface.[9–11]

To maintain the advantage of high mobility in the Ge substrate, an interface with a low density of trap states is desired since high interface trap density (D_{it}) could consume the channel mobility.[7] Based on Si studies the significant defects at the oxide-substrate interface result from the substrate roughness and interface dangling bonds.[12] On the Ge-based heterojunctions, the dangling bonds and roughness are also the main cause for high D_{it}.[7,13,14] D_{it} values larger than 10^{12} $cm^{-2}eV^{-1}$ are considered too high for device applications.[1] Thus, an interface with low defects is required for next generation CMOS fabrication.

1.2. RESEARCH BACKGROUND

This research will explore crystalline perovskite deposition on Ge (001) by atomic layer deposition (ALD) as high-*k* gate oxides and will explore how to reduce defects in the oxide and at the interface. The potential for achieving higher dielectric constant in crystalline structures is the reason to study crystalline perovskites instead of amorphous or polycrystalline films.[15]

1.2.1. ATOMIC LAYER DEPOSITION

Thin film growth techniques include chemical vapor deposition (CVD) and physical vapor deposition (PVD), which are chemical process and physical process for thin film deposition, respectively. Developments in CVD led to a more advanced chemical growth technique, ALD. PVD encompasses various delivery methods such as evaporation, sputtering and molecular beam epitaxy (MBE). Among all these thin film growth techniques, ALD has unique characteristics. Compared to CVD, ALD has the advantages of self-limited and conformal coverage on high aspect ratio structures.[16] Compared with MBE, ALD has better thickness uniformity over nonplanar features[17] and can be achieved with a lower thermal budget since the ALD growth window is much lower than the temperatures employed in MBE to facilitate the surface mobility important in MBE-based crystalline growth. And in addition, ALD can have higher deposition rates than MBE and lower equipment cost. As a consequence, ALD is a promising route for high-*k* crystalline oxide growth in semiconductor applications, such as for the Fin Field Effect Transistor (FinFET).

The principle for ALD is indicated in Figure 1.2. The substrate is typically maintained at a constant temperature in the ALD chamber. The metalorganic precursor is delivered into the chamber and absorbs on the substrate surface to achieve saturation, the un-absorbed precursor molecules in gas phase are purged out by the subsequent purge step. Then the second reactant is delivered to react with the absorbed precursor and this step is also followed with a purge step. Thus, one unit cycle of ALD is completed and can be repeated this sequence can achieve the thin film deposition with atomic scale precision (Ångstrom level).[16,18]

Previously, we reported the successful growth of $SrBO_3$ perovskite materials, where B = Ti or Hf, on with Ge by ALD.[14,19,20] However, the mechanism for the initial growth of perovskites on Ge by ALD is not yet understood. One key commonality in the ALD process is that the Sr cyclopentadienyl precursor is dosed first on the clean Ge surface. High–resolution cross-section scanning transmission electron microscopy imaging of molecular beam epitaxy-grown $BaTiO_3$ and atomic layer deposition-grown $SrHf_{0.55}Ti_{0.45}O_3$ reveal a 2×1 periodicity at the interface the alkaline earth metal (AEM) atom between dimer rows.[14,21] Based on this observation, we believe that the initial ALD growth for $SrHf_{0.55}Ti_{0.45}O_3$ on Ge forms out of the same Zintl template as found in MBE growth. To understand the initial interface reactions during perovskite ALD on Ge, we studied the deposition of Sr and Ba molecular precursors on Ge using *in situ* X-ray photoelectron spectroscopy (XPS) and reflection high energy electron diffraction (RHEED) and compare the results with Sr and Ba deposition using Knudsen cells in an MBE system and with density functional theory calculations. This study will be discussed in Chapter 4.

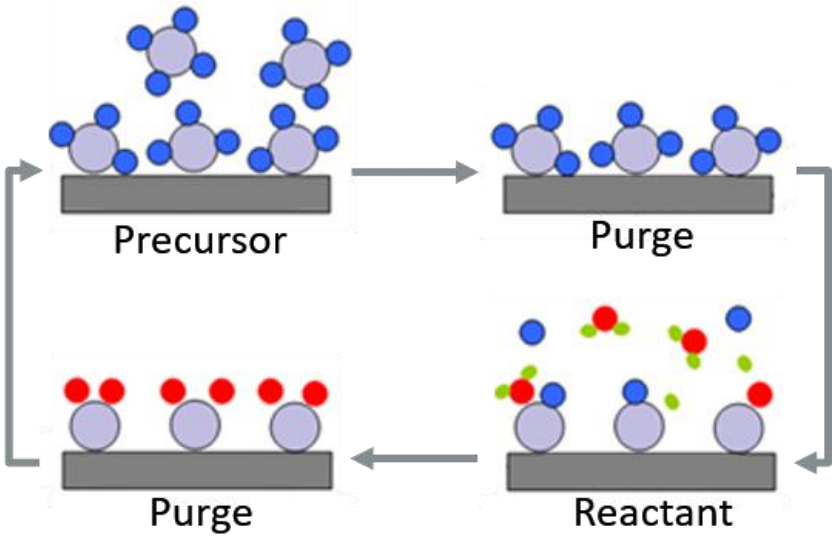

Figure 1.2. Schematic of ALD procedure.

1.2.2. CRYSTALLINE PEROVSKITE FOR HIGH-*K* OXIDES APPLICATION

Crystalline perovskites (ABO_3) have aroused widespread attention in material science due to their multiple properties. Especially, the epitaxial integration of crystalline perovskite oxides on semiconductors presents promising properties for numerous technological applications.[22,23] Replacing the cation A or B in perovskites ABO_3 can lead to different properties of the crystalline perovskite (As shown in Figure 1.3.), which include being high-*k*,[20,24–29] ferromagnetic,[30,31] ferroelectric,[32,33] multiferroic,[34,35] or superconducting[36] materials.

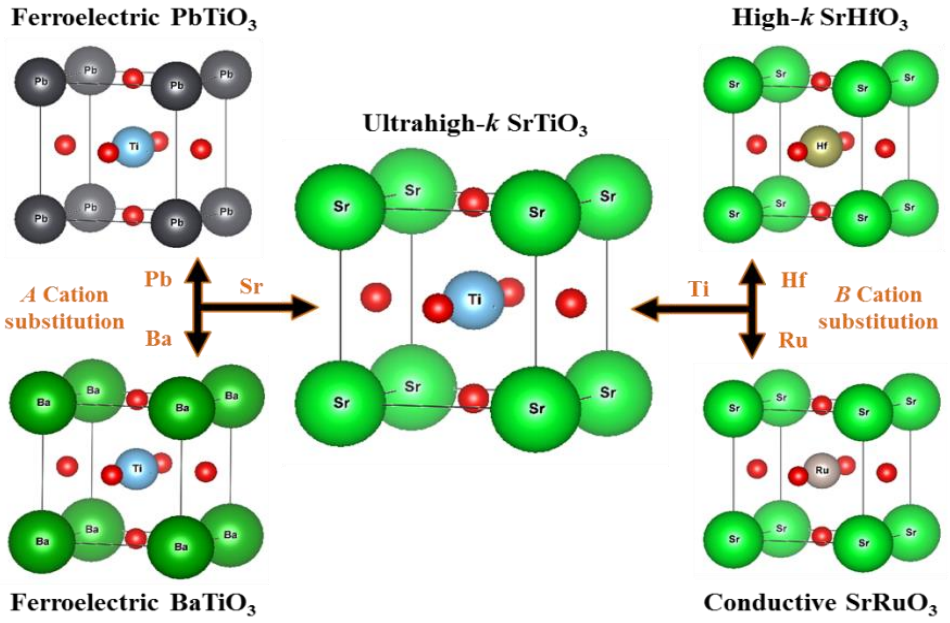

Figure 1.3. The versatility of the perovskite oxide is demonstrated by the simple substitution of the A or B cation. From ultrahigh-k $SrTiO_3$ (center) to ferroelectrics $PbTiO_3$/$BaTiO_3$ (left) and high-*k* $SrHfO_3$ or conductive $SrRuO_3$ (right). Taken from "Atomic layer deposition of perovskite oxides and their epitaxial integration with Si, Ge, and other semiconductors." Applied Physics Reviews 2, 041301 (2015). [37]

After McKee first reported the work of epitaxial growth of $SrTiO_3$ on silicon in 1998, [38] the study of crystalline perovskites on semiconductors has been widely expanded for device applications.[14,20,39–44] These studies include using the crystalline perovskite as a high-*k* gate oxide for field-effect transistor device applications on various semiconductors such as Si, Ge, and GaAs. [24–29,45–50] The *k* value is targeted to be over 12 and preferably 25 to 35 for high dielectric materials.[51]

For crystalline ABO_3 perovskite compound growth, besides the higher mobility reason, Ge (001) may be a preferable substrate to Si (001) due to the lattice match with ABO_3 perovskites. The in-plane atomic spacing on the Ge (001) surface and Si (001)

surface are 3.992 Å and 3.840 Å, respectively.[24–26] Ge (001) will have less lattice strain than Si for a crystalline high-*k* gate stack, like $SrHfO_3$ (lattice constant *a*=4.069 Å), which has -1.9% and -5.6% (compressive) strain on Ge and Si, respectively. For $SrTiO_3$ (*a*=3.905 Å) and the strains are 2.2% and -1.7% Ge and Si, respectively. For $BaTiO_3$ (*a*=4.005 Å), the strains re -0.3% and -4.1%, respectively. Therefore, compared to Si (001), Ge (001) may more readily facilitate crystalline ABO_3 growth.

The previous work in our group has studied the growth of $SHfO_3$ (SHO) and $STiO_3$ (STO) on Ge by ALD.[19,20] Based on these studies, there was a trade-off between the dielectric properties of SHO/Ge and STO/Ge heterojunctions. The dielectric constants for STO and SHO were *k*~90 and *k*~17. The leakage current for STO was around 10 A/cm^2 at 0.7 MV/cm with 0.7 nm equivalent oxide thickness (EOT) and for SHO was 6.3×10^{-6} A/cm^2 at 1.0 MV/cm with EOT=1.0 nm.[19,20] Since the high performance MOSFET requires a high dielectric constant gate oxide and low leakage current, the high-*k* materials that optimize the dielectric properties are required. One approach to tuning the dielectric constant and leakage current is to combine the attributes of STO and SHO through $SrHf_xTi_{1-x}O_3$ growth, by adjusting the Hf content *x* to get the desired dielectric properties. This is presented in Chapter 3. Another idea is to achieve $SrZrO_3$ deposition on Ge (001) by ALD. $SrZrO_3$ has the comparable conduction band offset (CBO) with $SrHfO_3$ on Ge, which are 1.77 eV and 2.17 eV for $SrZrO_3$/Ge and $SrHfO_3$/Ge, respectively, and meanwhile has a higher dielectric constant *k* around 30.[20,55] The $SrZrO_3$/Ge should have better electrical properties, which are expected to be intermediate between STO and SHO. Compare to the reported leakage current versus EOT for gate oxides on Ge (001) in the literature, the $SrZrO_3$/Ge heterojunction is a promising material to improve the performance into the dashed red cycle shown in Figure 1.4. Several groups have studied SZO deposition by molecular beam epitaxy (MBE) or pulse laser deposition (PLD).[24,55,56]

But the $SrZrO_3$ has never been achieved by ALD on Ge. So in this research, we will also study the $SrZrO_3$ deposition on Ge (001) by ALD for high-*k* gate oxide application. This is presented in Chapter 5.

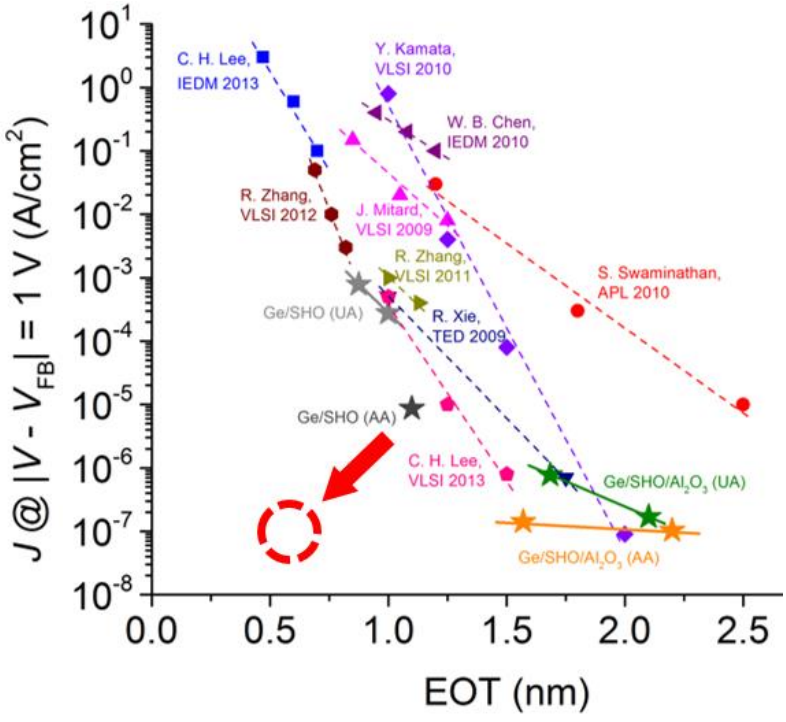

Figure 1.4. Leakage current versus EOT reported as the state of the art in recently reported work of gate oxides on Ge. Taken from "A Low-Leakage Epitaxial High-*k* Gate Oxide for Germanium Metal−Oxide−Semiconductor Devices." *ACS applied materials & interfaces*, 8(8): 5416-5423, (2016). [57]

1.2.3. CHALLENGES OF INTERFACE DEFECTS

Since Ge has higher mobility than Si, which can result in higher drive current $I_{on,}$ this research choose Ge as the substrate. To maintain the advantage of high mobility in Ge substrate, a high quality interface is desired since high interface trap density (D_{it}) could

consume the channel mobility.[7] Previous work in the Ekerdt group found SHO to have D_{it} around 4×10^{13} $cm^{-2}eV^{-1}$.[20,57] The nature of defects at interface of Ge-based heterojunction are mainly formed by dangling bonds[7,13] and the roughness of Ge substrate could also result in the high D_{it}.[12,14] Several groups have employed different methods to degrade the interface trap density,[57–65]such as the air annealing method to reduce the D_{it} of crystalline $SrHfO_3$/Ge to around 2×10^{12} $cm^{-2}eV^{-1}$.[57] Kim's group used La_2O_3-incorporation in HfO_2 dielectrics on Ge and achieved the D_{it} value ~10^{12} $cm^{-2}eV^{-1}$.[58] One of the most widely introduced method is using GeO_x as a passivation layer, which can yield a D_{it} value on the order of lower 10^{11} $cm^{-2}eV^{-1}$.[60,63–67] But this method increases the EOT with the introduction of passivation layer. So herein, a new approach without sacrificing the EOT is studied in this research by introducing atomic deuterium to treat the Ge heterojunction interface.

Takagi's group studied post deposition annealing to treat Al_2O_3/GeO_x/n-Ge in different ambients of N_2, forming gas, H_2, D_2, atomic H and atomic D. Eventually the atomic D treatment led to the best effective electron mobility.[68] So we employed this method to lower the interface trap density in Chapter 5 since dangling bonds in the interface might be another reason to increase the D_{it}.[14] Based on the study of Lyding, D desorption yield is about 50 times lower on Ge than the H yield on Si as shown in Figure 1.5.[69] The similar results should be present at the buried interface in my studies with Ge substrates.

In addition, the previous work showed that high annealing temperature above 650 °C could lead to interfacial reactions, which increase the D_{it}.[20] Ge steps can lead to anti-phase boundary formation in the film. In this research, the SZO is expected to crystalize at lower elevated temperature than SHO to minimize interfacial reactions due to lighter B site atomic weight.[14] New surface treatments for the Ge substrate will be examined in Chapter

5 study the impact of flatter Ge (001) surfaces.[10] Finally atomic deuterium is used to heal dangling bonds at the Ge surface in Chapter 5.

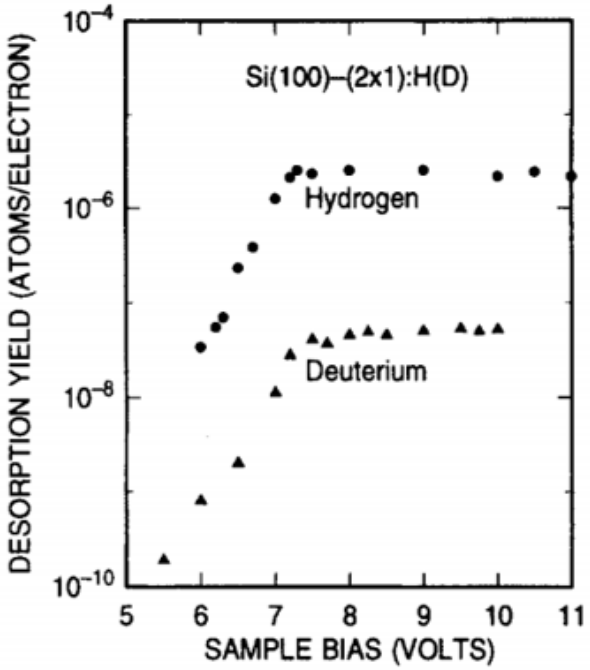

Figure 1.5. Comparison of the STM-induced desorption yields of hydrogen and deuterium from Si(100)-(2×1):H(D) as a function of the sample bias voltage. Taken from "STM-induced H atom desorption from Si (100) isotope effects and site selectivity" *Chemical Physics Letters*, 257 (1) 148-154, (1996).[69]

1.3. RESEARCH OBJECTIVES AND CHAPTER OVERVIEW

The aim of this research is to study the growth of the crystalline Sr-based perovskites $SrBO_3$, where B = Ti, Zr, Hf, on Ge (001) by atomic layer deposition and understand the mechanism for initial ALD growth on Ge (001). In addition, this work will also explore the defect nature of the films and interfaces and achieve favorable dielectric

properties for gate oxide applications in microelectronics devices. Particularly, the specific objectives of this research in each chapter are listed as follows:

Chapter 2 introduces about the specific equipment used in this research. A commercial MBE, a home-built hot wall ALD chamber and a commercial x-ray photoelectron spectroscopy analyzer are combined within on system, which allows us to achieve *in situ* deposition and characterization by X-ray photoelectron spectroscopy (XPS). A home-designed atomic deuterium chamber is also attached on this system for *in situ* post treatment. The experimental procedure will also be discussed, especially the conditions for film deposition by ALD and other *ex situ* characterization methods such as x-ray reflectivity (XRR), x-ray diffraction (XRD), aberration-corrected scanning transmission electron microscopy (STEM), capacitance-voltage (C-V), and current-voltage (I-V) measurements.

Chapter 3 discusses the growth of crystalline $SrHf_xTi_{1-x}O_3$ (SHTO) films on Ge (001) substrates by atomic layer deposition. Samples were prepared with different Hf content x to explore if strain, from tensile (x = 0) to compressive (x = 1), affects film crystallization temperature and how composition affects properties. Amorphous films grow at 225 °C and are crystallized into epitaxial layers at annealing temperatures that varied monotonically with composition from ∼530 °C (x = 0) to ∼660 °C (x = 1). Transmission electron microscopy reveals abrupt interfaces. Electrical measurements reveal 0.1 A/cm^2 leakage current at 1 MV/cm and dielectric constant of 30 for x = 0.55. This work indicates that the SHTO can combine the superiorities of STO and SHO, and adjusts the dielectric properties by changing the Hf content x but it still exhibits higher leakage current than expected for CMOS application.

Chapter 4 presents the study of the initial growth of ABO_3 perovskites on Ge (001) by atomic layer deposition, where A = Ba, Sr and B = Ti, Hf, Zr, and compares the behavior

with a MBE-grown template – chemically and structurally – to understand the mechanism(s) for crystalline ABO_3 growth by ALD on Ge (001). Via *in situ* X-ray photoelectron spectroscopy (XPS), reflection high-energy electron diffraction (RHEED) and density functional theory (DFT), we analyzes the surface core level shifts and surface structure during the initial growth of ABO_3 perovskites on Ge (001) by ALD. We find that the initial dosing of the barium- or strontium- bis(triisopropylcyclopentadienyl) precursors on a clean Ge surface produces a surface phase that has the same chemical and structural properties as the 0.5-monolayer Ba Zintl layer formed when depositing Ba by MBE. Similar binding energy shifts are found for Ba, Sr and Ge when using either chemical or elemental metal sources. The observed germanium surface core level shifts are consistent with the flattening of the initially tilted Ge surface dimers using both molecular and atomic metal sources. Similar binding energy shifts and changes in dimer tilting with alkaline earth metal adsorption are found with density functional theory calculations. High angle angular dark field scanning transmission microscopy images of $BaTiO_3$, $SrZrO_3$, $SrHfO_3$ and $SrHf_{0.55}Ti_{0.45}O_3$ reveal the location of the Ba (or Sr) atomic columns between the Ge dimers. The results imply that the organic ligands dissociate from the precursor after precursor adsorption on the Ge surface, producing the same Zintl template critical for perovskite growth on Group IV semiconductors during molecular beam epitaxy. This work also indicates that using the MBE-grown Zintl template for ALD growth can prevent surface carbon contamination, which could possibly lower the defects at the interface.

Chapter 5 studies $SrZrO_3$ growth on both bare Ge (001) and Zintl template by ALD, and explores variables such as the growth temperature, cycle ratio etc. This work is based on the study in the previous two chapters and demonstrates that $SrZrO_3$ may be the best option for high-*k* dielectric application in the crystalline perovskite group of $SrBO_3$, where B is the element (Ti, Zr and Hf). The $SrZrO_3$/Ge heterojunction has the comparable

conduction band offset (CBO) with $SrHfO_3$ on Ge, which are 1.77 eV and 2.17 eV for $SrZrO_3$ and $SrHfO_3$ on Ge, respectively, and meanwhile also higher dielectric constant *k* around 30. On the other hand, since $SrZrO_3$ can achieve crystallization at lower temperature at ~590 °C than $SrHfO_3$ (650 °C), it's easier to have better crystallinity in $SrZrO_3$ and little interface reaction, which could result in lower interface defects. Several new methods including Zintl template preparation, oxygen plasma pre-treatment and atomic deuterium post treatment are applied to reduce the interface trap density. MOSCAP devices are fabricated based on selective samples for electrical characterization and interface trap density measurement. The electrical properties for $SrZrO_3$/Ge heterojunction in this work are reported as 30 dielectric constant and leakage current of 2.14×10^{-8} A/cm^2 at 1 MV/cm with an EOT = 0.8 nm. The best D_{it} for treated sample is eventually obtained as 8.56×10^{11}cm^{-2}eV^{-1}. The work reports the deposition of crystalline $SrZrO_3$ on Ge (001) by ALD for the first time and applies a new strategy to minimize the D_{it} value.

1.4. REFERENCE

1 P. S. Goley and M. K. Hudait, Materials **7**, 2301 (2014).

2 D. A. Muller, T. Sorsch, S. Moccio, F. H. Baumann, K. Evans-Lutterodt, and G. Timp, Nature **399**, 758 (1999).

3 R. Chau, S. Datta, M. Doczy, J. Kavalieros, and M. Metz, in Ext. Abstr. Int. Workshop Gate Insul. IEEE Cat No03EX765, pp. 124–126 (2003).

4 M. Kobayashi, J. Mitard, T. Irisawa, T. Hoffmann, M. Meuris, K. Saraswat, Y. Nishi, and M. Heyns, IEEE Trans. Electron Devices **58**, 384 (2011).

5 International Roadmap for Semiconductors (2012 Edition).

6 D. P. Brunco, B. D. Jaeger, G. Eneman, A. Satta, V. Terzieva, L. Souriau, F. E. Leys, G. Pourtois, M. Houssa, K. Opsomer, G. Nicholas, M. Meuris, and M. Heyns, ECS Trans. **11**, 479 (2007).

7 R. Pillarisetty, Nature **479**, 324 (2011).

8 E. Simoen, J. Mitard, G. Hellings, G. Eneman, B. De Jaeger, L. Witters, B. Vincent, R. Loo, A. Delabie, S. Sioncke, M. Caymax, and C. Claeys, Mater. Sci. Semicond. Process. **15**, 588 (2012).

9 X.-J. Zhang, G. Xue, A. Agarwal, R. Tsu, M.-A. Hasan, J. E. Greene, and A. Rockett, J. Vac. Sci. Technol. A **11**, 2553 (1993).

10 P. Ponath, A. B. Posadas, R. C. Hatch, and A. A. Demkov, J. Vac. Sci. Technol. B **31**, 031201 (2013).

11 J. Oh and J.C. Campbell, J. Electron. Mater. **33**, 364 (2004).

12 S. Mohsenifar, M.H. Shahrokhabadi, S. Mohsenifar, and M. H. Shahrokhabadi, Microelectron. Solid State Electron. **4**, 12 (2015).

13 S. Baldovino, A. Molle, and M. Fanciulli, Appl. Phys. Lett. **93**, 242105 (2008).

14 S. Hu, M.D. McDaniel, A. Posadas, C. Hu, H. Wu, E.T. Yu, D.J. Smith, A.A. Demkov, and J.G. Ekerdt, MRS Commun. **6**, 125 (2016).

15 A. I. Kingon, J.-P. Maria, and S. K. Streiffer, Nature **406**, 1032 (2000).

16 S. M. George, Chem. Rev. **110**, 111 (2010).

17 J. Provine and M. Rincon, NNIN ALD Road Show (2012).

18 M. Leskelä and M. Ritala, Thin Solid Films **409**, 138 (2002).

19 M. D. McDaniel, T. Q. Ngo, A. Posadas, C. Hu, S. Lu, D. J. Smith, E. T. Yu, A. A. Demkov, and J. G. Ekerdt, Adv. Mater. Interfaces **1**, 1400081 (2014).

20 M. D. McDaniel, C. Hu, S. Lu, T. Q. Ngo, A. Posadas, A. Jiang, D. J. Smith, E. T. Yu, A. A. Demkov, and J. G. Ekerdt, J. Appl. Phys. **117**, 054101 (2015).

21 K. D. Fredrickson, P. Ponath, A. B. Posadas, M. R. McCartney, T. Aoki, D. J. Smith, and A. A. Demkov, Appl. Phys. Lett. **104**, 242908 (2014).

22 A. A. Demkov and A. B. Posadas, Integration of Functional Oxides with Semiconductors (Springer, 2014).

23 N. Setter, D. Damjanovic, L. Eng, G. Fox, S. Gevorgian, S. Hong, A. Kingon, H. Kohlstedt, N.Y. Park, G.B. Stephenson, I. Stolitchnov, A.K. Taganstev, D.V. Taylor, T. Yamada, and S. Streiffer, J. Appl. Phys. **100**, 051606 (2006).

24 M. Jahangir-Moghadam, K. Ahmadi-Majlan, X. Shen, T. Droubay, M. Bowden, M. Chrysler, D. Su, S. A. Chambers, and J. H. Ngai, Adv. Mater. Interfaces **2**, 1400497 (2015).

25 R. A. McKee, F. J. Walker, and M. F. Chisholm, Science **293**, 468 (2001).

26 J. W. Reiner, A. M. Kolpak, Y. Segal, K. F. Garrity, S. Ismail-Beigi, C. H. Ahn, and F. J. Walker, Adv. Mater. **22**, 2919 (2010).

27 Z. Yu, Y. Liang, C. Overgaard, X. Hu, J. Curless, H. Li, Y. Wei, B. Craigo, D. Jordan, R. Droopad, J. Finder, K. Eisenbeiser, D. Marshall, K. Moore, J. Kulik, and P. Fejes, Thin Solid Films **462**–**463**, 51 (2004).

28 R. Droopad, Z. Yu, H. Li, Y. Liang, C. Overgaard, A. Demkov, X. Zhang, K. Moore, K. Eisenbeiser, M. Hu, J. Curless, and J. Finder, J. Cryst. Growth **251**, 638 (2003).

29 M. Sousa, C. Rossel, C. Marchiori, H. Siegwart, D. Caimi, J.-P. Locquet, D.J. Webb, R. Germann, J. Fompeyrine, K. Babich, J.W. Seo, and C. Dieker, J. Appl. Phys. **102**, 104103 (2007).

30 J.-G. Cheng, J.-S. Zhou, J.B. Goodenough, and C.-Q. Jin, Phys. Rev. B **85**, 184430 (2012).

31 G. H. Jonker and J. H. Van Santen, Physica **19**, 120 (1953).

32 C. H. Ahn, K. M. Rabe, and J.-M. Triscone, Science **303**, 488 (2004).

33 N. Nuraje and K. Su, Nanoscale **5**, 8752 (2013).

34 G. Catalan and J. F. Scott, Adv. Mater. **21**, 2463 (2009).

35 S. Dong and J.-M. Liu, Mod. Phys. Lett. B **26**, 1230004 (2012).

36 J. G. Bednorz and K. A. Müller, Rev. Mod. Phys. **60**, 585 (1988).

37 M. D. McDaniel, T. Q. Ngo, S. Hu, A. Posadas, A. A. Demkov, and J. G. Ekerdt, Appl. Phys. Rev. **2**, 041301 (2015).

38 R. A. Mckee, F. J. Walker, and M. F. Chisholm, Phys. Rev. Lett. **81**, 3014 (1998).

39 K. Kukli, M. Ritala, T. Sajavaara, T. Hänninen, and M. Leskelä, Thin Solid Films **500**, 322 (2006).

40 L. Ji, M. D. McDaniel, S. Wang, A. B. Posadas, X. Li, H. Huang, J. C. Lee, A. A. Demkov, A. J. Bard, J. G. Ekerdt, and E. T. Yu, Nat. Nanotechnol. **10**, 84 (2015).

41 Y. Guo, K. Suzuki, K. Nishizawa, T. Miki, and K. Kato, J. Cryst. Growth **284**, 190 (2005).

42 Y. Shichi, S. Tanimoto, T. Goto, K. Kuroiwa, and Y. Tarui, Jpn. J. Appl. Phys. **33**, 5172 (1994).

43 Y. Chu, L. W. Martin, M. B. Holcomb, M. Gajek, S. Han, Q. He, N. Balke, C. Yang, D. Lee, W. Hu, Q. Zhan, P. Yang, A. Fraile-rodríguez, A. Scholl, S.X. Wang, and R. Ramesh, Nat. Mater. Lond. **7**, 478 (2008).

44 M. Okuyama and Y. Hamakawa, Ferroelectrics **63**, 243 (1985).

45 J. W. Reiner, A. Posadas, M. Wang, M. Sidorov, Z. Krivokapic, F. J. Walker, T. P. Ma, and C. H. Ahn, J. Appl. Phys. **105**, 124501 (2009).

46 A. A. Demkov, A. B. Posadas, H. Seo, M. Choi, K. J. Kormondy, P. Ponath, R. C. Hatch, M. D. McDaniel, T. Q. Ngo, and J. G. Ekerdt, ECS Trans. **54**, 255 (2013).

47 M. P. Warusawithana, C. Cen, C. R. Sleasman, J. C. Woicik, Y. Li, L. F. Kourkoutis, J. A. Klug, H. Li, P. Ryan, L.-P. Wang, M. Bedzyk, D. A. Muller, L.-Q. Chen, J. Levy, and D. G. Schlom, Science **324**, 367 (2009).

48 S.-H. Baek and C.-B. Eom, Acta Mater. **61**, 2734 (2013).

49 V. Vaithyanathan, J. Lettieri, W. Tian, A. Sharan, A. Vasudevarao, Y. L. Li, A. Kochhar, H. Ma, J. Levy, P. Zschack, J. C. Woicik, L. Q. Chen, V. Gopalan, and D. G. Schlom, J. Appl. Phys. **100**, 024108 (2006).

50 Y. Liang, J. Kulik, T. C. Eschrich, R. Droopad, Z. Yu, and P. Maniar, Appl. Phys. Lett. **85**, 1217 (2004).

51 J. Robertson and R.M. Wallace, Mater. Sci. Eng. R Rep. **88**, 1 (2015).

52 A. S. Cooper, Acta Cryst **Vol: 15**, (1962).

53 M. E. Straumanis and E. Z. Aka, J. Appl. Phys. **23**, 330 (1952).

54 Y. Okada and Y. Tokumaru, J. Appl. Phys. **56**, 314 (1984).

55 M. Yang, W. S. Deng, Q. Chen, Y. P. Feng, L. M. Wong, J. W. Chai, J. S. Pan, S. J. Wang, and C. M. Ng, Appl. Surf. Sci. **256**, 4850 (2010).

56 Z. H. Lim, K. Ahmadi-Majlan, E. D. Grimley, Y. Du, M. Bowden, R. Moghadam, J. M. LeBeau, S. A. Chambers, and J. H. Ngai, J. Appl. Phys. **122**, 084102 (2017).

57 C. Hu, M. D. McDaniel, A. Jiang, A. Posadas, A. A. Demkov, J. G. Ekerdt, and E. T. Yu, ACS Appl. Mater. Interfaces **8**, 5416 (2016).

58 I. Oh, M.-K. Kim, J. Lee, C.-W. Lee, C. Lansalot-Matras, W. Noh, J. Park, A. Noori, D. Thompson, S. Chu, W. J. Maeng, and H. Kim, Appl. Surf. Sci. **287**, 349 (2013).

59 S. Swaminathan, M. Shandalov, Y. Oshima, and P. C. McIntyre, Appl. Phys. Lett. **96**, 082904 (2010).

60 R. Xie, T. H. Phung, W. He, M. Yu, and C. Zhu, IEEE Trans. Electron Devices **56**, 1330 (2009).

61 M. Caymax, M. Houssa, G. Pourtois, F. Bellenger, K. Martens, A. Delabie, and S. Van Elshocht, Appl. Surf. Sci. **254**, 6094 (2008).

62 K. Kita, T. Takahashi, H. Nomura, S. Suzuki, T. Nishimura, and A. Toriumi, Appl. Surf. Sci. **254**, 6100 (2008).

63 C. H. Lee, C. Lu, T. Tabata, W. F. Zhang, T. Nishimura, K. Nagashio, and A. Toriumi, Electron Devices Meet. IEDM 2013 IEEE Int. p. 2.5.1-2.5.4 (2013).

64 R. Zhang, P. C. Huang, N. Taoka, M. Takenaka, and S. Takagi, Symp. VLSI Technol. VLSIT, pp. 161–162 (2012).

65 C. H. Lee, C. Lu, T. Tabata, T. Nishimura, K. Nagashio, and A. Toriumi, Symp. VLSI Technol. VLSIT, pp. T28–T29 (2013).

66 H. Matsubara, T. Sasada, M. Takenaka, and S. Takagi, Appl. Phys. Lett. **93**, 032104 (2008).

67 A. Delabie, F. Bellenger, M. Houssa, T. Conard, S. Van Elshocht, M. Caymax, M. Heyns, and M. Meuris, Appl. Phys. Lett. **91**, 082904 (2007).

68 R. Zhang, J.C. Lin, X. Yu, M. Takenaka, and S. Takagi, Symp. VLSI Technol., pp. T26–T27 (2013).

69 P. Avouris, R. E. Walkup, A. R. Rossi, T.-C. Shen, G. C. Abeln, J. R. Tucker, and J. W. Lyding, Chem. Phys. Lett. **257**, 148 (1996).

Chapter 2: Research methodology

2.1. Research Facilities

The majority of experiments are conducted on the equipment in Materials Physics Laboratory. This equipment shown in Figure 2.1 combines the custom-built ALD reactor with a commercial MBE system (DCA 600) and an X-ray photoelectron spectroscopy (XPS) analysis chamber (VG Scienta R3000).[1] In addition, a home-built atomic deuterium chamber (D-chamber) is also attached to the system for *in situ* treatment.

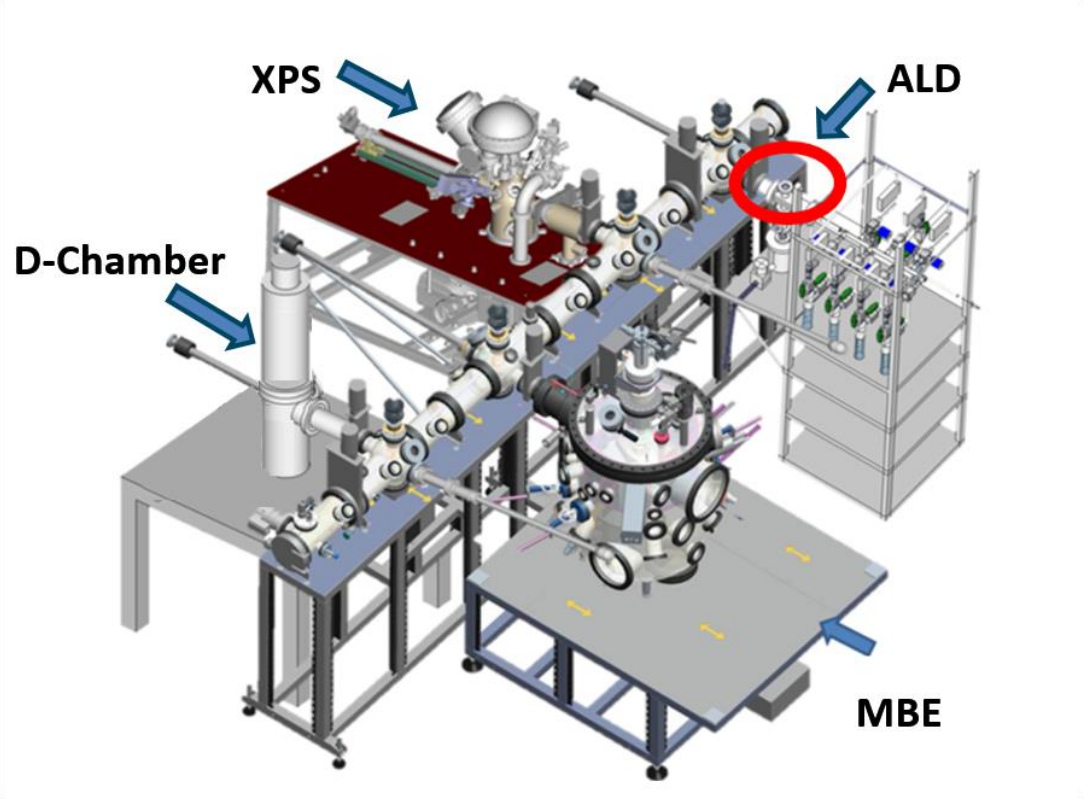

Figure 2.1. Schematic of the research facilities

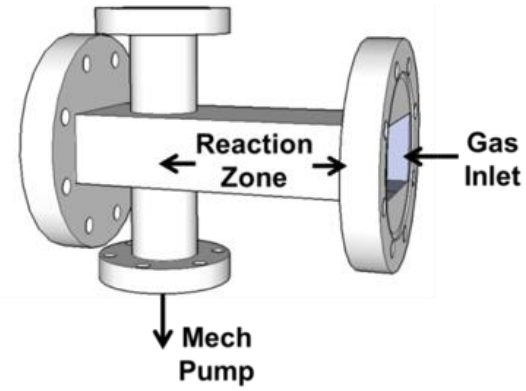

Figure 2.2. Perspective drawing of the ALD chamber.[1]

In situ XPS was performed with a monochromatic Al Kα source at 1486.6 eV using a VG Scienta R3000 electron energy analyzer. The analyzer was calibrated with a clean Ag foil such that the Ag $3d_{5/2}$ core level is at a binding energy of 368.28 eV. The XPS analysis chamber can also perform the low energy ion-scattering spectroscopy (LEISS) measurement. The MBE is equipped with six effusion cells (four standard and two high-temperature), a four-pocket electron beam evaporator, a quartz crystal microbalance (QCM), a reflective high energy electron diffraction (RHEED, Staib Instruments operating at 21 keV) system and a radio frequency plasma source of both oxygen and nitrogen. The QCM can calibrate the flux rate. The RHEED enables the observation of post deposition annealing process in real time. The plasma source can be applied for sample treatment before and after the growth. The ALD consists of eight ports for precursor and H_2O reactant saturators, a manifold equipped with ALD valves from Swagelok and mass flow controllers for each ports and a custom-built, hot wall stainless steel chamber for deposition. The ALD chamber is rectangular with the length of 20 cm and volume of 460 cm^3 (as shown in Figure 2.2).

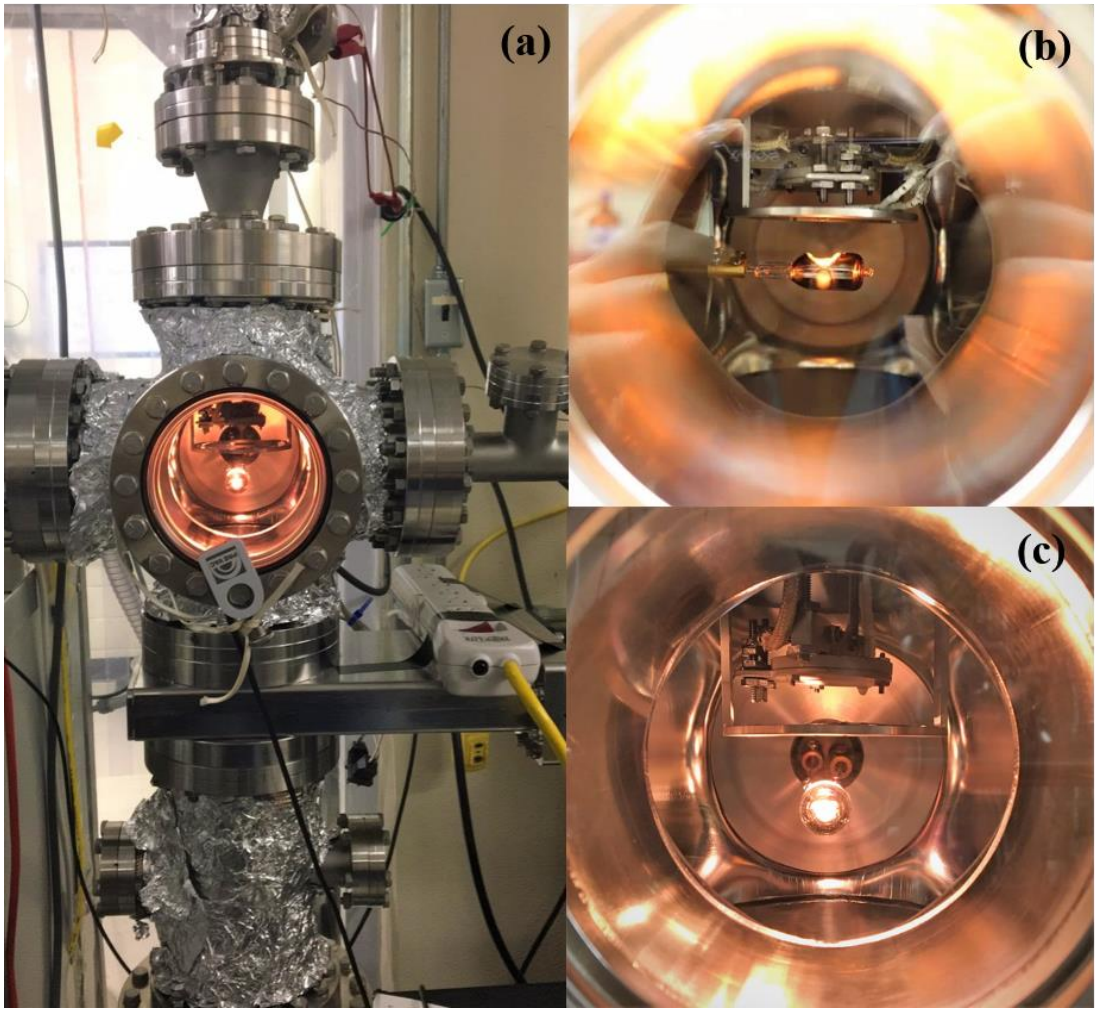

Figure 2.3. (a) Image of atomic deuterium chamber (D-chamber), (b) inside side view and (c) inside front view of the D-chamber.

The last portion for the system is the home-built D-chamber. As shown in Figure 2.3.(a), a six-cross chamber is used to combine the heater from the top, a tungsten filament from the back, a transfer arm for sample insertion and removal from the right and the turbo pump at the bottom. The left side is attached to the main system to enable transfer sample in vacuum for *in situ* treatment. Figure 2.3.(b) and (c) indicate the heater-sample-filament arrangement. For *in situ* treatment the distance from heater to sample is around 2 cm and

sample to filament is around 4 cm. The heater, which is supplied from Momentive Performance Materials, is made of pyrolytic boron nitride (PBN). The resistance for the heater at room temperature is measured to be 9.8-13.5 ohms. The maximum power and current allowed for the heater are 663 W and 12 A, respectively. The heater position is fixed above the sample grabber as shown in Figure 2.4.(b). The grabber is connected to a linear motion as shown in Figure 2.4.(a) to enable grabber movement in the vertical direction. For sample treatment, the distance from the heater to grabber is kept at 2 cm so that radiation can heat the sample to ~350°C when heater temperature set as 450°C with the filament on.

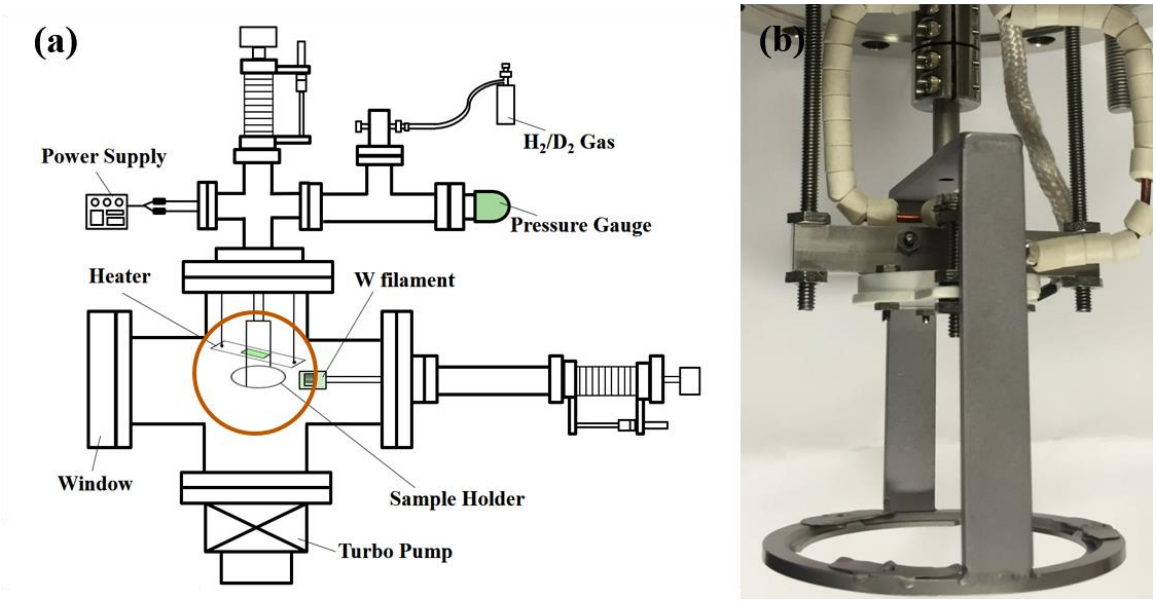

Figure 2.4. Schematic of the D-chamber (a) and (b) the image of heater and sample grabber, which corresponds to the cycle region in (a).

The tungsten filament is also connected to a linear motion manipulator so that it can be translated in the horizontal direction and it is positioned at 4 cm below the sample when exposing the sample to atomic deuterium (as shown in Figure 2.4.(a)). The tungsten filament is a 400 W Osram Xenophot bulb, which has part of the glass enclosure removed to expose the filament. A current of 5.2 A was supplied by a DC power supply (KEPCO, MSK10-10M) to the tungsten filament and produces a temperature above 1800 K, which was calibrated by a thermal pyrometer. At this temperature, the tungsten filament could crack deuterium molecule to generate atomic deuterium.[2] The pressure of introduced deuterium gas (99.999%; Matheson) is controlled by a leak valve and monitored by a 943 Model cold cathode gauge from MKS instrument to maintain at 5.0×10^{-6} torr in the chamber. The flux of atomic deuterium is estimated around 2×10^{13} D/cm^2·s based on previous work.[3]

2.2. GENERAL EXPERIMENT METHOD

The Ge (001) substrate is prepared from a 4-inch Ge wafer (Sb-doped, ρ~0.04 Ω-cm) from MTI Corp. as described previously.[4–6] The as-received Ge wafer is diced into approximately 18×20 mm^2 pieces, degreased with acetone, isopropyl alcohol and water, dried and then two methods are introduced to remove the carbon from the surface. The first one is to expose the sample to ultraviolet light/ozone to remove residual carbon. The other treatment involves transferring the sample into the MBE chamber followed by the oxygen plasma treatment. The surface GeO_2 is removed by annealing at 700 °C in vacuum (< 2×10^{-9} Torr) for 1 hr. The resulting 2×1-reconstructed Ge (001) surface is verified by *in situ* RHEED. The clean Ge (001) sample is transferred *in vacuo* to an XPS chamber to verify the Ge surface composition. Following this characterization, the sample is then transferred

in situ and exposed to varying doses of elemental Sr and Ba in the MBE chamber, or exposed to the metal precursors or for perovskite film deposition in the ALD chamber.

For elemental deposition in the MBE chamber the substrate is maintained at 600 °C following protocols in previous reports.[1,7] The Ba and Sr fluxes are calibrated with a quartz crystal monitor to a rate of approximately 1 ML/min, allowing for controlled submonolayer dosing. Coverages of Ba or Sr are reported in ML equivalents for MBE-dosed samples, where a ML is defined to be the atomic density of the Ge (001) unreconstructed surface (6.26×10^{14} atoms/cm^2). RHEED is used to monitor surface structure *in situ* and in real time. The MBE-dosed samples is cooled to 200 °C before transferring the sample into the XPS analysis chamber.

For deposition in the ALD chamber the sample is maintained at 225 °C, the typical temperature used for $BaTiO_3$, $SrHfO_3$ and $SrTiO_3$ growth.[4,5,8] The precursors and conditions used for this study are listed in Table 2.1. H_2O is used as the oxygen source at room temperature. The ALD chamber is maintained at a total pressure of 1 Torr using Ar carrier gas during dosing and less than 1×10^{-6} Torr when in standby mode. An ALD half-cycle refers to a 2-s exposure to the precursor stream followed by a 20-s Ar purge (referred to as 1 half-cycle herein). A complete cycle refers to a 2-s precursor exposure, 20-s argon purge, 2-s deionized water exposure, and another 20-s argon purge (referred to as 1 cycle herein). The ALD-dosed samples are transferred out of the ALD chamber without cooling the sample and subsequently cooled to room temperature in the transfer line.

For the SZO growth by ALD, to achieve the slightly Sr rich in grown film, the cycle ratio needs to be adjusted as Sr: Zr = 2:3. The quaternary SHTO oxides growth is more complicated, which is accomplished by adjusting the number of *m* SHO subcycles (Sr: Hf=1:1) and *n* STO (Sr:Ti=2:1) subcycles to vary the Hf content (*x*) in SHTO. Different film thickness is controlled by the total number of supercycles *l*.

Table 2.1. ALD precursors for each element

Element	Precursor name	Temperature/ ℃	Vendor
Sr	Strontium Bis(triisopropylcyclopentadienyl)	130	Air Liquide
Ba	Barium Bis(triisopropylcyclopentadienyl)	150	
Ti	Titanium tetraisopropoxide	40	Sigma-Aldrich
Zr	Tetrakis (dimethylamido) Zirconium (IV)	60	
Hf	Hafnium formamidinate	115	Dow Chemical

2.3. *EX SITU* CHARACTERIZATION

Based on the previous experiments,[4,5] the films can be amorphous as grown, so post-deposition annealing is required to obtain the single crystalline film. The RHEED is used to observe transformation from amorphous to crystalline in real time and XPS is used to analyze the composition and the elemental oxidation states in the grown films and at the interfaces. For *ex situ* characterization, the film thickness is measured by X-ray reflectivity (XRR) and crystallinity is analyzed by X-ray diffraction (XRD) and rocking curve on a Rigaku Ultima IV system with a Cu Kα source. The aberration-corrected scanning transmission electron microscopy (STEM) is employed here to investigate the grown film and interface. The samples are prepared via standard cross-section method with Ar ion milling and STEM images are taken with a JEOL ARM 200F operated at 200 kV. The STEM analysis work is performed by our collaborator Dr. David J. Smith at Arizona State University.

To study the electrical properties, which include dielectric constant *k*, leakage current *I* and interface trap density D_{it}, samples are selected to fabricate the MOS capacitor

structures and the capacitance-voltage (C-V) and current-voltage (I-V) measurements are performed on an Agilent B1500A semiconductor device parameter analyzer with a Cascade Microtech probe station. The electrical measurements are a collaboration with Dr. Edward Yu's group in the ECE department at UT. Some theoretical modeling is also introduced to support this research and this part is assisted by Dr. Alexander A Demkov in Physics department at UT. My primary focus is centered on the ALD growth, materials characterization, the building of atomic deteurium source chamber, and collaboration with other research groups for the theoretical modeling and device testing.

2.4. REFERENCES

1 M. D. McDaniel, A. Posadas, T. Wang, A. A. Demkov, and J. G. Ekerdt, Thin Solid Films **520**, 6525 (2012).

2 U. Bischler and E. Bertel, J. Vac. Sci. Technol. Vac. Surf. Films **11**, 458 (1993).

3 J. M. McCrate and J. G. Ekerdt, Chem. Mater. **26**, 2166 (2014).

4 M. D. McDaniel, T. Q. Ngo, A. Posadas, C. Hu, S. Lu, D. J. Smith, E. T. Yu, A. A. Demkov, and J. G. Ekerdt, Adv. Mater. Interfaces **1**, 1400081 (2014).

5 M. D. McDaniel, C. Hu, S. Lu, T. Q. Ngo, A. Posadas, A. Jiang, D. J. Smith, E. T. Yu, A. A. Demkov, and J. G. Ekerdt, J. Appl. Phys. **117**, 054101 (2015).

6 S. Hu, M. D. McDaniel, A. Posadas, C. Hu, H. Wu, E. T. Yu, D.J. Smith, A. A. Demkov, and J. G. Ekerdt, MRS Commun. **6**, 125 (2016).

7 M. Choi, A. Posadas, R. Dargis, C.-K. Shih, A. A. Demkov, D. H. Triyoso, N. D. Theodore, C. Dubourdieu, J. Bruley, and J. Jordan-Sweet, J. Appl. Phys. **111**, 064112 (2012).

8 T. Q. Ngo, A. B. Posadas, M. D. McDaniel, C. Hu, J. Bruley, E. T. Yu, A. A. Demkov, and J. G. Ekerdt, Appl. Phys. Lett. **104**, 082910 (2014).

Chapter 3: Monolithic Integration of Perovskites on Ge(001) by Atomic Layer Deposition: A Case Study with $SrHf_xTi_{1-x}O_3$

3.1. INTRODUCTION

As the transistor feature sizes continue to scale ever smaller there has been a transition away from the use of conventional materials for the channel, Si, and the gate oxide, SiO^2.[1]Germanium has electron and hole mobility of 3900 and 1900 cm^2/Vs, respectively, compared to 1400 and 470 cm^2/Vs at 300 K, respectively, in Si. For this reason, Ge is being considered for p-type metal-oxide semiconductor field effect transistors (MOSFET).[1,2] There are multiple considerations in selecting a gate oxide material including the dielectric constant, band offset, leakage current, interface trap density (D_{it}), and ease of manufacturing.[3,4] Various groups have reported gate oxides on Ge in MOSFETs, including TiO_2/Al_2O_3, ZrO_2, $LaAlO_3$ on an interfacial layer of $SrGe_x$, HfO_2 on an interfacial layer of Y_2O_3-doped GeO_2, Y_2O_3 on a GeO_x interfacial layer, and HfO_2 with Al_2O_3 to suppress HfO_2-GeO_x intermixing.[5–10]

Amorphous oxides generally have lower dielectric constants than the crystalline form. However, the absence of grain boundaries in amorphous films is a potential advantage as grain boundaries can serve as defect trap sites.[11] Crystalline oxides have been reported on silicon[12–14] and germanium.[13,15] These crystalline oxides on semiconductors (COS) can offer high dielectric constants, perfection of the crystal structure at the oxide/semiconductor interface, and the possibility to coherently bond across the interface and minimize dangling bonds.[12,13,16] Many COS examples are for oxides grown using molecular beam epitaxy (MBE). We recently reported an all-chemical growth process for

S. Hu, M. D. McDaniel, A. Posadas, C. Hu, H. Wu, E. T. Yu, D. J. Smith, A. A. Demkov, and J.G. Ekerdt, MRS Commun. 6, 125 (2016).
Comments: I designed and conducted the experiment.

$SrTiO_3$ (STO) and $SrHfO_3$ (SHO) on Ge (001) using atomic layer deposition (ALD) that illustrates a potentially scalable integration route to crystalline oxides on germanium.[17,18]

SHO has a large band gap of 6.1 eV with favorable conduction band offset (~2.2 eV) and valence band offset (~3.2 eV) with Ge.[19,20] This is in contrast with Ti-based perovskites, where the Ti 3d states yield negligible conduction band offsets with Si and Ge (~0.1–0.5 eV).[21–23] Incorporation of Hf into the alloy provides an upward shift of the d-states, which improves the conduction band offset, and increases the lattice constant, which may affect epitaxy. The dielectric constants were k~90 and k~20 for thin films of STO and SHO, respectively. Capacitor structures showed the leakage current for STO was around 10 A/cm^2 at 0.7 MV/cm with equivalent oxide thickness (EOT) of 0.7 nm and the leakage current for SHO was less than 10^{-5} A/cm^2 at 1.0 MV/cm with EOT of 1.0 nm.[17,18] In the previous studies amorphous films were deposited during ALD and the crystalline films formed after annealing at temperatures from 530 to 660 °C. The present study was undertaken to explore the role of strain on the crystallization temperature and composition on the film properties by growing alloys of $SrHf_xTi_{1-x}O_3$ (SHTO) by ALD on Ge (001). The lattice constants of 3.905 Å and 4.069 Å for bulk STO and SHO, respectively, lead to 2.2% and -1.9% strain with the Ge (001) substrate for fully-strained, commensurate films affording a composition for which the lattice constant will match Ge (001) surface spacing along the [110] direction.

3.2. EXPERIMENT

The Ge substrates (18×20 mm^2) are diced from a 4-in Ge wafer (n-type, Sb-doped, 0.029-0.054 Ω·cm resistivity from MTI Corp.) The sample preparation procedure and experimental system are described in previous work.[17,18] The wafer pieces are cleaned with

acetone, isopropyl alcohol and deionized water in an ultrasonic bath for 10 min each. After drying with nitrogen the sample is exposed to UV/ozone for 30 min to remove residual carbon contamination. The sample is mounted on a molybdenum puck and loaded into the vacuum system immediately and transferred to a molecular beam epitaxy (MBE) chamber. The sample is annealed and deoxidized in vacuum ($<2\times10^{-9}$ Torr) by heating from 200 to 500 °C at 20 °C min^{-1} and then from 550 to 650 °C at 10 °C min^{-1}, annealed at 650 °C for 1 hr, and finally cooled to 200 °C at 30 °C min^{-1}. This procedure produces the 2×1-reconstructed clean Ge (001) surface, which is essential as the starting surface for perovskite ALD.[17,18] *In situ* reflection high-energy electron diffraction (RHEED) is used to verify the surface order. Figure 3.1 shows a representative surface after this procedure.

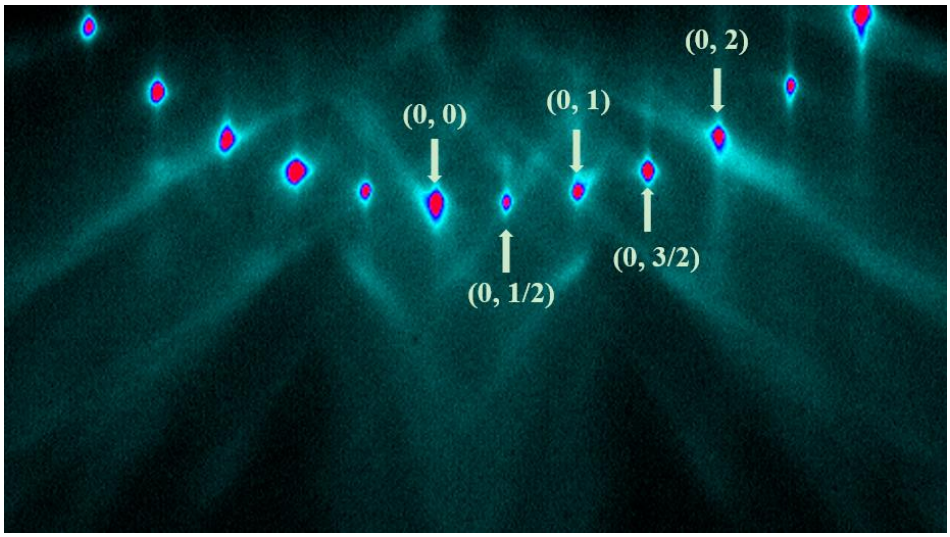

Figure 3.1. After 1 hr vacuum annealing at 650 °C, the Ge 2×1 reconstructed surface is observed by RHEED. The Kikuchi lines indicate the surface cleanliness and good long range order of the substrate, which are important for ALD growth on Ge (001). Image taken along the <110> direction.

The Ge substrate with the 2×1-reconstructed surface is transferred *in situ* to the ALD chamber,[24] where it is allowed to equilibrate for ~15 min at the growth temperature of 225 °C. Film growth is performed at 1 torr using strontium bis(triisopropylcyclopentadienyl) [$Sr(^{i}Pr_3Cp)_2$] (HyperSr), hafnium formamidinate [$Hf(fmd)_4$] (Hf-FAMD), titanium tetraisopropoxide [$Ti(O\text{-}^{i}Pr)_4$] (TTIP), and water as the co-reactant (oxygen source) is H_2O.[17,18] The Sr, Hf, and Ti precursors were heated to 130, 115 and 40 °C, respectively. The quaternary compound was grown using the dosing and purging times indicated in Figure 3.2. For each metalorganic precursor, a 2-s dose time saturates the surface;[17,18] the co-reactant water is dosed for 1 s. Following each precursor or water dose, a 15-s Ar purge is required. Our previous work showed that excess Sr was required to initiate the growth of STO on Ge. For this reason the Sr:Ti cycle ratio is 2:1[18] and we adopted that protocol herein. Similarly, SHO growth on Ge used a Sr:Hf cycle ratio of 1:1 and that was used herein.[17] The cycle ratios in Figure 3.2 produce SHTO films that are slightly Sr-rich (Sr/(Sr+Hf+Ti)) and a 1:1 (Sr:Ti+Hf) film requires some of the Sr:Ti cycle ratios to be 1:1 rather than 2:1. The quaternary $SrHf_xTi_{1-x}O_3$ oxide was grown by adjusting the number of *m* SHO subcycles and *n* STO subcycles to vary the Hf content (*x*). Different film thickness is controlled by the total number of supercycles *l*.

Sr-------2s (Sr) / 15s (Ar) / 1s (H_2O) / 15s (Ar) × 1
Hf-------2s (Hf) / 15s (Ar) / 1s (H_2O) / 15s (Ar)× 1 } × *m*
Sr-------2s (Sr) / 15s (Ar) / 1s (H_2O) / 15s (Ar) × 2
Ti-------2s (Ti) / 15s (Ar) / 1s (H_2O) / 15s (Ar) × 1 } × *n*
} × *l*

Figure 3.2. Schematic of the growth method for $SrHf_xTi_{1-x}O_3$ films by ALD. The subcycles *m* for SHO and *n* for STO are adjusted to realize different Hf content *x*. Different film thicknesses were realized by adjusting the number of *l* supercycles.

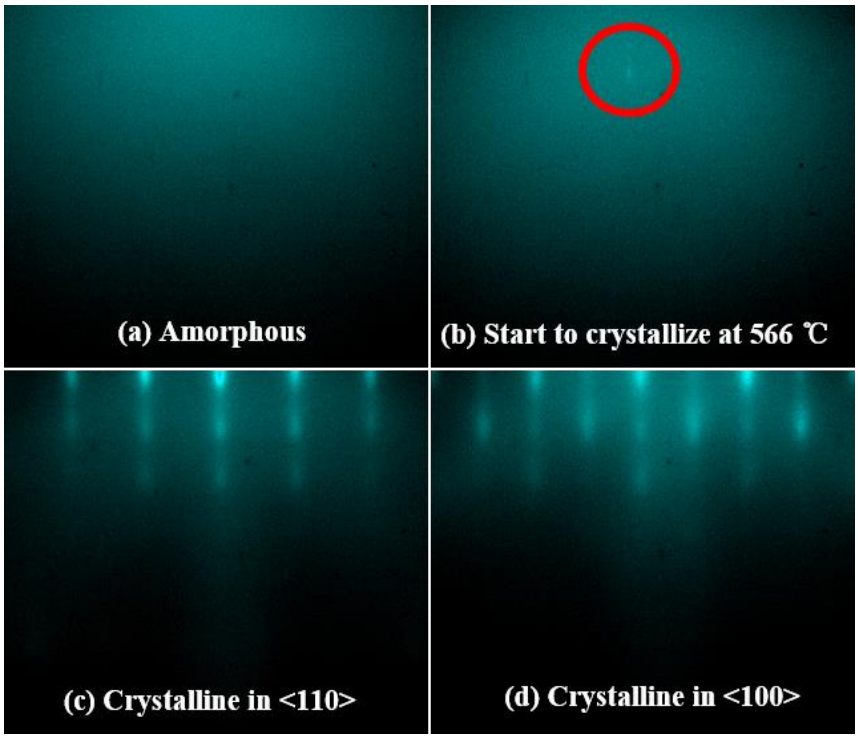

Figure 3.3. RHEED images for an 11.4-nm $SrHf_{0.34}Ti_{0.66}O_3$ film showing (a) the as-grown amorphous film, (b) the first pattern spot appearing at 568 °C, and (c) and (d) images were taken at 200 °C following annealing at 588 °C for 5 min. The beam was aligned along <110> and <100> directions for (c) and (d), respectively. This film was grown with a m:n =1:1 subcycle ratio and l=20 supercycles.

Following ALD growth, the sample is transferred back to the MBE chamber and annealed while monitoring the surface in real time with RHEED to follow the transformation from amorphous to crystalline. The substrate is heated from 200 to 500 °C with a 20 °C min^{-1} ramp rate, followed by a ramp rate of 10 °C min^{-1} as the temperature is increased further. Figure 3.3 shows a representative transformation for an 11.4-nm $SrHf_{0.34}Ti_{0.66}O_3$ film. The temperature at which spots in the RHEED pattern emerge is monitored and this is referred to as the crystallization temperature. The temperature is then increased by 20 °C and held at this as annealing temperature for 5 min to fully crystallize

the sample. The sample is then cooled to 200 °C at 30 °C min^{-1} and transferred from the MBE chamber.

The films were characterized by *in situ* x-ray photoelectron spectroscopy (XPS) to analyze the composition and uniformity using monochromatic Al Kα source at 1486.6 eV and a VG Scienta R3000 analyzer, which is calibrated by a silver foil. High-resolution spectra are measured five times and summed up for the Sr (3*d*, 3*p*) Ti 2*p*, O 1*s*, C 1*s*, Hf 4*f* and Ge 3*d* features. The measurement settings were 50 meV steps with 157 ms/step dwell time and 100 eV pass energy with a 0.4 mm analyzer slit width, which resulted in 350 meV effective resolution. The stoichiometry and Hf content *x*, which is defined as the ratio of Hf to (Hf+Ti), for the $SrHf_xTi_{1-x}O_3$ films are calculated by the integrated area of the Sr 3*d*, Ti 2*p* and Hf 4*f* peaks. The atomic sensitivity factors (ASF) for Sr 3*d*, Ti 2*p* and Hf 4*f* are set as 1.843, 2.001 and 2.639, respectively.[25]

The thickness and crystallinity of the SHTO films were measured by x-ray reflectivity (XRR) and x-ray diffraction (XRD) on a Rigaku Ultima IV system with a Cu Kα source. The interface of selected samples was examined by cross-sectional transmission electron microscopy (TEM). The samples were prepared via standard cross-section method with Ar ion milling. Aberration-corrected scanning transmission electron microscopy (STEM) was used for further interface study. The TEM images were taken with a JEOL 2010F and STEM images were taken with a JEOL ARM 200F. Electron-energy-loss spectroscopy (EELS) composition mapping was also applied to investigate the elemental distributions in the growth direction.

Electrical properties (dielectric constant *k* and leakage current *I*) were established for some samples by fabricating standard metal oxide semiconductor capacitor (MOS capacitor) structures. The films had a top electrode of TaN applied by sputtering and 15 μm photolithographic features were defined with a SF6-based plasma etch. After building

up the MOS capacitor structure the back side of the wafer was scratched and silver paste was applied to form the bottom electrode. The capacitance-voltage (C-V) and current-voltage (I-V) measurements were performed on an Agilent B1500A semiconductor device parameter analyzer with a Cascade Microtech probe station.

3.3. Results and Discussion

3.3.1. Deposition and crystallization of $SHf_xTi_{1-x}O_3$ films

Films with Hf content x distributed from 0 to 1 and with thickness between 8.0 to 14.0 nm were grown. SHTO films were deposited with subcycle ratios (Figure 3.2.) m:n from 1:3 to 7:1. STO (x = 0) and SHO (x = 1) films were deposited with around 100 cycles producing films that were 9.7 and 12.6 nm thick, respectively. SHTO films were grown with a total of $l\times(2m+3n)$ cycles as the composition was varied.

The XRD and rocking curve measurements confirmed the crystallization that was indicated by RHEED. Figure 3.4 shows the θ-2θ XRD and rocking curve around the film (002) reflection at 2θ = 45.45±0.5° for a film with a composition of $SrHf_{0.47}Ti_{0.53}O_3$. This sample was grown with a $m:n$=2:1 subcycle ratio and l=14 supercycles. The crystallization temperature was found to be 612 °C. *Ex situ* XRR measurement indicates the thickness is 13.9 nm. The (002) reflection at 2θ = 45.45±0.5 leads to an out-of-plane lattice constant of c = 3.989±0.005 Å. The rocking curve scan around the SHTO (002) reflection reveals a full-width half-maximum (FWHM) of 1.3°. The best quality STO and SHO films grown by ALD had FWHM of 0.8° and 1.2°, respectively.[17,18]

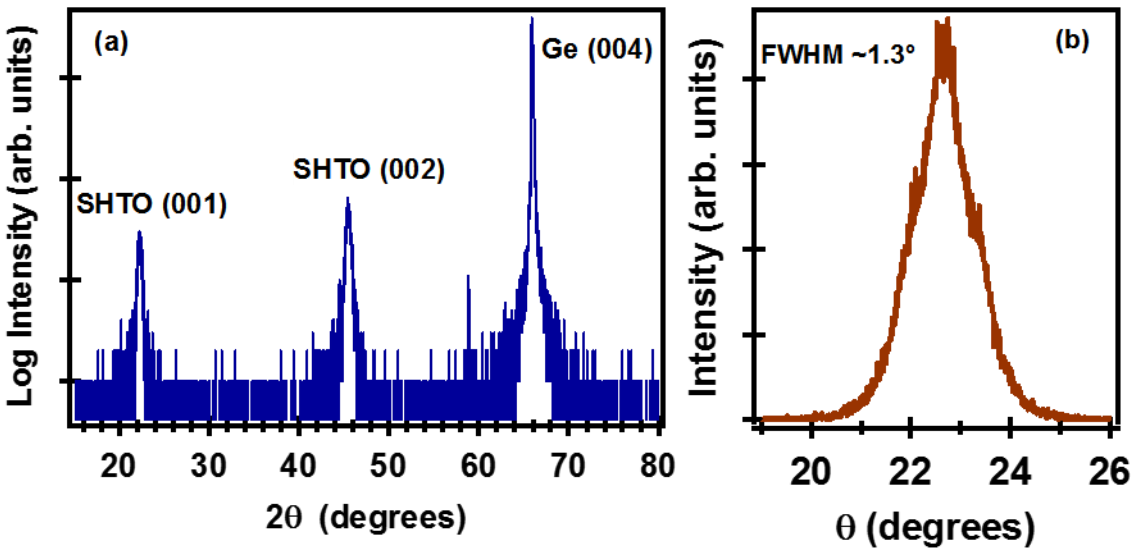

Figure 3.4. X-ray diffraction pattern (a), and rocking curve (b), for 13.9-nm $SrHf_xTi_{1-x}O_3$ (x=0.47) film grown on Ge by ALD, and annealed at 632℃ for 5 minutes in vacuum. The peak of the SHTO (002) reflection is at 2θ = 45.45±0.5° and the rocking curve for the (002) reflection has a full width at half maximum (FWHM) of 1.3°.

Figure 3.5.(a) illustrates that the temperature for crystallization onset increases monotonically with increasing Hf content from 510 °C for STO to 640 °C for SHO. The bulk lattice constants for SHO and STO are 4.069 Å and 3.905 Å, respectively. By assuming SHTO forms a substitutional alloy, and by applying Vegard's law the bulk SHTO lattice constants (a) can be estimated as a function of x and these are represented by the red line in Figure 3.5.(b). From Ge surface spacing of 3.992 Å along the <110> direction we compute the in-plane strain that should result from a fully-strained, commensurate film at room temperature and present this as the green line in Figure 3.5.(b). The fully-strained films vary from tensile (2.2 % for x = 0) to compressive (-1.9 % for x = 1). At room temperature a value of x~0.53 should give zero strain.

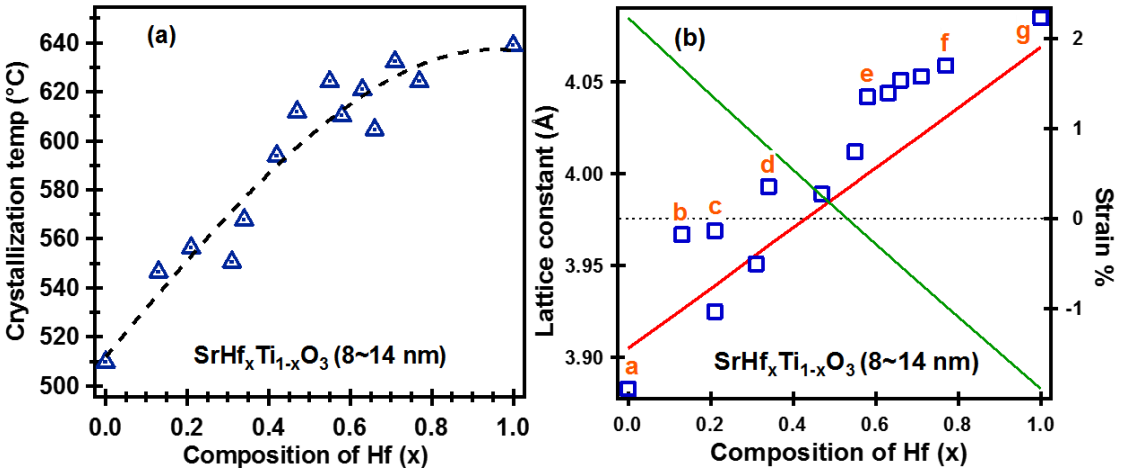

Figure 3.5. (a) Crystallization temperature T versus Hf content x for 8- to 14-nm thick $SrHf_xTi_{1-x}O_3$ films. The dashed line is drawn to guide the eye. (b) Predicted dependence of the bulk lattice constant and strain with Hf content x at room temperature. The red line indicates the cubic lattice constant a of bulk $SrHf_xTi_{1-x}O_3$ based on Vegard's law. The green line presents the strain for commensurate and fully-strained SHTO films on Ge. The squares are the experimental out-of-plane lattice constants c for different x; the squares with letters indicate that samples with Sr-rich compositions of around 55% and other squares indicate samples for which the Sr composition varied from 49% to 51%.

The coefficient of thermal expansion for Ge is approximately one order of magnitude less than a composition averaged value for SHTO alloys;[26–28] over the 500-650 °C annealing window the x-value that matches the Ge separation distance decreases from x~0.4 to x~0.3. We sought to determine how interface strain influenced crystallization. The monotonically increasing crystallization temperature with x (Figure 3.5.(a)) suggests that the annealing temperature does not depend on the strain between the substrate and the SHTO alloy but is rather dependent on the atomic mass of the elements that comprise the alloy. Since the atomic mass of Hf is much heavier than Ti, it will require more thermal energy to move Hf to the correct location of the perovskite structure to crystallize compared to Ti, similar to what has been found for A-site cations in ATiO3 perovskites.[29]

Both Sr-rich or Sr-lean stoichiometry in STO films grown on STO produced an out-of-plane lattice constant that was greater than expected for a fully strained film.[30] The SHTO out-of-plane lattice constants c are determined from the (002) XRD reflections and are also presented in Figure 3.5.(b). In general the experimental *c*-values are greater than *a* for compressive films and less than *a* for tensile films, consistent with expectations for commensurate films. However, squares with letters in Figure 3.5.(b) correspond to samples that have Sr-enrichment around 55% and could be expected to have out-of-plane lattice constants that are greater than fully-strained stoichiometric films. A fully-strained stoichiometric STO film on Ge should have an out-of-plane lattice constant of 3.852 Å at room temperature based on a Poisson ratio for STO of 0.232.[31] The experimental STO value (Square (a) in Figure 3.5.(b)) is 3.883 Å due to Sr-enrichment. Similarly Squares (b), (c) and (d) correspond to samples with out-of-plane lattice constants that are greater than the bulk, cubic lattice constant. Whereas, films with similar compositions as (b), (c) and (d), which should be under tension if fully strained, display out-of-plane lattice constants less than *a*.

3.3.2. *IN SITU* XPS STUDY AND COMPOSITION UNIFORMITY

In situ XPS was performed on the SHTO films before and after annealing. Figure 3.6 presents results for a $SrHf_{0.56}Ti_{0.44}O_3$ film grown with an *m:n*= 3:1 subcycle ratio and *l* = 11 supercycles. This film started to crystallize at 633 °C had an out-of-plane lattice constant of 4.04 Å. Figures 3.6.(a)-(e) present the Sr 3*d*, Ti 2*p*, O 1*s*, C 1*s* + Sr 3*p* and Hf 4*f* core levels, respectively. The Sr $3d_{3/2}$ and $3d_{5/2}$ peaks are located at binding energies of 135.5 eV and 133.8 eV, respectively, which indicates that the Sr is fully oxidized (Sr^{2+}) in the SHTO film.[32] Similarly, the Ti 2*p* and Hf 4*f* features in Figures 3.6.(b) and (e),

respectively, correspond to fully oxidized Ti (Ti^{4+}) and Hf (Hf^{4+}). Figure 3.6.(d) shows that there is no carbon peak at the C 1*s* position of 285 eV.

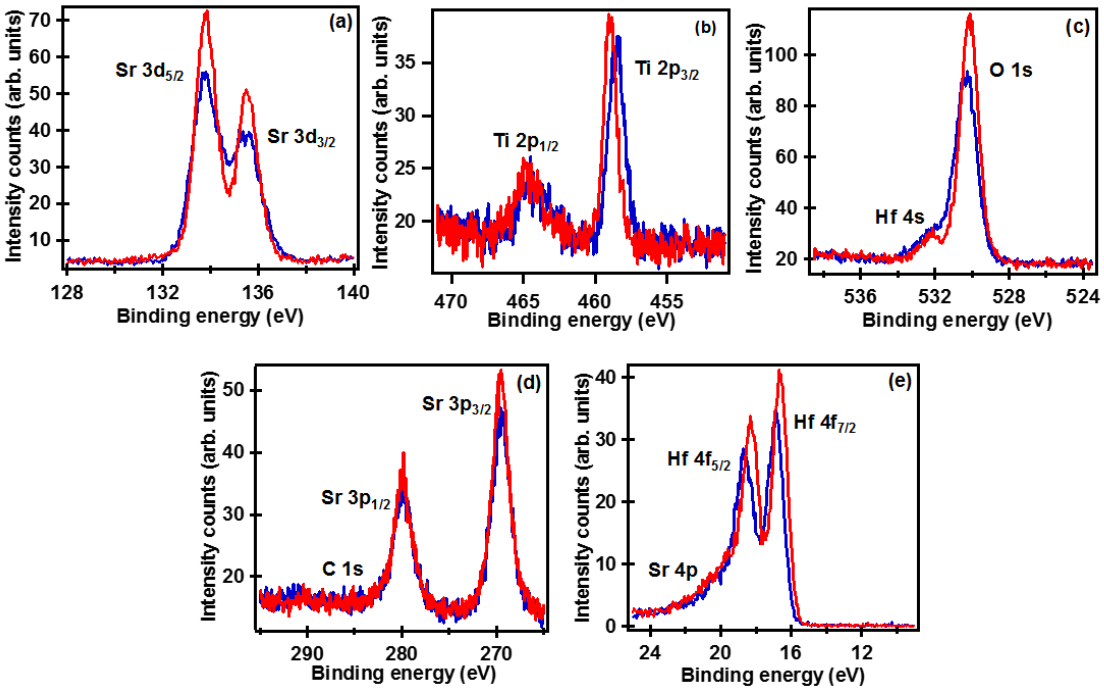

Figure 3.6. X-ray photoelectron spectra for Sr 3*d* (a), Ti 2*p* (b), O 1*s* (c), C 1*s* and Sr 3*p* (d) and Hf 4*f* (e) in a $SrHf_xTi_{1-x}O_3$ (x=0.56) film grown by ALD on Ge (001). The blue line in each figure corresponds to the spectrum post-deposition annealing and the red line corresponds to the spectrum after annealing at 654 °C for 5 min.

The Hf content x = 0.56 and stoichiometry are determined by integrating the areas of the Sr 3*d*, Ti 2*p* and Hf 4*f* features. The Sr:(Hf+Ti) ratios for films in this study reveal a stoichiometry that is consistent with an ABO_3 perovskite. Previous work in our group has shown that slightly Sr-rich films (i.e., A-rich) crystallize more readily on Ge (001) than B-rich films.[17,18] The Sr composition (viz., Sr/(Sr+Hf+Ti)) of all crystallized films falls in the range from 50% to 56%. Some films outside this range, such as 47% Sr. are still observed to crystallize. However, the RHEED images for such films (not shown) suggest rough

surfaces and imply lower crystalline quality. The sample in Figure 3.6 has the ratio of A:B of 55:45. The value of x = 0.56 for a m:n = 3:1 subcycle ratio suggests that Ti is more readily incorporated into the SHTO alloy during ALD.

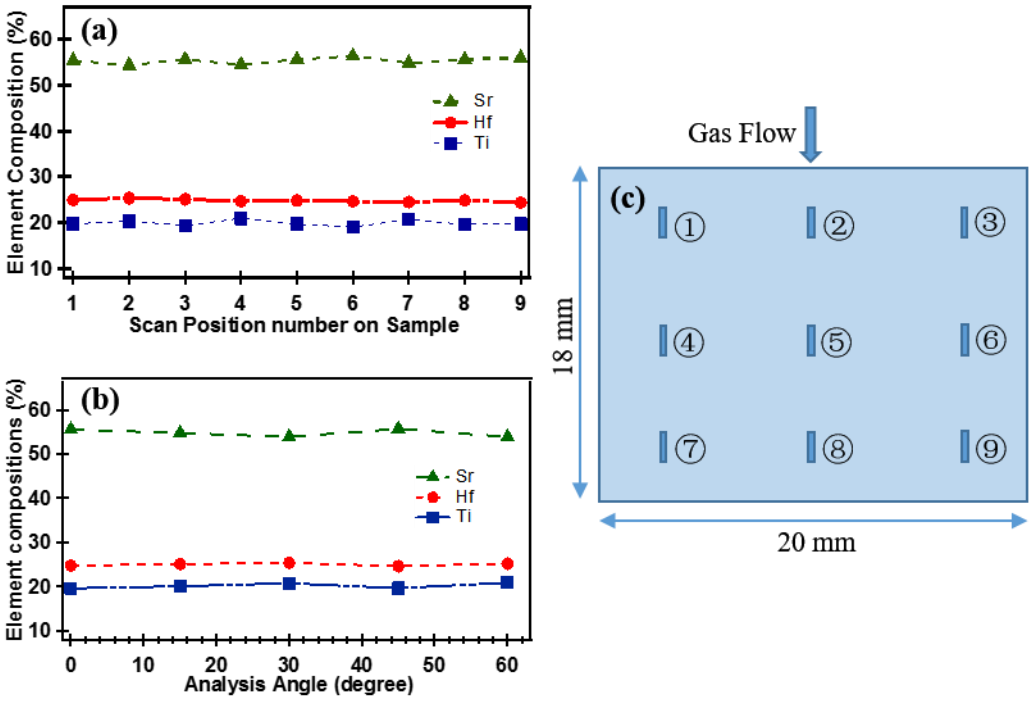

Figure 3.7. (a) XPS position analysis and (b) angle-resolved XPS at location Number 5 for the $SrHf_{0.56}Ti_{0.44}O_3$ film after annealing 654 °C. (c) Schematic showing the sampling points and orientation in the ALD chamber for the 18×20 mm^2 Ge substrate. The Numbers 1 to 9 denote different XPS sampling points; an area of 3×1 mm^2 is probed at each sample point. The Sr, Hf and Ti compositions are 55.3±1.0 %, 24.8±0.5% and 20.0±1.0%, respectively, for the nine positions. The analysis angles in (b) of 0, 15, 30, 45 and 60° correspond to sampling depths of 6.2, 6,0, 5.4, 4.4 and 3.1 nm, respectively. For all the AR-XPS scans, the Sr, Hf and Ti compositions have ranges of 54.8±0.9 %, 25.0±0.6% and 20.3±0.6%, respectively.

Compositional uniformity across the Ge substrates and throughout the films was probed with XPS. Figure 3.7 presents results for the film discussed in Figure 3.6 after

annealing at 653 °C for 5 min. The composition is uniform across the film and constant with gas flow direction, as would be expected for an ALD process. Angle-resolved XPS (AR-XPS) was performed at wafer position Number 5 to examine uniformity of the composition through the thickness of the film. Based on the universal escape depth curve[33] we estimate nearly 97% of the signal comes from a depth of no more than ~6.2 nm from the SHTO surface when the sample is fixed on the horizontal plane (*i.e.*, 0°). The analysis angles (Figure 3.7.(b) of 0, 15, 30, 45 and 60° correspond to sampling depths of 6.2, 6,0, 5.4, 4.4 and 3.1 nm, respectively. For the AR-XPS scans that sampled depths of 6.2 to 3.1 nm from the free surface, the Sr, Hf and Ti compositions were 54.8±0.9%, 25.0±0.6% and 20.3±0.6%, respectively, confirming the composition uniformity with depth of the film.

3.3.3. MICROSTRUCTURE

Previous work in our group showed that annealing temperature affected the interface trap density of SHO films. Films annealed at less than 650 °C retained an abrupt Ge-SHO interface. SHO annealed at 700 °C and 750 °C resulted in an interfacial layer evidenced by Ge XPS features that are suggestive of a hafnium germanide and a noncrystalline layer at the SHO-Ge interface.[17] TEM and HAADF analysis was performed on a 14-nm $SrHf_{0.55}Ti_{0.45}O_3$ sample which was grown with subcycle ratio *m:n*= 3:1, supercycle *l*=11 but Sr:Ti=1:1 in subcycle *n* so that it had lower Sr composition that is 49%. A film with good thickness uniformity and surface smoothness is visible in Figure 3.8.(a). Figures 3.8.(b) and (c) show high-angle annular-dark-field (HAADF) STEM images of the SHTO-Ge interface and Figure 3.9 shows enlargements from selected regions in Figure 3.8.(c). An abrupt interface without an obvious interfacial layer is found when the SHTO was annealed at 645 °C, which is consistent with previous work.[17] EELS

composition mapping was performed to investigate the element distribution across the interface. The EELS data presented in Figure 3.10 indicate that there is no interdiffusion across the Ge-SHTO interface and that the SHTO composition is spatially uniform.

Local grain tilting is apparent in Figure 3.8.(b). The solid lines *mn* and *nl* represent the Hf/Ti plane adjacent to the Ge (001) surface and the dotted line is an extension of line *mn*. The included angle indicates a local crystal tilt near the Ge surface of ~2.2°. Grain tilting can be caused by several factors, including lattice mismatch and the resulting film strain.[34,35] The $SrHf_{0.55}Ti_{0.45}O_3$ film is expected to be under compressive strain through the crystallization and cooling steps since $SrHf_{0.55}Ti_{0.45}O_3$ will have about -0.1 % compressive strain at room temperature (Figure 3.5.(b)). During the transformation from amorphous into a crystalline film, nucleation likely occurs at the Ge-SHTO interface to produce the epitaxial film. The presence of a stepped surface with a step height of ~5.658/4 = 1.414 Å, as visible in Figure 3.8.(b) and Region 1 in Figure 3.8.(c), will impact the lateral area over which an epitaxial crystalline domain can grow before it encounters a step that is not commensurate with the SHTO step height.

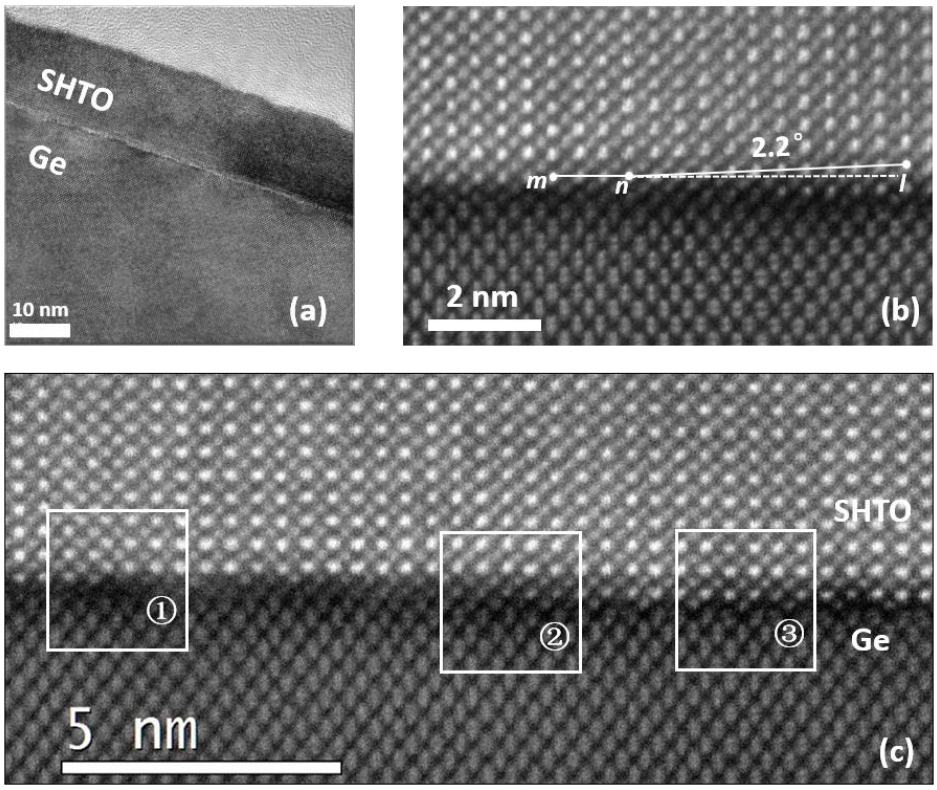

Figure 3.8. Transmission electron micrographs of 14.0-nm $SrHf_{0.55}Ti_{0.45}O_3$ with post-deposition annealing at 645℃ for 5 minutes: (a) TEM image showing the cross-sectional view of the SHTO film, (b) and (c) high-resolution HAADF STEM images showing details of the SHTO-Ge interface. In figure (b), the full lines *mn* and *nl* indicate the Hf/Ti plane, the dotted line is the extension of *mn*. The included angle between *nl* and the dotted line is ~2.2°. Regions ①, ② and ③ in Figure (c) are selected for further analysis in Figure 3.9.

An antiphase boundary (APB) is visible in Region 1 of Figure 3.8.(c) as illustrated in the enlargements in Figures 3.9.(a) and (c). One possible reason is that crystallites initiated on adjacent Ge regions extend laterally to intersect above the surface step leading to APB formation in the crystalline film.[36] The Ge columns near the APB in Figure 3.9.(a) and (c) are misaligned with the Hf/Ti columns and some unbonded (to Sr) Ge is visible at the interface, which is consistent with APB observed for STO grown by MBE on Si(001).[36]

Since the misalignments can result in increased Ge–Sr bond length, dangling Ge bonds may also be formed. Both of the column misalignments and the possible Ge dangling bonds at the interface may contribute to the electrical trap states observed for SHO.[17] Surface steps without the formation of an APB are also indicated in Figure 3.9.(b) and (e).

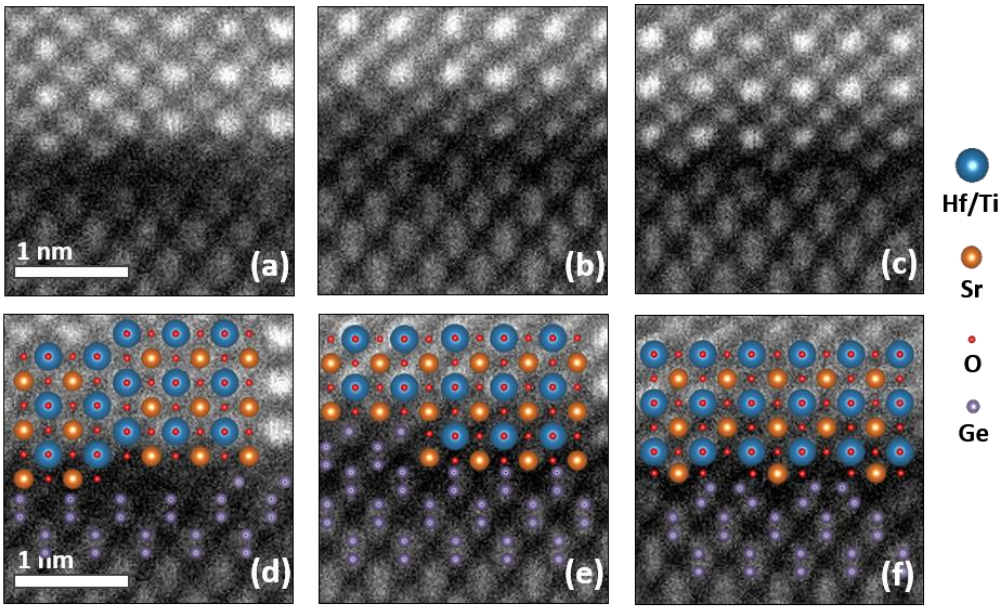

Figure 3.9. HAADF STEM images (a), (b) and (c) showing enlarged portions of regions ①, ② and ③ in Figure 3.8 (c), respectively. (d), (e) and and (f) HAADF STEM images with atomic structure overlaid for (a), (b) and (c), respectively.

The enlarged images in Figures 3.9.(c) and (f) indicate that some Ge retains the 2×1 reconstruction present in the starting surface (Figure 3.1) during ALD and annealing. The local interface structure in Figures 3.9.(b)/(e) and 5(c)/(f) is similar to that found for $BaTiO_3$ deposited by molecular beam epitaxy on a Ge (001) surface that first had ½ monolayer of Sr deposited to form a Zintl layer.[37] This might indicate that Sr orders at the Ge (001) surface during the initial ALD cycles to form a Zintl layer with Ge.

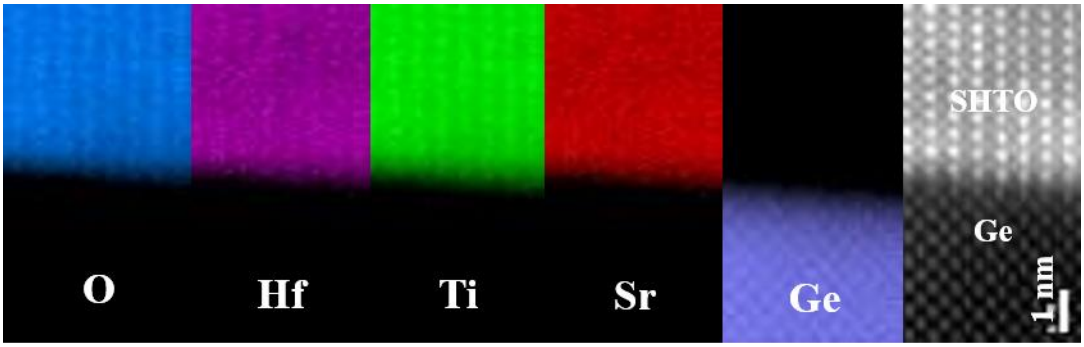

Figure 3.10. Electron-energy-loss spectroscopy (EELS) mapping to determine the elemental distribution in selected region for 14.0-nm $SrHf_xTi_{1-x}O_3$ with x = 0.55, post-deposition annealed at 645℃ for 5 min.

3.3.4. ELECTRICAL PROPERTIES

The crystallization temperatures for 4-nm thick STO and SHO were around 510 and 640 °C, respectively.[17,18] At 700 °C, an interfacial layer forms at the Ge-SHO interface that is <0.5 nm thick. This interfacial layer may contribute to the D_{it} values that were as low as 2×10^{12} $cm^{-2}eV^{-1}$ for crystalline SHO and increased with higher annealing temperatures.[17] To test the dielectric performance, the $SrHf_xTi_{1-x}O_3$ film with x = 0.55 was used to fabricate a MOS capacitor. The microstructure for this film revealed the presence of an APB in the near surface region and partial 2×1 reconstruction at the Ge-SHTO interface and these could be sources of interface trap states. The *C-V* and *I-V* curves are shown in Figures 3.11.(a) and (b), respectively. From Figure 3.11.(a), the capacitance achieves saturation at around 1.93 μF/cm^2, corresponding to a relative dielectric constant of k ~30. The *I-V* measurement shows leakage current of 0.1 A/cm^2 at 1 MV/cm with an EOT＝1.8 nm. Previous work in our group showed that the dielectric constant for SHO (4.6 nm) and STO (15 nm) is around 17 and 90, respectively.[17,18] If k is linearly dependent

on Hf content, k for the 14.0 nm $SrHf_{0.55}Ti_{0.45}O_3$ film is expected to appear at x=0.82, which indicates that the dielectric constant is more heavily weighted by Hf. The leakage current for SHO is 6.3×10^{-6} A/cm^2 at 1 MV/cm with an EOT＝1.0 nm and for STO is 10 A/cm^2 at 1 MV/cm with an EOT＝0.7 nm. Ignoring the EOT difference, which will cause even higher leakage current for this $SrHf_{0.55}Ti_{0.45}O_3$ sample if it was considered, the leakage current of SHTO shows two orders of magnitude improvement over STO. However, the leakage current was too high to allow reliable D_{it} to be measured and understand any relation to the microstructure.

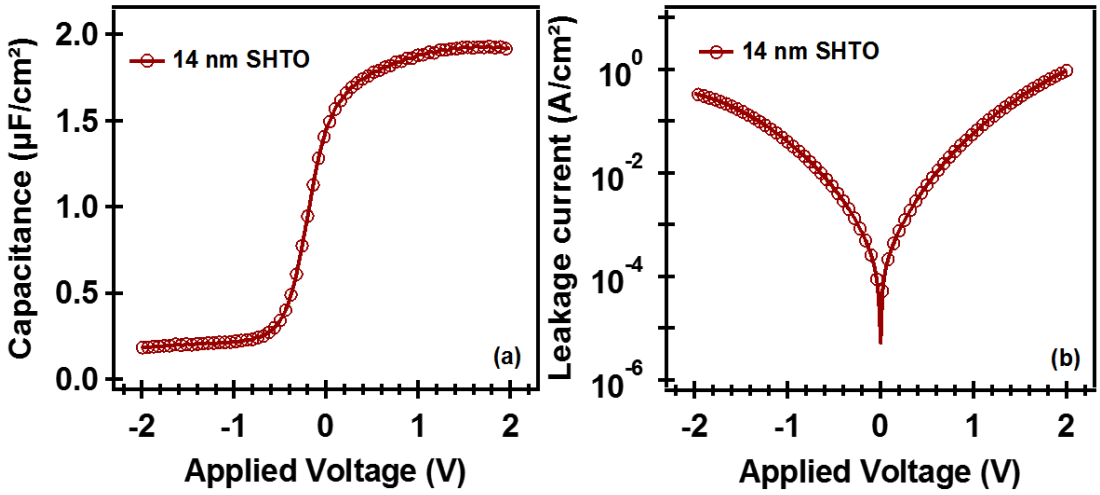

Figure 3.11. Capacitance-voltage (C-V) measurement (a) and current-voltage (I-V) measurement (b) for 14.0-nm $SrHf_xTi_{1-x}O_3$ (x = 0.55) film on Ge. The dielectric constant k=30 and leakage current is 0.1 A/cm^2 at 1 MV/cm with EOT＝1.8 nm.

3.4. SUMMARY

In this study, amorphous $SrHf_xTi_{1-x}O_3$ films have been grown on Ge (001) by ALD and annealed between 530°C to 660 °C to crystallize the film into a heteroexpitaxial layer.

Matching the lattice constant for the SHTO alloy with the substrate by adjusting *x* did not lowers the SHTO crystallization temperature rather the crystallization temperature increased monotonically with increasing Hf content. *In situ* XPS and AR-XPS analysis verified the stoichiometry and uniformity of the grown films. The *ex situ* XRR, XRD and rocking curve measurements were used to determine the thickness, lattice constant and crystallinity, respectively. The interface of a selected sample was explored by STEM and EELS mapping. The interface was abrupt with no apparent interdiffusion between the substrate and the SHTO layer. Regions of the Ge surface retained the 2×1 reconstruction. Film defects included grain tilting and APBs that are attributed to steps at the Ge (001) surface. Capacitance-voltage (*C-V*) and current-voltage (*I-V*) measurements show the dielectric constant k=30 and a leakage current I = 0.1 A/cm^2 (at 1 MV/cm with EOT＝1.8 nm) after the standard MOS capacitor was fabricated from a 14.0-nm SHTO film with Hf content x=0.55.

These results for SHTO films illustrate that ALD growth of quaternary perovskites directly on Ge (001) is feasible and that the properties can be adjusted with B-site substitution. Understanding the influence of strain and film microstructure on the D_{it} for crystalline ABO_3 layers on Ge necessarily requires systems that do not feature Ti on the B-site since Ti 3*d* states yield negligible conduction band offset with Ge, and require systems that crystallize at or below 650 °C to maintain an abrupt interface.

3.5. REFERENCES

1 P. S. Goley and M. K. Hudait, Materials **7**, 2301 (2014).

2 E, Simoen, J. Mitard, G. Hellings, G. Eneman, B. De Jaeger, L. Witters, B. Vincent, R. Loo, A. Delabie, S. Sioncke, M. Caymax, and C. Claeys, Mater. Sci. Semicond. Process. **15**, 588 (2012).

3 Y. Kamata, Mater. Today **11**, 30 (2008).

4 G. D. Wilk, R. M. Wallace, and J. M. Anthony, J. Appl. Phys. **89**, 5243 (2001).

5 S. Swaminathan, M. Shandalov, Y. Oshima, and P. C. McIntyre, Appl. Phys. Lett. **96**, 082904 (2010).

6 C. O. Chui, S. Ramanathan, B. B. Triplett, P. C. McIntyre, and K. C. Saraswat, IEEE Electron Device Lett. **23**, 473 (2002).

7 Y. Kamata, K. Ikeda, Y. Kamimuta, and T. Tezuka, 2010 Symposium on VLSI Technology. IEEE. 211–212 (2010).

8 C. H. Lee, C. Lu, T. Tabata, W. F. Zhang, T. Nishimura, K. Nagashio, and A. Toriumi, Electron Devices Meeting. IEEE. 2.5.1-2.5.4 (2013).

9 C. H. Lee, C. Lu, T. Tabata, T. Nishimura, K. Nagashio, and A. Toriumi, 2013 Symposium on VLSI Technology. IEEE. T28–T29 (2013).

10 R. Zhang, P.C. Huang, N. Taoka, M. Takenaka, and S. Takagi, 2012 Symposium on VLSI Technology. IEEE.161–162 (2012).

11 A. Rollett, F. J. Humphreys, G. S. Rohrer, and M. Hatherly, *Recrystallization and Related Annealing Phenomena* (Elsevier, 2004).

12 J. W. Reiner, A. M. Kolpak, Y. Segal, K. F. Garrity, S. Ismail-Beigi, C. H. Ahn, and F. J. Walker, Adv. Mater. **22**, 2919 (2010).

13 R. A. McKee, F. J. Walker, and M. F. Chisholm, Science **293**, 468 (2001).

14 R. A. McKee, F. J. Walker, and M. F. Chisholm, Phys. Rev. Lett. **81**, 3014 (1998).

15 M. Jahangir-Moghadam, K. Ahmadi-Majlan, X. Shen, T. Droubay, M. Bowden, M. Chrysler, D. Su, S.A. Chambers, and J.H. Ngai, Adv. Mater. Interfaces **2**, 1400497 (2015).

16 A. A. Demkov, A. B. Posadas, H. Seo, M. Choi, K. J. Kormondy, P. Ponath, R. C. Hatch, M. D. McDaniel, T. Q. Ngo, and J. G. Ekerdt, ECS Trans. **54**, 255 (2013).

17 M. D. McDaniel, C. Hu, S. Lu, T. Q. Ngo, A. Posadas, A. Jiang, D. J. Smith, E. T. Yu, A. A. Demkov, and J. G. Ekerdt, J. Appl. Phys. **117**, 054101 (2015).

18 M. D. McDaniel, T. Q. Ngo, A. Posadas, C. Hu, S. Lu, D. J. Smith, E. T. Yu, A. A. Demkov, and J. G. Ekerdt, Adv. Mater. Interfaces **1**, 1400081 (2014).

19 I. Oh, M.-K. Kim, J. Lee, C.-W. Lee, C. Lansalot-Matras, W. Noh, J. Park, A. Noori, D. Thompson, S. Chu, W. J. Maeng, and H. Kim, Appl. Surf. Sci. **287**, 349 (2013).

20 L. Bjaalie, B. Himmetoglu, L. Weston, A. Janotti, and C. G. V. de Walle, New J. Phys. **16**, 025005 (2014).

21 S. A. Chambers, Y. Liang, Z. Yu, R. Droopad, and J. Ramdani, J. Vac. Sci. Technol. Vac. Surf. Films **19**, 934 (2001).

22 F. Amy, A. S. Wan, A. Kahn, F. J. Walker, and R. A. McKee, J. Appl. Phys. **96**, 1635 (2004).

23 X. Zhang, A. A. Demkov, H. Li, X. Hu, Y. Wei, and J. Kulik, Phys. Rev. B **68**, 125323 (2003).

24 M. D. McDaniel, A. Posadas, T. Wang, A. A. Demkov, and J. G. Ekerdt, Thin Solid Films **520**, 6525 (2012).

25 C. D. Wagner, W. M. Riggs, L. E. Davis, and J. F. Moulder, Perkin-Elmer Phys. Electron. Div. (1979).

26 D. de Ligny and P. Richet, Phys. Rev. B **53**, 3013 (1996).

27 H. P. Singh, Acta Crystallogr. Sect. A **24**, 469 (1968).

28 S. Yamanaka, T. Maekawa, H. Muta, T. Matsuda, S. Kobayashi, and K. Kurosaki, J. Solid State Chem. **177**, 3484 (2004).

29 A. Meldrum, L. A. Boatner, W. J. Weber, and R. C. Ewing, J. Nucl. Mater. **300**, 242 (2002).

30 C. M. Brooks, L. F. Kourkoutis, T. Heeg, J. Schubert, D. A. Muller, and D. G. Schlom, Appl. Phys. Lett. **94**, 162905 (2009).

31 H. Ledbetter, M. Lei, and S. Kim, Phase Transit. **23**, 61 (1990).

32 J. F. Moulder, W. F. Stickle, P. E. Sobol, and K. D. Bomben, Perkin-Elmer Phys. Electron. Div. (1993).

33 M. P. Seah and W. A. Dench, Surf. Interface Anal. **1**, 2–11 (1979).

34 X. Jiang, R. Q. Zhang, G. Yu, and S. T. Lee, Phys. Rev. B **58**, 15351 (1998).

35 C. M. Foster, Z. Li, M. Buckett, D. Miller, P. M. Baldo, L. E. Rehn, G. R. Bai, D. Guo, H. You, and K. L. Merkle, J. Appl. Phys. **78**, 2607 (1995).

36 H. Wu, T. Aoki, A. B. Posadas, A. A. Demkov, and D. J. Smith, Appl. Phys. Lett. **108**, 091605 (2016).

37 K. D. Fredrickson, P. Ponath, A. B. Posadas, M. R. McCartney, T. Aoki, D. J. Smith, and A. A. Demkov, Appl. Phys. Lett. **104**, 242908 (2014).

Chapter 4: Zintl layer formation during perovskite atomic layer deposition on Ge (001)

4.1. INTRODUCTION

In 1998, McKee et al. reported that by using a submonolayer of alkaline earth metal (AEM), specifically strontium, one could enable the epitaxial growth of the perovskite $SrTiO_3$ on Si.[1] Since then, many groups have carried out studies of the growth of crystalline perovskite materials on various semiconductors, such as Si, Ge, and GaAs, for use as a gate oxide for field effect transistor applications.[2–13] At the same time, several groups also studied the details of the seemingly crucial sub-monolayer AEM template layer on Si (001),[14–21] which has been identified as being of Zintl character.[14,15,17,18] This Zintl template layer on Si strongly suppresses SiO_2 formation during the initial perovskite oxide nucleation process,[9,17,22–24] while simultaneously lowering the interface energy.[14–17] The presence of this Zintl template formed by half monolayer (ML) AEM coverage is necessary for direct epitaxy of a perovskite on Si.

After removing the native oxide in ultrahigh vacuum, the Si (001) and Ge (001) surfaces reconstruct via dimerization to form a 2×1 structure. When AEM atoms adsorb on the 2×1-reconstructed Si (001) surface, the most favorable bonding location for the AEM atoms is the four-fold site in the trough between two dimer rows, which has been confirmed both experimentally and theoretically.[14,16,19,22,25] Once the AEM atoms fill all the available four-fold sites on Si (001), the surface acquires the character of a Zintl phase.[14]

The Allen electronegativities of Sr, Ba, Si and Ge are 0.963, 0.881, 1.916 and 1.994, respectively.[26] Because the electronegativity for an AEM atom is much less than that of Si,

S. Hu, E. L. Lin, A. K. Hamze, A. Posadas, H-W. Wu, D. J. Smith, A. A. Demkov, and J. G. Ekerdt, J. Chem. Phys. 146, 052817 (2016).
Comments: I designed and conducted the experiment.

the AEM atoms will donate electrons to Si and form the AEM–Si Zintl bond.[14–17,21,27] In the case of Sr on Si, one Sr atom will donate its two valence electrons to the neighboring Si dimer atoms such that each Si dimer atom will receive one electron. This extra electron fills the dangling bond at the down atom of the dimer, removing the dimer tilt (which is a Peierls distortion).[15] The 2×1-reconstructed Ge surface exhibits the same dimer tilting phenomenon as in Si.[15,28] The Ge atoms in a given dimer can become more stable if one of them transfers charge to the other so that the unbounded orbital of the receiving atom becomes filled and that of the donating atom becomes empty. Because of the nature of the empty and filled orbitals, this transfer results in the dimer tilting on a clean surface.[29]

Due to similar electronegativity for Si and Ge, the AEM atoms are expected to have similar charge transfer behavior on Ge as that on Si, and it would be reasonable to expect the template model developed for Si applies to Ge. While there is less work reported either theoretically or experimentally for AEM atoms on Ge (001) compared to Si (001) there are noticeable differences between the systems.[30–32] Higher-order surface reconstructions are found with 0.5-ML Sr on Ge (100) compared to Si (100), with a 9×1 reconstruction found on Ge.[14,15,21,31] However, a 2×1 reconstruction has been reported for 0.45-ML Ba on Ge (001).[30] Finally, the surface restructuring found with Ge (001) has been associated formation of a Sr-Ge surface alloy and lower Ge–Ge binding energy as compared with a surface ad-layer on Si (001).[31,32]

The epitaxial integration of crystalline perovskites on semiconductors by atomic layer deposition presents an ideal platform to explore numerous technological applications since perovskites can be ferromagnetic,[33,34] ferroelectric,[35,36] multiferroic,[37,38] or superconducting.[39] Previously, we reported the successful growth of $SrBO_3$ perovskite materials, where B = Ti or Hf, on Ge by ALD.[40–42] However, the mechanism for the initial growth of perovskites on Ge by ALD is not yet understood. One key commonality in the

ALD process is that the Sr cyclopentadienyl precursor is dosed first on the clean Ge surface. High–resolution cross-section scanning transmission electron microscopy imaging of molecular beam epitaxy-grown $BaTiO_3$ and atomic layer deposition-grown $SrHf_{0.55}Ti_{0.45}O_3$ reveal a 2×1 periodicity at the interface with the AEM atom between dimer rows.[42,43] Based on this observation, we believe that the initial atomic layer deposition (ALD) growth for $SrHf_{0.55}Ti_{0.45}O_3$ on Ge forms out of the same Zintl template as found in molecular beam epitaxy (MBE) growth. To understand the initial interface reactions during perovskite ALD on Ge, we studied the deposition of Sr and Ba molecular precursors on Ge using *in situ* X-ray photoelectron spectroscopy (XPS) and reflection high energy electron diffraction (RHEED) and compare the results with Sr and Ba deposition using Knudsen cells in an MBE system and with density functional theory calculations.

4.2. EXPERIMENT

The Ge (001) substrate is prepared from a 4-inch Ge wafer (Sb-doped, ρ~0.04 Ω-cm) from MTI Corp. as described previously.[40–42] The as-received Ge wafer is diced into approximately 18×20 mm^2 pieces, degreased with acetone, isopropyl alcohol and water, dried and then exposed to ultraviolet light/ozone to remove residual carbon, and transferred into the growth and characterization system. The surface GeO_2 is removed by annealing at 700 °C in vacuum (< 2×10^{-9} Torr) for 1 hr. The resulting 2×1-reconstructed Ge (001) surface is verified by *in situ* RHEED (Staib Instruments operating at 21 keV). The clean Ge (001) sample is transferred *in vacuo* to an XPS chamber to verify the Ge surface composition. Following this characterization, the sample is then transferred *in situ* and exposed to varying doses of elemental Sr and Ba in the MBE chamber, or exposed to the

metal-organic barium bis(triisopropylcyclopentadienyl) [Ba(^{i}Pr$_3$Cp)$_2$] or strontium bis(triisopropylcyclopentadienyl) [Sr(^{i}Pr$_3$Cp)$_2$] precursors in the ALD chamber.[44]

For elemental deposition in the MBE chamber the substrate was maintained at 600 °C following protocols in previous reports.[44,45] The Ba and Sr fluxes were calibrated with a quartz crystal monitor to a rate of approximately 1 ML/min, allowing for controlled submonolayer dosing. Coverages of Ba or Sr are reported in ML equivalents for MBE-dosed samples, where a ML is defined to be the atomic density of the Ge (001) unreconstructed surface (6.26×10^{14} atoms/cm^2). RHEED was used to monitor surface structure *in situ* and in real time. The MBE-dosed samples were cooled to 200 °C before transferring the sample into the XPS analysis chamber. For deposition in the ALD chamber the sample was maintained at 225 °C, the typical temperature used for $BaTiO_3$ or $SrTiO_3$ growth.[40,46] The Ba and Sr precursors, barium bis(triisopropylcyclopentadienyl) [Ba(^{i}Pr$_3$Cp)$_2$] and strontium bis(triisopropylcyclopentadienyl) [Sr(^{i}Pr$_3$Cp)$_2$], were supplied by Air Liquide.[47] The Ba precursor was heated to 150 °C and the Sr precursor was heated to 130 °C to produce sufficient vapor pressure for dosing in ALD.[46,48] The ALD chamber was maintained at a total pressure of 1 Torr using Ar carrier gas during dosing and less than 1×10^{-6} Torr when in standby mode. An ALD half-cycle refers to a 2-s exposure to the precursor stream followed by a 20-s Ar purge (referred to as 1 half-cycle herein). A complete cycle refers to a 2-s precursor exposure, 20-s argon purge, 2-s deionized water exposure, and another 20-s argon purge (referred to as 1 cycle herein). The ALD-dosed samples were transferred out of the ALD chamber without cooling the sample and subsequently cooled to room temperature in the transfer line.

In situ XPS was performed with a monochromatic Al Kα source at 1486.6 eV using a VG Scienta R3000 electron energy analyzer. The analyzer was calibrated with a clean Ag foil such that the Ag 3$d_{5/2}$ core level is at a binding energy of 368.28 eV. For high

resolution scans of the Sr 3*d*, Ba 3*d*, Ge 3*d* and C 1*s* core levels, we use a pass energy of 100 eV in combination with a 0.8 mm entrance slit to yield a minimum linewidth of 300 meV. An incident angle of 0° was used for Sr 3*d*, Ba 3*d*, Ge 3*d* features while an incident angle of 60°, which limits the sampling depth to about 5.0 nm,[49] was used for the C 1*s* feature. The XPS results were analyzed with CasaXPS (Version 2.3.16 PR 1.6).

The interface structures of samples with a crystalline perovskite oxide grown on top were examined by high-angle annular-dark-field scanning transmission electron microscopy (HAADF STEM). The samples were prepared via standard cross-section method with Ar ion milling. The aberration-corrected STEM images were taken with a JEOL ARM 200F operated at 200 kV. The beam convergence angle was set to 20 mrad and the HAADF images were recorded with collection angle of 90-150 mrad.

4.3. THEORY

To clarify experimental results, in particular photoemission, density functional theory (DFT) calculations were performed using the Vienna *ab initio* Simulation Package (VASP) with projector augmented-wave (PAW) pseudopotentials.[50–55] The exchange-correlation energy was calculated in the local density approximation (LDA)[56] and in the generalized gradient approximation (GGA).[57,58] Two germanium pseudopotentials[54,55] were used for both the LDA and GGA calculations: one included only the valence $4s^2 4p^2$ electrons, and the other treated the semi-core 3*d* electrons as valence electrons as well, for a configuration of $3d^{10} 4s^2 4p^2$. For strontium and barium, the semi-core *s* and *p* states are treated as valence states, so the electron configurations are $4s^2 4p^6 5s^2$ and $5s^2 5p^6 6s^2$, respectively. A plane wave cutoff of 650 eV was utilized for all calculations performed, and a 6×12×2 Monkhorst-Pack *k*-point grid[59] was used for the 2×1 structures. The *k*-point

sampling was modified accordingly for the 2×2 and 4×4 structures to maintain the same *k*-point density in the irreducible wedge of the Brillouin zone. The electronic energy was converged to 10^{-6} eV and the cells were relaxed until the interatomic forces were smaller than 10^{-2} eV/angstrom. For the LDA calculations, the theoretical lattice constants were $a_{Ge} = 5.625$ Å and $a_{Ge} = 5.646$ Å with and without the $3d$ semi-core electrons, respectively. For the GGA calculations, the theoretical lattice constants were $a_{Ge} = 5.758$ Å and $a_{Ge} = 5.783$ Å with and without the $3d$ semi-core electrons, respectively. The slabs used were 14 layers thick (three and a quarter unit cells), and the thicker slabs (used only in some LDA calculations) were 22 layers thick (five and a quarter unit cells). All slabs had 15 Å of vacuum to prevent spurious interactions with their periodic images. All clean germanium slabs were relaxed until the known surface reconstruction was achieved.[60,61] The 2×1 slabs had only one tilted dimer on the surface, and the 2×2 and 4×4 had multiple dimers tilted in alternating directions. One-half of a monolayer (ML) of barium and strontium atoms were placed in the troughs between the surface dimers,[14,17] and then all the atoms were allowed to relax. After relaxation, the surface dimers in the presence of alkaline-earth atoms are no longer tilted. That is to say, there is no difference between the up and down germanium atoms of a dimer after relaxation. This is illustrated for the fully relaxed 4×4 slab surface with and without barium in Figure 4.1. The surface dimers are 4.6% shorter with the barium adatoms than they are on the clean germanium surface, and are 0.8% shorter with the strontium adatoms.

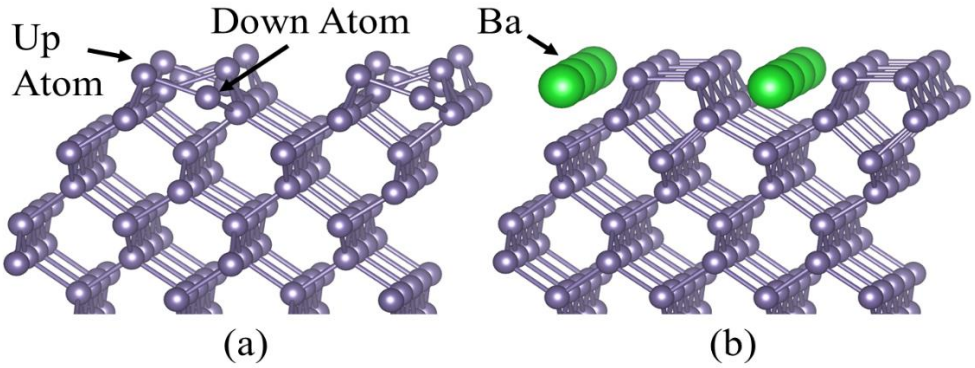

Figure 4.1. (a) Relaxed, clean 4×4 germanium slab surface, exhibiting trough and dimer rows, and alternating tilt angles in the dimers. (b) Relaxed 4×4 germanium slab surface after adding 0.5 ML of barium atoms to the surface. The surface dimers flatten in the presence of alkaline-earth ions.

4.4. RESULTS

Figure 4.2.(a) shows the x-ray photoelectron spectra for the Ba $3d_{5/2}$ feature for increasing Ba coverage on Ge (001) as deposited by MBE. As the Ba coverage increases, the Ba $3d_{5/2}$ main peak is found at a binding energy of 781.03 eV, 780.81 eV and 780.63 eV for 0.3 ML, 0.5 ML and 1 ML, respectively. Figure 4.2.(b) shows RHEED patterns corresponding to 0, 0.3 and 0.5 ML of Ba on Ge (001). The clean surface (0-ML Ba) displays the 2×1 reconstruction expected for a bare surface after removal of the oxide layer.[40] RHEED images (not shown) reveal the intensity of the 2×1 spot changes with low coverage but does not fully disappear; it initially weakens at 0.17 ML and then slowly recovers its full intensity after about 0.3 ML and does not significantly change between 0.3 and 0.5 ML. The RHEED images for 0.3- and 0.5-ML Ba are of a 2×1-reconstructed surface. The 2×1-reconstructed surface following 0.5-ML Ba is consistent with results reported by Cattoni et al., for 0.45-ML Ba.[30] Higher-order reconstructions have been

reported for 0.5-ML Ba and Sr on Ge (001).[31] We also observe higher-order reconstructions of Ge (001) for 0.5-ML-MBE Sr on Ge (001) (Figure 4.3), whereas one ALD Ba half-cycle leads to a 2×1-reconstructed Ge (001) surface (not shown). More study is required to reconcile the different reconstructions for MBE-based 0.5-ML AEM on Ge (001), but this is beyond the scope of this study.

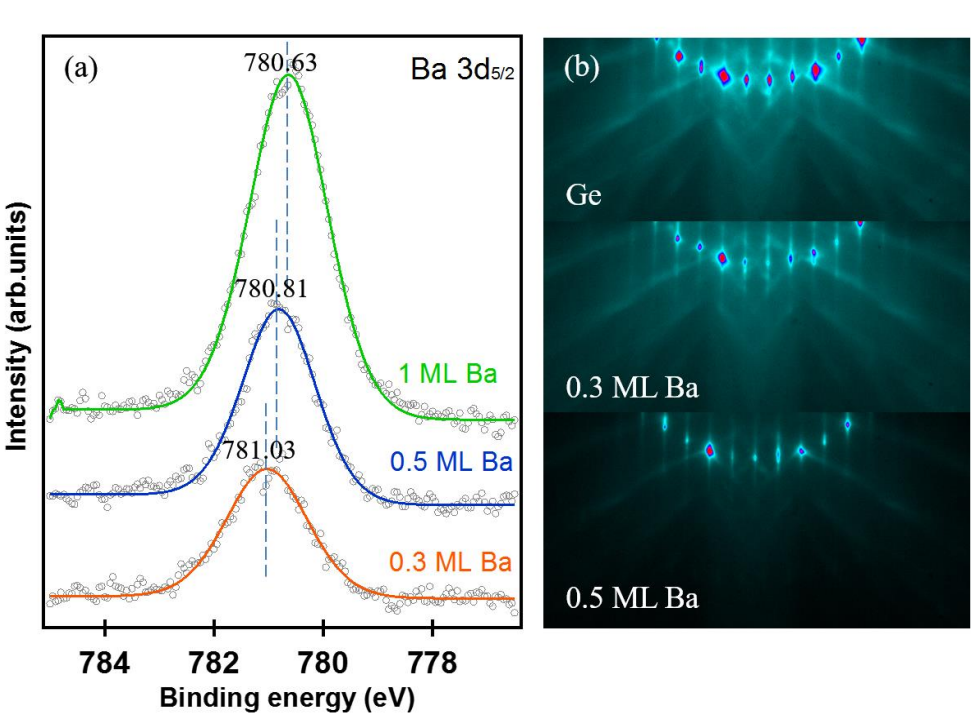

Figure 4.2. (a) X-ray photoelectron spectra of Ba $3d_{5/2}$ for different Ba coverage on Ge (001). Grey circles indicate the experiment data and the spectral fitting results are shown by solid colored lines. The peak position for each coverage is marked by a dashed line. (b) RHEED images of clean Ge surface before deposition and after deposition of 0.3-ML and 0.5-ML Ba, all images are taken at 200 °C substrate temperature and the beam is aligned along the [110] azimuth.

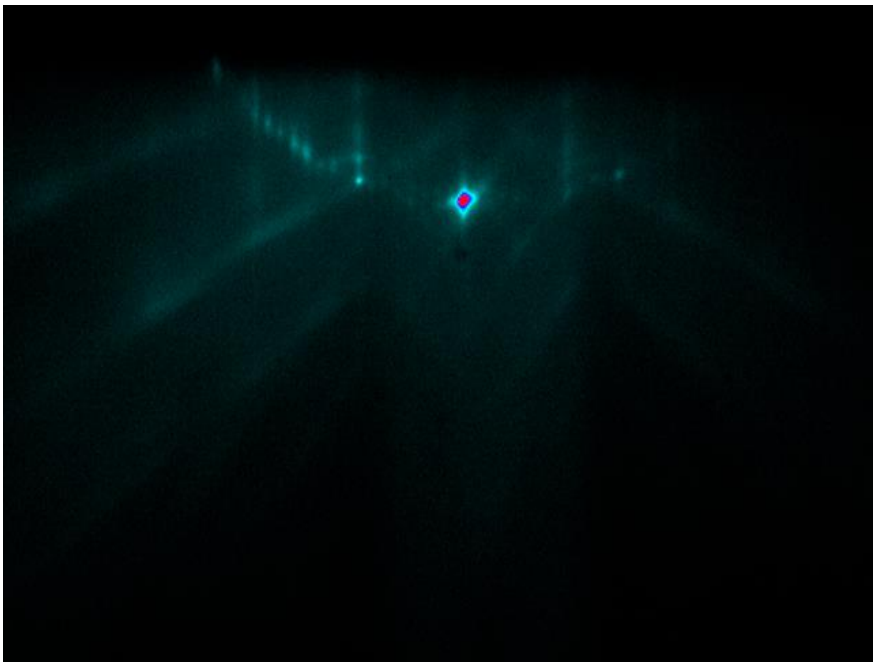

Figure 4.3. RHEED patterns of the Ge (001) surface after depositing of 0.5 ML of Sr. The image is taken at 200 °C and the beam is aligned along the [110] azimuth.

Figure 4.4 is a comparison of the Sr 3*d* and Ba 3$d_{5/2}$ spectra for MBE dosing and for ALD precursor dosing using a half cycle. Figure 4.5 shows the corresponding changes in the Ge 3*d* spectra for MBE and ALD dosing with Sr and Ba. We look at the 0.5-ML coverage in more detail since this coverage leads to the 2×1 Zintl layer that is critical for enabling epitaxial growth of $SrTiO_3$ or $BaTiO_3$ on Si and Ge by MBE.[1,2,43,45,62–64] Since the background region for Ge is not flat in the 140 to 130-eV range, the spectral data for Sr were smoothed with the Savitzky Golay function using Igor Pro 6.10. For Sr deposition, the Sr 3$d_{5/2}$ peak position shifted from 134.30 eV for 0.5-ML exposure to 133.96 eV for 1.0-ML exposure while the bulk Ge 3$d_{5/2}$ peak shifted from 29.28 eV for bare Ge (001) to 29.60 eV for 0.5-ML Sr exposure. The Sr 3$d_{5/2}$ peak for Ge exposed to one ALD half-cycle is at 134.30 eV with the bulk Ge 3$d_{5/2}$ peak shifted to a higher binding energy of 29.69 eV compared to the bare Ge (001) surface. The results for Ba exposure parallel those of Sr;

the bulk Ge $3d_{5/2}$ peak shifted to a higher binding energy for 0.5-ML Ba or one Ba ALD half-cycle compared to the bare surface binding energy (Figure 4.5.(b)) and the Ba $3d_{5/2}$ peak shifted to lower binding energy with increasing Ba coverage (Figure 4.2.(a)).

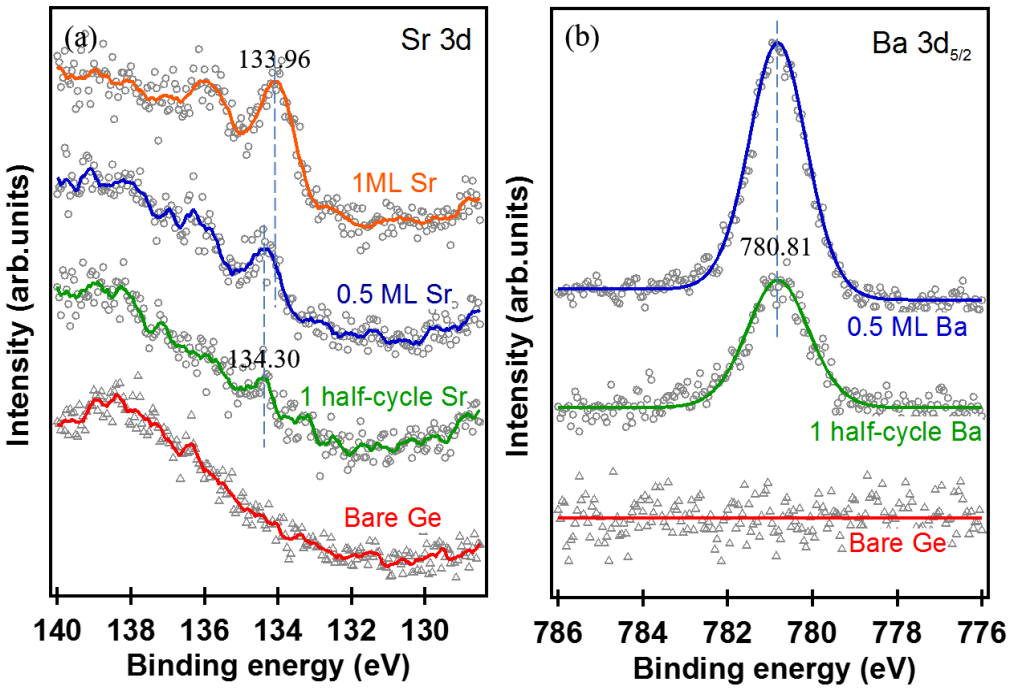

Figure 4.4. X-ray photoelectron spectra of (a) Sr 3*d* and (b) Ba $3d_{5/2}$ for Sr and Ba deposited on Ge (001) by ALD and MBE. The grey circles are the experimental data and the spectral fitting results are shown by the solid colored lines. The peak positions for Sr $3d_{5/2}$ and Ba $3d_{5/2}$ are marked by the dashed lines.

A 2-s exposure to the Sr or Ba precursor in the first half-cycle of ALD leads to Sr and Ba coverages of approximately 0.2 ML, based on a comparison of the XPS integrated areas for the respective ALD half-cycle exposures and the 0.5-ML exposures in Figure 4.4. Since the XPS signals for Ba were more intense than those of Sr and were not affected by the background feature from pure Ge, additional studies were conducted with Ba. Figure

4.6.(a) presents the Ba 3*d* spectra following a 2-s and a 4-s exposure to $Ba(^{i}Pr_3Cp)_2$. The Ba $3d_{5/2}$ peak area remained unchanged indicating the saturation coverage is already reached with the 2-s exposure.

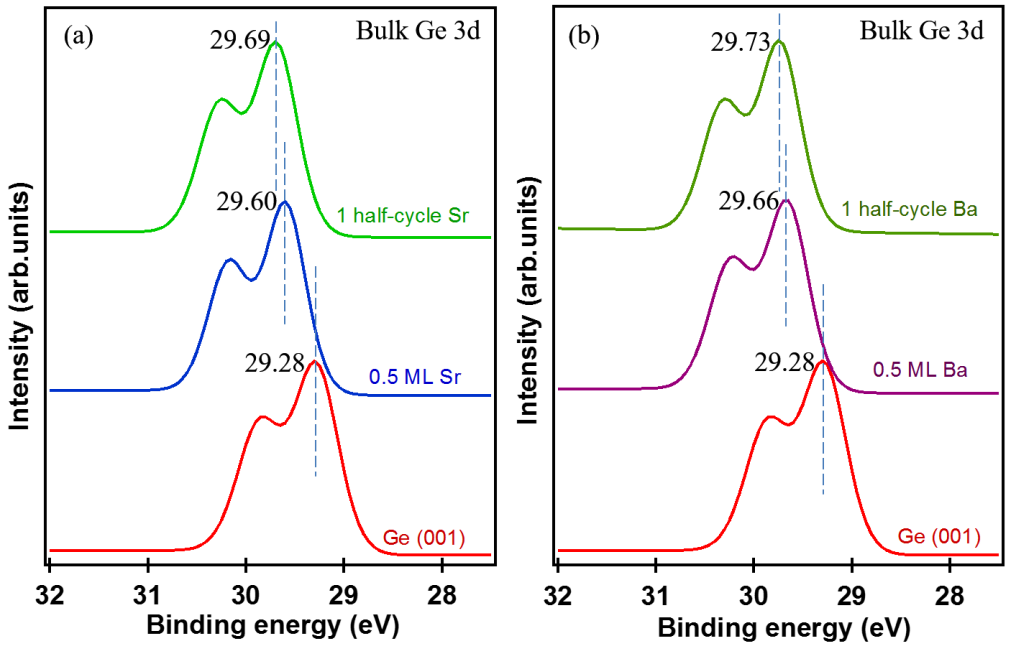

Figure 4.5. X-ray photoelectron spectra of Ge 3*d* for bare Ge, 0.5-ML coverage by MBE and one ALD half-cycle deposition for (a) Sr deposition and (b) Ba deposition. The Ge $3d_{5/2}$ peak position is marked by a dashed line.

The nature of the adsorbed Ba precursor could not be determined with certainty since the sample had to be transferred from the ALD chamber, through a transfer line at around 2×10^{-9} Torr into the analysis chamber. Below we present evidence that the surface contains completely and/or partially dissociated precursor, molecular precursor, and ligands following adsorption. During sample transfer, we suspect the residual water in the ALD chamber reacts with the sample surface and effectively completes the ALD cycle. Evidence for this includes the observation that after the sample is moved from the ALD

chamber to the analysis chamber and then back to the ALD chamber for another 2-s exposure to Ba(^{i}Pr$_3$Cp)$_2$, the Ba 3*d* signal intensity increases (Figure 4.6.(b)). Repeating this process leads to a further increase in the Ba 3*d* signal.

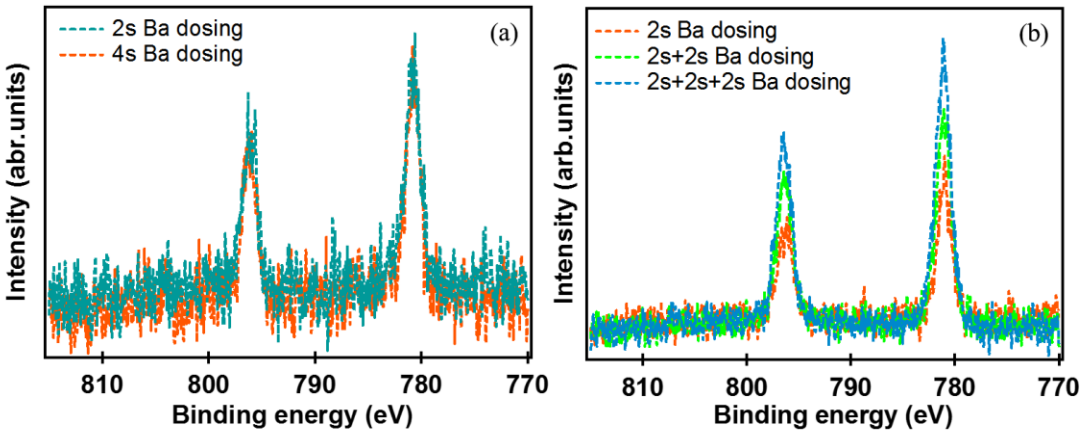

Figure 4.6. (a) Ba 3*d* X-ray photoelectron spectra after 2-s Ba exposure using the standard half-cycle and after 4-s of exposure followed by the 20-s Ar purge. (b) Ba 3*d* spectra following a 2-s exposure to the Ba precursor in the ALD chamber and transferring the sample into the analysis chamber, and then repeating this process on the same sample a second time (2s + 2s), and then a third time (2s + 2s + 2s).

Figure 4.7 presents the C 1*s* X-ray photoelectron spectrum following exposure of a clean Ge (001) surface to the ALD chamber for 1 min and the spectrum following the standard 2-s half-cycle ALD exposure to Ba(^{i}Pr$_3$Cp)$_2$. Carbon, likely in the form of precursor ^{i}Pr$_3$Cp ligands that persist in the ALD chamber background, adsorbed on the clean Ge (001) surface without exposing the surface to the Ba(^{i}Pr$_3$Cp)$_2$ precursor. Using the relative sensitivity factors for Ba and C and that a 0.2-ML coverage for Ba results from a half-cycle exposure, we estimate the C coverage to be 1.0 ML.[65] Putting this amount of carbon in perspective, each Ba(^{i}Pr$_3$Cp)$_2$ molecule contains 1 Ba and 28 C atoms so the surface could easily adsorb the 5×-equivalents of C:Ba from adsorbed ligands or ligand

fragments. This carbon level remains constant while Ba accumulates on the surface during the experiments presented in Figure 4.6.(b). Figure 4.8 presents the corresponding C 1*s* spectra to accompany Figure 4.6.(b) and shows that the C 1*s* signal remained constant. We note there is no carbon detected in $SrHfO_3$, $SrTiO_3$, $SrTi_xHf_{1-x}O_3$ films that have been grown by ALD on Ge (100) from these precursors so carbon reported herein is somehow associated with the Ge surface.[40–42]

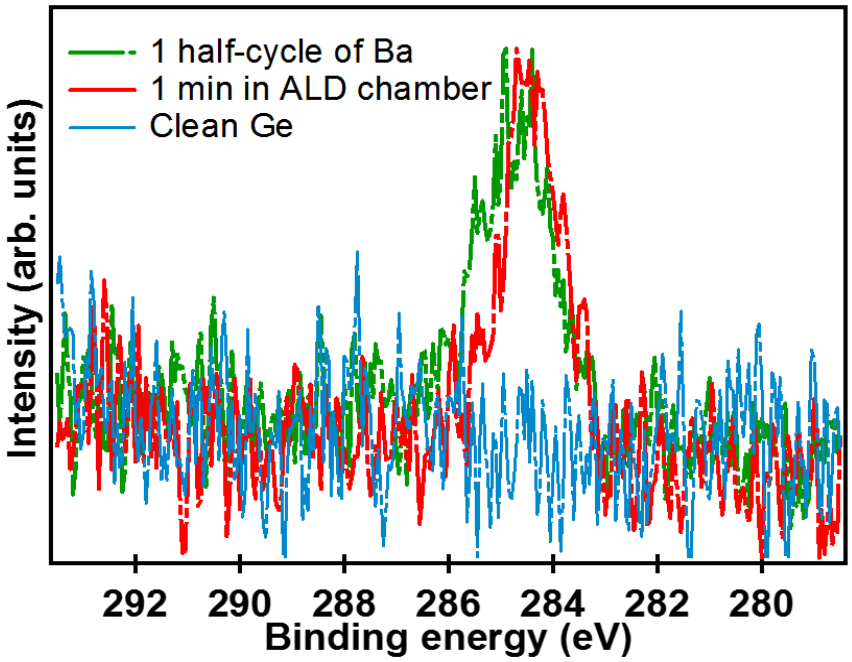

Figure 4.7. C 1*s* X-ray photoelectron spectra of a clean Ge surface after GeO_2 removal and thermal annealing, for a clean Ge surface that was moved into the ALD chamber for 1 min and then transferred to the analysis chamber, and a clean Ge surface after exposure to the Ba ALD half-cycle.

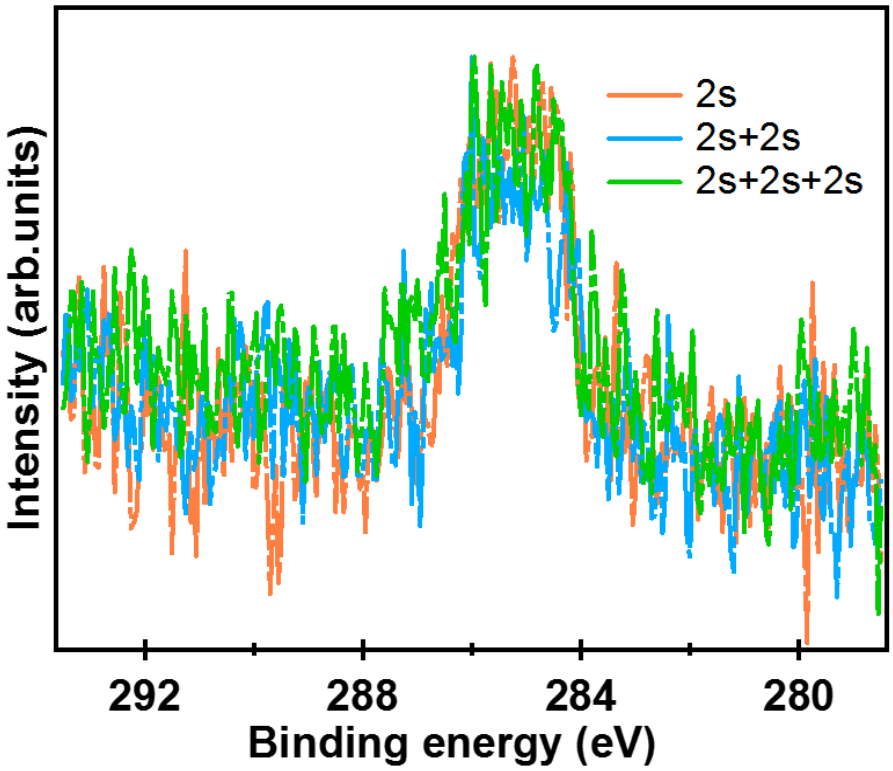

Figure 4.8. C 1*s* X-ray photoelectron spectra following a 2-s exposure to the Ba precursor in the ALD chamber and transferring the sample into the analysis chamber, and then repeating this process on the same sample a second time (2s + 2s), and then a third time (2s + 2s + 2s).

Evidence in support of some $Ba(^{i}Pr_3Cp)_2$ molecules adsorbing intact following the first half-cycle is provided in Figure 4.9. The Ba peak area is unchanged in Figure 4.9.(a) after one complete cycle when the sample is subjected to the vacuum of the transfer line ($\sim 2\times10^{-9}$ Torr) and the analysis chamber ($\sim 1\times10^{-9}$ Torr) in between the first half-cycle precursor dose and the second half-cycle water dose. When the Ge surface is exposed one complete ALD cycle continuously, *i.e.*, precursor dose, Ar purge, water dose, and Ar purge, the Ba peak area corresponds to 0.4 ML (Figure 4.9.(b)). If some, or all, molecularly-adsorbed $Ba(^{i}Pr_3Cp)_2$ desorbs during transfer to the analysis chamber (Figure 4.9.(a)) at the

lower background pressure, a lower Ba signal in Figure 4.9.(a) should be expected compared to Figure 4.9.(b) where the full 2-s exposure coverage was present to react with water in the second half-cycle.

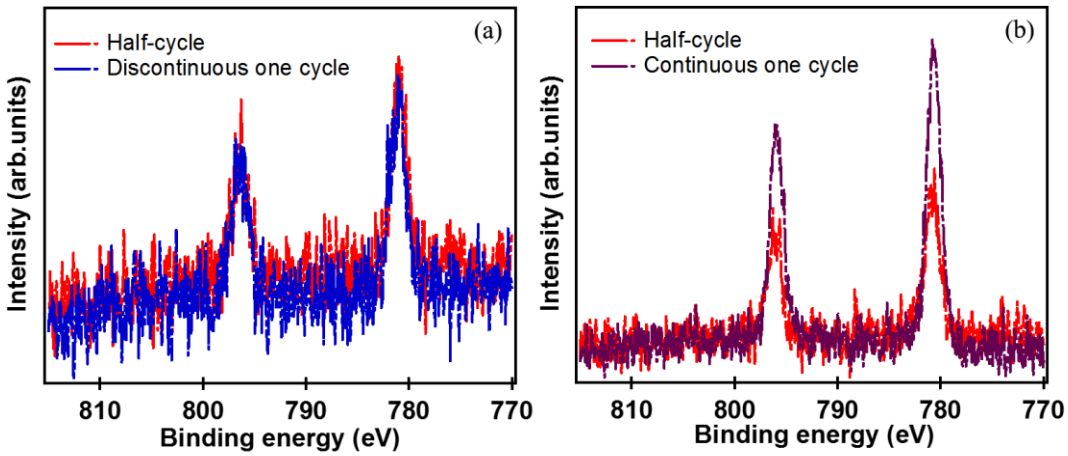

Figure 4.9. Ba 3*d* X-ray photoelectron spectra when (a) the water exposure in the second half-cycle is performed after transferring the sample into the analysis chamber and back into the ALD chamber, and (b) the water exposure of the second half-cycle is performed before transferring the sample into the analysis chamber.

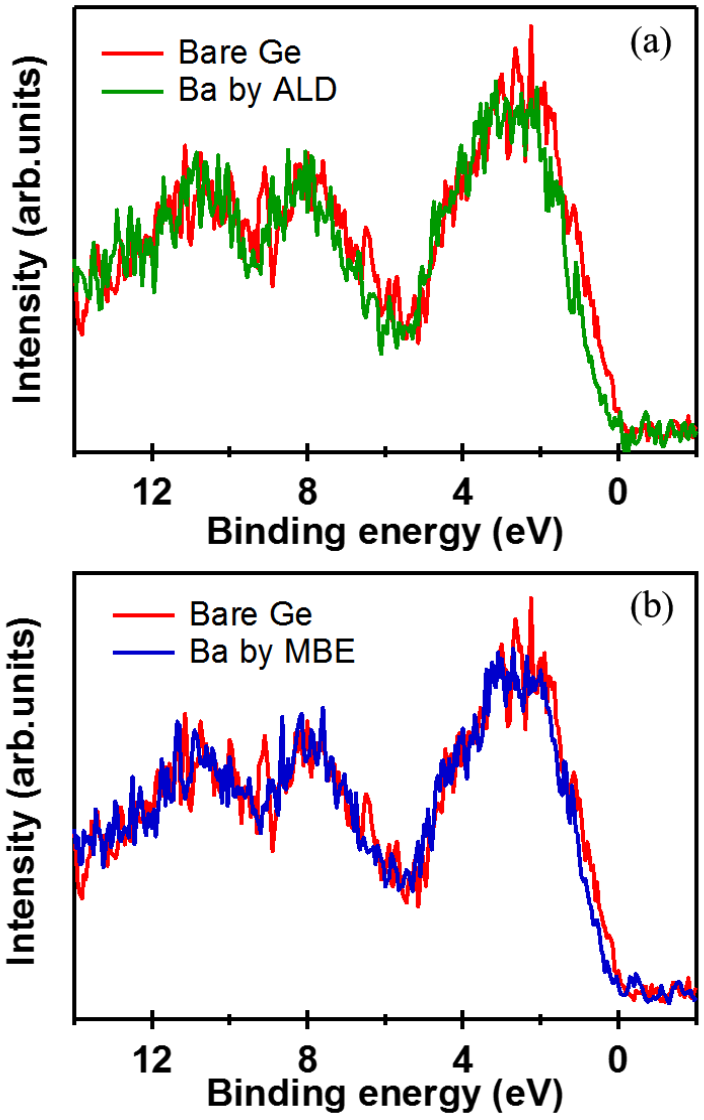

Figure 4.10. Valence band comparisons for bare Ge (001) with (a) one Ba ALD half-cycle and (b) 0.3-ML Ba by MBE.

As shown in Figure 4.5, both Sr and Ba deposition on Ge (001) by ALD and MBE shifted the bulk Ge 3*d* peak towards higher binding energy compared to bare Ge (001). This Ge binding energy shift is attributed to electron transfer from the AEM (Sr or Ba) to Ge. The charge transfer was verified by comparing the shift of the valence band edge,

which was determined by the linear extrapolation method[66] to the shift in the Ge core levels. Figure 4.10.(a) presents the valence band spectra for clean Ge (001) and after adsorption of one Ba ALD half-cycle, which produces 0.2 ML of Ba, on a different Ge (001) sample. Figure 4.10.(b) presents the valence band spectra for clean Ge (001) and after adsorption of 0.3 ML of Ba in the MBE chamber on a different Ge (001) sample. The Ge valence band edge shifted by 0.34 eV to higher binding energy after the Ba ALD half-cycle and by 0.22 eV to higher binding energy after 0.3-ML-MBE Ba deposition.

Surface core level shifts (SCLS) were explored to further understand the effect of the charge transfer from the alkaline earth metal to Ge, with the results presented in Figure 4.11 for Ba, Figure 4.12 for Sr and Figure 4.13 for bare Ge. Constraints used for deconvolution of the Ge 3*d* spectrum were obtained from the literature. Ge $3d_{3/2}$ and Ge $3d_{5/2}$ components have an intensity ratio of 0.67 and a separation of 0.585 eV.[67] The surface core level shifts for Ge were calculated based on full final-state theory and, relative to the bulk component, found to be -0.67 eV for the up atom, -0.39 eV for the down atom, and -0.16 eV for second layer atoms.[28] A Ge^{+1} component with a relative binding energy of +0.7 eV is also included in the fitting.[40] Using these parameters the Ge 3*d* peak for bare Ge (001) was fitted as shown in Figure 4.13. As illustrated in Figure 4.13 when -0.67 eV was used for the up atom of the tilted Ge dimer, the fit to the lower energy shoulder was poor. Figure 4.13 also presents the fit that results when a relative binding energy of -0.89 eV is used for the up atom instead but with all the other energies (*e.g.*, -0.39 eV for the down atom) kept the same as the values in the literature. This relative energy of -0.89 eV produced the lowest residual standard error when fitted in CasaXPS, and was used herein for the remainder of the study.

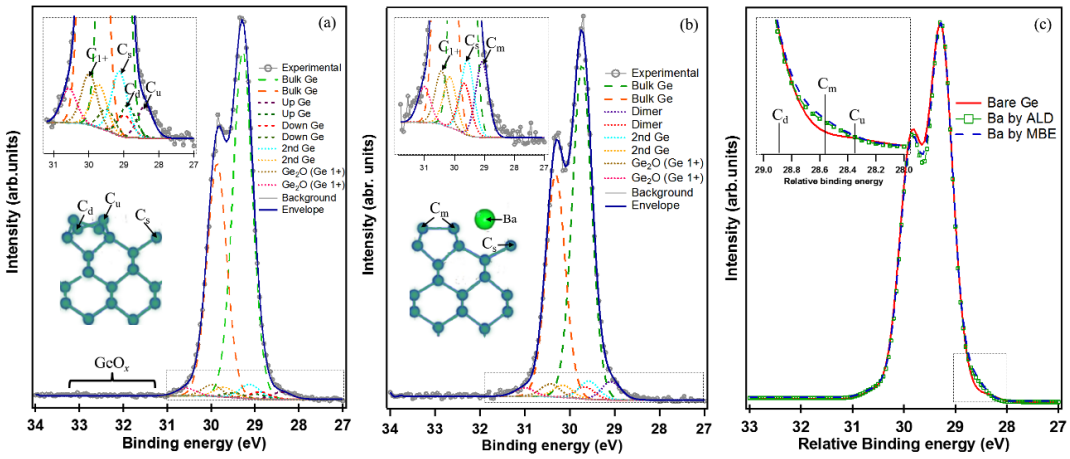

Figure 4.11. Spectral fitting of the high resolution Ge 3*d* spectrum for (a) bare Ge (001) and (b) after deposition of Ba by one half-cycle; the dashed frame is presented in a magnified view in the insets and the related structure models are inserted for (a) and (b). (c) Presents an overly of the fitted envelope curves for Ge 3*d* from (a) and (b) and 0.5-ML Ba by MBE; the dashed frame magnifies the lower binding energy shoulder and the solid black lines indicate the relative component positions.

Figure 4.11.(a) presents the fit for bare Ge (001); the spectrum was deconvoluted into five components (bulk Ge, C_{1+} for Ge^{1+}, C_s for second layer Ge, C_d for the down Ge of the Ge dimer, and C_u for the up Ge of the Ge dimer). The bulk Ge component was found to have a binding energy of 29.28 eV for Ge $3d_{5/2}$. After depositing Ba by ALD, based on studies on Si (100), the charge transfer from Ba to Ge is expected to symmetrize (flatten) the surface dimer so that the C_u and C_d components will merge into a single dimer component C_m.[17] The Ge 3*d* spectrum for one Ba ALD half-cycle on Ge (001) is shown Figure 4.11.(b), which was deconvoluted into four components; the bulk Ge component of Ge $3d_{5/2}$ is at 29.73 eV, the C_{1+} and C_s components retained their relative position to bulk Ge, and a dimer component C_m was fitted at -0.65 eV relative to bulk Ge. The dimer component C_m for 0.5-ML-Ba coverage (not shown) was found at -0.64 eV relative to bulk Ge. The fitted-Ge 3*d* curves are presented in Figure 4.11.(c) after artificially shifting the

peaks for one Ba ALD half-cycle and 0.5-ML-MBE Ba to have the same bulk energy as bare Ge (001), *i.e.*, 29.28 eV, in order to visually compare the lower binding energy shoulders. The inset to Figure 4.11.(c) shows the bare Ge sample has less signal intensity at the C_m position than the other two samples, consistent with a flattened dimer after adsorbing Ba.

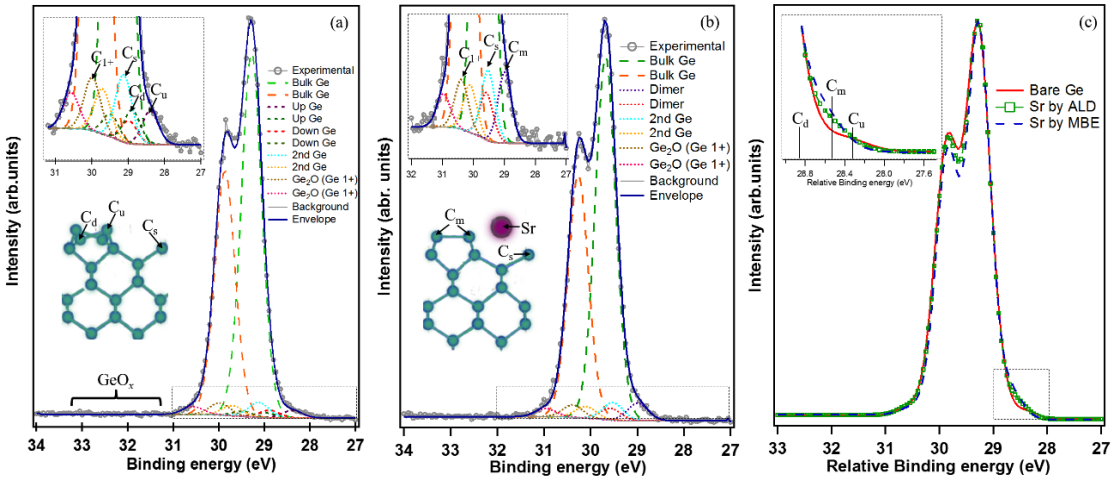

Figure 4.12. Spectral fitting of the high resolution Ge 3*d* spectrum for (a) bare Ge (001) and (b) after deposition of Sr by one half-cycle; the dashed frame is presented in a magnified view in the insets and the related structure models are inserted for (a) and (b). (c) Presents an overly of the fitted envelope curves for Ge 3*d* from (a) and (b) and 0.5-ML Sr by MBE; the dashed frame magnifies the lower binding energy shoulder and the solid black lines indicate the relative component positions.

The same analysis was applied to Ge 3*d* spectra after one Sr ALD half-cycle and 0.5-ML-MBE Sr adsorption with similar results as Ba (Figure 4.12). The C_m dimer component position for Sr by ALD was found at -0.69 eV and at -0.62 eV for 0.5-ML-MBE Sr.

In density functional theory, the approximate binding energy of a core electron can be calculated as the difference between the energies of the ground state system and the system with a core electron removed from the core:[68]

$$E_B = E(n_c - 1) - E(n_c).$$

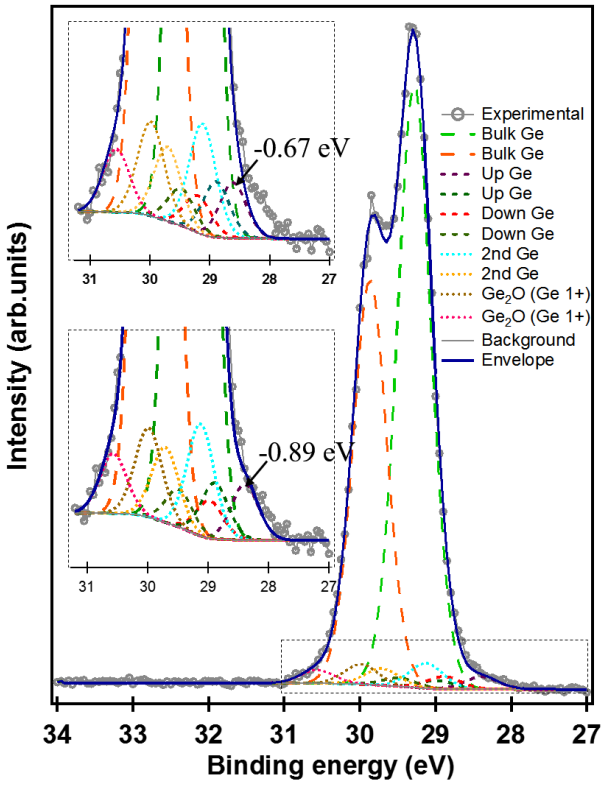

Figure 4.13. Spectral fitting of the high resolution Ge 3*d* spectrum for bare Ge. The dashed frame is presented in a magnified view in the insets for two different deconvolution fits. In the top inset the surface core level shift for up-Ge of the tilted dimer is fit to -0.67 eV. In the bottom inset the surface core level shift for up-Ge of the tilted dimer is fit to -0.89 eV. A better fit of the Ge 3*d* feature results when a core level shift of -0.89 eV is used.

The "ejected" electron is placed in the valence or conduction band to keep the overall system neutral. In this approximation, it is assumed that the core hole remains localized on the atom at which it is created. This is the so-called final-state approximation,

in which the surrounding electrons are allowed to screen the core hole.[28,68,69] The binding energy of a core electron depends on the surrounding environment. The local environment at the surface of a solid is different than the local environment in the bulk, which leads to a shift in the binding energy. This SCLS is given by

$$E_{SCLS} = [E_{\text{surface}}(n_c - 1) - E_{\text{surface}}(n_c)] - [E_{\text{bulk}}(n_c - 1) - E_{\text{bulk}}(n_c)].$$

Table 4.1: LDA calculations of the SCLSs in eV

	LDA, $4s^2 4p^2$		LDA, $3d^{10} 4s^2 4p^2$		LDA, $4s^2 4p^2$, thick slab	
	Up atom	Down atom	Up atom	Down atom	Up atom	Down atom
Ge, 2×1 slab	-0.60	-0.36	-0.78	-0.46	-0.63	-0.40
Ge, 2×2 slab	-0.48	-0.31	-0.67	-0.44		
Ge, 4×4 slab	-0.39	-0.12				
Ge, 2×1 slab, ½ ML Ba	-0.88	-0.88	-1.34	-1.34	-0.92	-0.92
Ge, 4×4 slab, ½ ML Ba	-0.94	-0.94				
Ge, 2×1 slab, ½ ML Sr	-0.67	-0.68	-0.79	-0.79	-0.71	-0.71
Ge, 4×4 slab, ½ ML Sr	-0.74	-.074				

Note: LDA is organized by system size and valence electron configuration used. Note that there is no difference in the SCLS for the up and down atoms in systems with barium and strontium. This is because the surface dimers flattened, so there is no longer an up and a down atom.

Table 4.2: Summary of predictions and measurements of the SCLS of the germanium surface from the literature and from this work.

	SCLS (eV) – up atom	SCLS (eV) – down atom
Pehlke and Scheffler (DFT-LDA) [28]	-0.67	-0.39
Cho et al. (DFT-LDA) [70]	-0.73	-0.33
Le Lay et al. (experimental) [71]	-0.59	-0.22
This work (experimental)	-0.89	-0.39

In these calculations, we took the atoms in the middle of our slabs as bulk-like.[17,28,69] The results of our calculations of core level shifts using LDA are displayed in Table 4.1. In general, for the clean germanium surface, for most configurations considered, the SCLSs are in good agreement with previous theoretical and experimental work, a summary of which is presented in Table 4.2. With the GGA functional and $4s^2 4p^2$ ($3d^{10} 4s^2 4p^2$) valence electron pseudopotentials, we found the SCLSs to be -0.95 eV (-0.68 eV) for the up atom and -0.29 eV (-0.38 eV) for the down atoms for the 2×1 slab. Our theoretical results also qualitatively agree with the experimental results in this work. In particular, both experiment and theory show the surface dimers flatten after the adsorption of the AEM, resulting in a SCLS towards lower binding energy that is the same for all surface Ge atoms.

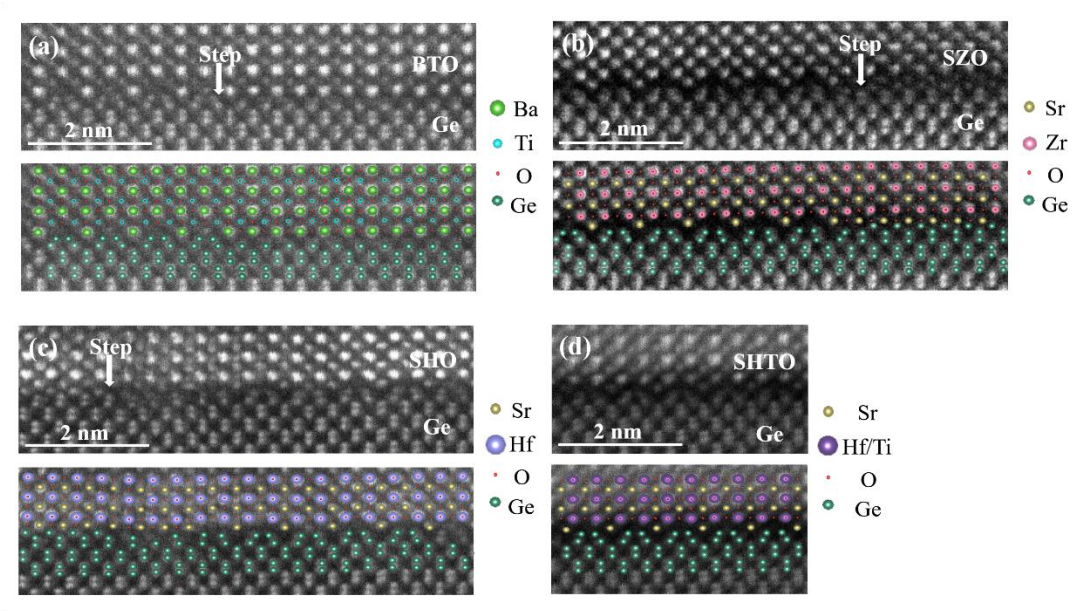

Figure 4.14. HAADF STEM images showing the interface of $BaTiO_3$ (BTO) (a), $SrZrO_3$ (SZO) (b), $SrHfO_3$ (SHO) (c) and $SrHf_{0.55}Ti_{0.45}O_3$ (SHTO) (d) films grown by ALD on Ge (001) substrates. White arrows mark the position of a single layer Ge surface step. Structural models below each image illustrate the interface structure in particular showing the change in periodicity of the Ge (001) substrate surface and the location of the Ba (or Sr) atomic columns between the Ge dimers. ((a) and (c) are reprinted with permissions from J. Mater. Res. **0**, 1 (2016).[72] (d) is reprinted with permission from MRS Commun. **6**, 125 (2016).[42] Copyright 2016 Cambridge University Press.)

The HAADF STEM studies were performed on four different crystalline perovskite oxides, namely $BaTiO_3$, $SrZrO_3$, $SrHfO_3$ and $SrHf_{0.55}Ti_{0.45}O_3$, that have been grown on Ge (001) by ALD.[41,42] The $BaTiO_3$ and $SrZrO_3$ films have not been described previously; however, all films shown in Figure 4.14 followed the same growth process.[40–42] The films were grown in the ALD system at 225 °C and each required post-deposition annealing in vacuum to achieve good crystallinity. In Figure 4.14.(a), (b) and (c), white arrows mark the one-layer Ge surface step position where the 2×1 periodicity changes to 1×1 periodicity when viewed along the [110] direction. As clearly shown in Figure 4.14, the 2×1

reconstructed Ge dimer is visible for each film with either Ba atoms or Sr atoms located at the trough between two dimer rows, which is the structure predicted for a Zintl template.

4.5. DISCUSSION

Based on these observations we posit Ba and Sr form a Zintl layer at the perovskite/Ge interface during the initial stages of Ba- and Sr-based perovskite ALD. The similar Ge binding energy shifts, spectral features and valence band shifts with exposure to Ba or Sr by ALD and MBE indicate the same phenomena are occurring on the Ge surface at submonolayer AEM coverage. The first-principles DFT calculations for Ba and Sr adsorbed in a four-fold site between dimer rows on Ge (001) predict the binding energy shifts and the flattening of the tilted dimer (Figure 4.1 and Table 4.2) in qualitative agreement with experiment (Figures 4.5,4.11,4.12). Similar calculations of AEMs on Si (001) are the basis for Zintl layer formation in that system[14,15,17] and support a similar interpretation herein on Ge (001). A Zintl layer is reasoned to form the template for MBE growth of crystalline perovskites on Si and Ge.[43,45,62] The 2×1 periodicity at the perovskite–Ge interface in the HAADF-STEM images for $BaTiO_3$ grown by MBE on Ge (001)[43] and for the four perovskites grown by ALD on Ge (100) (Figure 4.14) with either Ba atoms or Sr atoms located at the trough between the dimer rows further demonstrate the formation of a Zintl layer during ALD.

McKee showed the interfacial layer formed from Sr or Ba could be as thin as 1 ML and was associated with a strontium silicide, $SrSi_2$, for 0.5-ML Sr.[1,2] This interfacial layer is critical in protecting the Si surface from subsequent oxidation during MBE of perovskite.[9,17,22–24] Subsequent studies of this template layer formed from 0.5-ML Sr have shown the surface to be 2×1-reconstructed, with Sr in the four-fold sites between Si dimer

rows, that the binding energy and the valence band energy shift to higher energy when compared against a bare 2×1-reconstructed Si (100) surface, and that the charge transfer between Sr and the Si-dimers leads to surface core level shifts to higher energies, and that the merging of the up- and down-atom Si $3d_{5/2}$ components into one component is associated with a flattened dimer.[14,15,17,21] Demkov and Zhang interpreted the local $SrSi_2$ surface stoichiometry, which is the stoichiometry of the bulk Zintl silicide, $SrSi_2$,[73,74] as a Zintl layer.[14]

Except for the different surface reconstruction found for 0.5-ML-MBE Sr on Ge (Figure 4.3) the results reported herein for both Ba and Sr are qualitatively similar. Charge transfer from the AEM to Ge was found when using an ALD half-cycle dose at 225 °C or 0.5-ML MBE dose at 600 °C (Figure 4.4 and 4.5). This charge transfer is seen in the Ge valence band energy shift to higher energy when Ba was dosed on the surface (Figure 4.5). The 2×1-reconstructed bare Ge surface consists of dimer rows and the dimers are tilted (asymmetric) giving rise to two surface states, with the up-dimer atom filled and the down-dimer atom empty. These states are resolved as the C_u and C_d components in the Ge 3*d* spectral fitting (Figure 4.11). The asymmetric tilt of the dimer merges into one component feature, C_m, following Ba (Figure 4.11) or Sr (Figure 4.12) adsorption by ALD or MBE. On Si (001) the asymmetric tilt of the dimer was eliminated as a result of Sr atoms donating their 2 electrons to the Si (001) surface.[17] The same spectral features are found herein for Ge (001) indicating similar charge transfer and loss of asymmetry. By analogy to the interpretations offered for AEM on Si (001), the AEM atoms form a partial Zintl layer for 0.2-ML Ba or Sr derived from the ALD half-cycle, and they form a Zintl layer for the 0.5-ML-MBE Ba or Sr coverages on Ge (001).

The DFT results showed the surface dimers symmetrize (flatten) upon adsorption of 0.5-ML of Ba and Sr (Figure 4.1) and that the surface core levels for the up and down

dimers merge upon adsorption of the 0.5-ML of Ba and Sr (Table 4.1). As mentioned above, for most configurations of the clean Ge surface considered, the SCLSs (see Table 4.1) are in good agreement with previous theoretical and experimental work (see Table 4.2). However, the theoretical predictions do somewhat depend on the choice of the functional, slab thickness, and in-plane area of the simulation slab. Furthermore, screening depends on the band gap of the system. Since both LDA and GGA underestimate the band gap for germanium, the screening is exaggerated. This is especially important for the systems with 0.5-ML of barium and strontium, which are metallic in this theory. This is not a problem for similar studies done for silicon, where the band gap is maintained for with 0.5-ML of Sr adsorbed on the surface.[14] We find that the SCLSs for germanium (001) surface with 0.5-ML of barium and strontium are negative (towards lower binding energy), which matches the experimental results for both ALD and MBE growth. Furthermore, the theoretical SCLS is the same for both atoms in the Ge surface dimer, which indicates the dimer has flattened after the adsorption of the Ba and Sr, just as was observed experimentally. The magnitude of the SCLS is larger for barium than for strontium, also in qualitative agreement with experiment. However, the absolute value of the shift is overestimated for both metals, for the reasons discussed above.

During ALD exposures the Ge (001) surface gets contaminated with a carbonaceous material. An ALD half-cycle leads to 1.0 ML of carbon, *i.e.*, 5:1 C:Ba (:Sr), that does not increase with continued dosing, even as the Ba coverage increases (Figure 4.6.(b) and 4.8). The same 1-ML coverage is found upon exposure of a clean Ge (001) surface to the ALD chamber for 1 min (Fig. 7). Cycloaddition reactions of organic molecules containing C–C double bonds are common on Ge (001),[75] and it is conceivable that ligands either come directly from the precursor during adsorption of barium- or strontium-bis(triisopropylcyclopentadienyl) precursors or from

triisopropylcyclopentadienyl ligands that could desorb from the ALD chamber walls bind to the Ge (001) surface through a cycloaddition reaction. These ligands might be expected to persist on the Ge surface for a few ALD cycles that alternate between the precursor and water exposure.

It is possible the carbon associated with these bound ligands somehow contribute to the binding energy shift found for Ge (Figure 4.5). The AEM binding energy decreases with increasing coverage for MBE-dosed samples (Figure 4.2 and 4.4). The ALD half-cycle led to 0.2 ML of Ba or Sr and gave the same Ge binding energy shift as the corresponding 0.5-ML MBE dose (Figure 4.4). A GeC monolayer has been reported with a Ge 3*d* binding energy of 29.8 eV versus 29.4 eV for clean Ge,[76] providing precedence for carbon to contribute to the greater BE found for 0.2-ML AEM when it originates from an organometallic precursor than the BE that might be expected for this AEM coverage.

ALD of the ABO_3 perovskite films presented in Figure 4.14 led to amorphous films that required annealing between 500 and 650 °C to crystallize the deposited film into a heteroepitaxial layer on Ge (001).[41,42] The first complete ALD cycle produces 0.4-ML of Sr or Ba (Figure 4.9). Following this 0.4-ML Sr/Ba deposition the B element of the perovskite is introduced via a molecular precursor, and then A is deposited again. The RHEED and XPS results herein show the Sr/Ba in the first ALD half-cycle adsorb on the Ge (001) surface and form a partial Zintl layer. We propose the Zintl layer, $SrGe_x$ or $BaGe_x$, is completed during the first few ALD cycles and this Zintl layer forms a template from which the epitaxial film crystalizes during the annealing step. The strongest evidence in support of the interfacial Zintl layer is found in the HAADF-STEM images (Figure 4.14) that show the Sr or Ba located at the trough between the dimer rows.

4.6. SUMMARY

The organic ligands dissociate from the precursor after precursor adsorption on the Ge (001) surface, producing the same Zintl template critical for perovskite growth on Group IV semiconductors during molecular beam epitaxy. We find that the initial dosing of the barium- or strontium- bis(triisopropylcyclopentadienyl) precursors on a clean Ge surface produces a surface phase that has the same chemical and structural properties as the 0.5-monolayer Ba Zintl layer formed when depositing Ba by molecular beam epitaxy. Similar binding energy shifts are found for Ba, Sr and Ge when using either molecular or atomic metal sources. Germanium surface core level shifts reveal the tilted Ge surface dimers flatten for molecular and atomic metal sources. Similar binding energy shifts and changes in dimer tilting with alkaline earth metal adsorption are found with density functional theory calculations. High angle angular dark field scanning transmission microscopy images of $BaTiO_3$, $SrZrO_3$, $SrHfO_3$ and $SrHf_{0.55}Ti_{0.45}O_3$ reveal the location of the Ba (or Sr) atomic columns between the Ge dimers and reinforce the formation of a Zintl layer at the onset of ALD.

4.6. REFERENCES

1 R. A. McKee, F. J. Walker, and M. F. Chisholm, Phys. Rev. Lett. **81**, 3014 (1998).

2 R. A. McKee, F. J. Walker, and M. F. Chisholm, Science **293**, 468 (2001).

3 M. Jahangir-Moghadam, K. Ahmadi-Majlan, X. Shen, T. Droubay, M. Bowden, M. Chrysler, D. Su, S.A. Chambers, and J.H. Ngai, Adv. Mater. Interfaces **2**, 1400497 (2015).

4 R. Droopad, Z. Yu, H. Li, Y. Liang, C. Overgaard, A. Demkov, X. Zhang, K. Moore, K. Eisenbeiser, M. Hu, J. Curless, and J. Finder, J. Cryst. Growth **251**, 638 (2003).

5 J. W. Reiner, A. Posadas, M. Wang, M. Sidorov, Z. Krivokapic, F. J. Walker, T. P. Ma, and C. H. Ahn, J. Appl. Phys. **105**, 124501 (2009).

6 M. Sousa, C. Rossel, C. Marchiori, H. Siegwart, D. Caimi, J.-P. Locquet, D. J. Webb, R. Germann, J. Fompeyrine, K. Babich, J. W. Seo, and C. Dieker, J. Appl. Phys. **102**, 104103 (2007).

7 A. A. Demkov, A. B. Posadas, H. Seo, M. Choi, K.J. Kormondy, P. Ponath, R. C. Hatch, M. D. McDaniel, T. Q. Ngo, and J. G. Ekerdt, ECS Trans. **54**, 255 (2013).

8 M. P. Warusawithana, C. Cen, C. R. Sleasman, J. C. Woicik, Y. Li, L. F. Kourkoutis, J. A. Klug, H. Li, P. Ryan, L.-P. Wang, M. Bedzyk, D. A. Muller, L.-Q. Chen, J. Levy, and D.G. Schlom, Science **324**, 367 (2009).

9 Z. Yu, Y. Liang, C. Overgaard, X. Hu, J. Curless, H. Li, Y. Wei, B. Craigo, D. Jordan, R. Droopad, J. Finder, K. Eisenbeiser, D. Marshall, K. Moore, J. Kulik, and P. Fejes, Thin Solid Films **462**–**463**, 51 (2004).

10 S.-H. Baek and C.-B. Eom, Acta Mater. **61**, 2734 (2013).

11 V. Vaithyanathan, J. Lettieri, W. Tian, A. Sharan, A. Vasudevarao, Y. L. Li, A. Kochhar, H. Ma, J. Levy, P. Zschack, J. C. Woicik, L. Q. Chen, V. Gopalan, and D. G. Schlom, J. Appl. Phys. **100**, 024108 (2006).

12 J. W. Reiner, A. M. Kolpak, Y. Segal, K. F. Garrity, S. Ismail-Beigi, C. H. Ahn, and F. J. Walker, Adv. Mater. **22**, 2919 (2010).

13 Y. Liang, J. Kulik, T. C. Eschrich, R. Droopad, Z. Yu, and P. Maniar, Appl. Phys. Lett. **85**, 1217 (2004).

14 A. A. Demkov and Z. Xiaodong, J. Appl. Phys. **103**, (2008).

15 H. Seo, M. Choi, A. B. Posadas, R. C. Hatch, and A. A. Demkov, J. Vac. Sci. Technol. B **31**, 04D107 (2013).

16 J. Wang, J. A. Hallmark, D. S. Marshall, W. J. Ooms, P. Ordejón, J. Junquera, D. Sánchez-Portal, E. Artacho, and J.M. Soler, Phys. Rev. B **60**, 4968 (1999).

17 M. Choi, A. B. Posadas, H. Seo, R. C. Hatch, and A. A. Demkov, Appl. Phys. Lett. **102**, 031604 (2013).

18 X. Zhang, A. A. Demkov, H. Li, X. Hu, Y. Wei, and J. Kulik, Phys. Rev. B **68**, 125323 (2003).

19 X. Yao, X. Hu, D. Sarid, Z. Yu, J. Wang, D. S. Marshall, R. Droopad, J. K. Abrokwah, J. A. Hallmark, and W. J. Ooms, Phys. Rev. B **59**, 5115 (1999).

20 X. Hu, X. Yao, C. A. Peterson, D. Sarid, Z. Yu, J. Wang, D. S. Marshall, J. A. Curless, J. Ramdani, R. Droopad, J. A. Hallmark, and W. J. Ooms, Surf. Sci. **457**, L391 (2000).

21 C. R. Ashman, C.J. Först, K. Schwarz, and P.E. Blöchl, Phys. Rev. B **69**, 075309 (2004).

22 Y. Liang, S. Gan, Y. Wei, and R. Gregory, Phys. Status Solidi B **243**, 2098 (2006).

23 K. D. Fredrickson, H. Seo, and A. A. Demkov, J. Appl. Phys. **120**, 065301 (2016).

24 Y. Wei, X. Hu, Y. Liang, D. C. Jordan, B. Craigo, R. Droopad, Z. Yu, A. Demkov, J. L. E. Jr, and W. J. Ooms, J. Vac. Sci. Technol. B **20**, 1402 (2002).

25 D. M. Goodner, D. L. Marasco, A. A. Escuadro, L. Cao, and M. J. Bedzyk, Phys. Rev. B **71**, 165426 (2005).

26 L. C. Allen, J. Am. Chem. Soc. **111**, 9003 (1989).

27 C.-P. Cheng, I.-H. Hong, and T.-W. Pi, Phys. Rev. B **58**, 4066 (1998).

28 E. Pehlke and M. Scheffler, Phys. Rev. Lett. **71**, 2338 (1993).

29 L. Spiess, A.J. Freeman, and P. Soukiassian, Phys. Rev. B **50**, 2249 (1994).

30 A. Cattoni, R. Bertacco, M. Cantoni, F. Ciccacci, H. Von Kaenel, and G.J. Norga, Appl. Surf. Sci. **254**, 2720 (2008).

31 B. R. Lukanov, J. W. Reiner, F. J. Walker, C. H. Ahn, and E. I. Altman, Phys. Rev. B **84**, 075330 (2011).

32 B. Lukanov, K. Garrity, S. Ismail-Beigi, and E. I. Altman, Phys. Rev. B **85**, 195316 (2012).

33 J.-G. Cheng, J.-S. Zhou, J. B. Goodenough, and C.-Q. Jin, Phys. Rev. B **85**, 184430 (2012).

34 G. H. Jonker and J. H. Van Santen, Physica **19**, 120 (1953).

35 C. H. Ahn, K. M. Rabe, and J.-M. Triscone, Science **303**, 488 (2004).

36 N. Nuraje and K. Su, Nanoscale **5**, 8752 (2013).

37 S. Dong and J.-M. Liu, Mod. Phys. Lett. B **26**, 1230004 (2012).

38 G. Catalan and J. F. Scott, Adv. Mater. **21**, 2463 (2009).

39 J. G. Bednorz and K. A. Müller, Rev. Mod. Phys. **60**, 585 (1988).

40 M. D. McDaniel, T. Q. Ngo, A. Posadas, C. Hu, S. Lu, D. J. Smith, E. T. Yu, A. A. Demkov, and J. G. Ekerdt, Adv. Mater. Interfaces **1**, 1400081 (2014).

41 M. D. McDaniel, C. Hu, S. Lu, T. Q. Ngo, A. Posadas, A. Jiang, D. J. Smith, E. T. Yu, A. A. Demkov, and J. G. Ekerdt, J. Appl. Phys. **117**, 054101 (2015).

42 S. Hu, M. D. McDaniel, A. Posadas, C. Hu, H. Wu, E. T. Yu, D. J. Smith, A. A. Demkov, and J. G. Ekerdt, MRS Commun. **6**, 125 (2016).

43 K. D. Fredrickson, P. Ponath, A. B. Posadas, M. R. McCartney, T. Aoki, D. J. Smith, and A. A. Demkov, Appl. Phys. Lett. **104**, 242908 (2014).

44 M. D. McDaniel, A. Posadas, T. Wang, A. A. Demkov, and J. G. Ekerdt, Thin Solid Films **520**, 6525 (2012).

45 M. Choi, A. Posadas, R. Dargis, C.-K. Shih, A. A. Demkov, D. H. Triyoso, N. D. Theodore, C. Dubourdieu, J. Bruley, and J. Jordan-Sweet, J. Appl. Phys. **111**, 064112 (2012).

46 T. Q. Ngo, A. B. Posadas, M. D. McDaniel, C. Hu, J. Bruley, E. T. Yu, A. A. Demkov, and J. G. Ekerdt, Appl. Phys. Lett. **104**, 082910 (2014).

47 Manufactured and supplied by Air Liquide ALOHA Electronics Performance Materials, Air Liquide Electronics U.S. LP, Houston, TX.

48 S. Rentrop, T. Moebus, B. Abendroth, R. Strohmeyer, A. Schmid, T. Weling, J. Hanzig, F. Hanzig, H. Stöcker, and D. C. Meyer, Thin Solid Films **550**, 53 (2014).

49 M. P. Seah and W. A. Dench, Surf. Interface Anal. 2 (1979).

50 G. Kresse and J. Hafner, Phys. Rev. B **47**, 558 (1993).

51 G. Kresse and J. Hafner, Phys. Rev. B **49**, 14251 (1994).

52 G. Kresse and J. Furthmüller, Comput. Mater. Sci. **6**, 15 (1996).

53 G. Kresse and J. Furthmüller, Phys. Rev. B **54**, 11169 (1996).

54 P. E. Blöchl, Phys. Rev. B **50**, 17953 (1994).

55 G. Kresse and D. Joubert, Phys. Rev. B **59**, 1758 (1999).

56 J. P. Perdew and A. Zunger, Phys. Rev. B **23**, 5048 (1981).

57 J. P. Perdew, K. Burke, and M. Ernzerhof, Phys. Rev. Lett. **77**, 3865 (1996).

58 J. P. Perdew, K. Burke, and M. Ernzerhof, Phys. Rev. Lett. **78**, 1396 (1997).

59 H. J. Monkhorst and J. D. Pack, Phys. Rev. B **13**, 5188 (1976).

60 R. E. Schlier and H. E. Farnsworth, J. Chem. Phys. **30**, 917 (1959).

61 D. J. Chadi, J. Vac. Sci. Technol. **16**, 1290 (1979).

62 P. Ponath, K. Fredrickson, A. B. Posadas, Y. Ren, X. Wu, R. K. Vasudevan, M. Baris Okatan, S. Jesse, T. Aoki, M.R. McCartney, D.J. Smith, S.V. Kalinin, K. Lai, and A. A. Demkov, Nat. Commun. **6**, 6067 (2015).

63 J. H. Ngai, D. P. Kumah, C. H. Ahn, and F. J. Walker, Appl. Phys. Lett. **104**, 062905 (2014).

64 C. Merckling, G. Saint-Girons, C. Botella, G. Hollinger, M. Heyns, J. Dekoster, and M. Caymax, Appl. Phys. Lett. **98**, 092901 (2011).

65 J. F. Moulder, W. F. Stickle, P. E. Sobol, and K. D. Bomben, Perkin-Elmer Phys. Electron. Div. (1993).

66 A. D. Katnani and G. Margaritondo, Phys. Rev. B **28**, 1944 (1983).

67 W.-J. Lee, J. W. Ma, J. M. Bae, S. H. Park, M.-H. Cho, and J. P. Ahn, CrystEngComm **13**, 5204 (2011).

68 W. F. Egelhoff, Surf. Sci. Rep. **6**, 253 (1987).

69 S. Lizzit, A. Baraldi, A. Groso, K. Reuter, M. V. Ganduglia-Pirovano, C. Stampfl, M. Scheffler, M. Stichler, C. Keller, W. Wurth, and D. Menzel, Phys. Rev. B **63**, 205419 (2001).

70 J.-H. Cho, S. Jeong, and M.-H. Kang, Phys. Rev. B **50**, 17139 (1994).

71 G. Le Lay, J. Kanski, P. O. Nilsson, U. O. Karlsson, and K. Hricovini, Phys. Rev. B **45**, 6692 (1992).

72 D. J. Smith, H.-W. Wu, S. Lu, T. Aoki, P. Ponath, K. Fredrickson, M. D. McDaniel, E. Lin, A. B. Posadas, A. A. Demkov, J. G. Ekerdt, and M. R. McCartney, J. Mater. Res. **0**, 1 (2016).

73 E. Zintl and W. Dullenkopf, Z Phys Chem Abt B **16**, 183 (1932).

74 E. Zintl, Angew. Chem. **52**, 1 (1939).

75 P. W. Loscutoff and S. F. Bent, Annu. Rev. Phys. Chem. **57**, 467 (2006).

76 J.-M. Mackowski, B. Cimma, R. Pignard, P. Colardelle, and P. Laprat, Window and Dome Technologies and Materials III, SPIE 1760, (San Diego, California, American), pp. 201-209 (1992).

Chapter 5: Crystalline $SrZrO_3$ deposition on Ge (001) by atomic layer deposition for high-*k* dielectric application

5.1. INTRODUCTION

Crystalline perovskites have received increased attention due to their multiple properties, such as dielectric, piezoelectric, ferroelectric, ferromagnetic, etc.[1,2] McKee first reported epitaxial growth of $SrTiO_3$ (STO) on silicon in 1998.[3] The study of crystalline perovskites on semiconductors has been widely expanded subsequently for device applications,[4–13] including the use of crystalline perovskites as a high-*k* gate oxide for field-effect transistor device applications.

In the past decades, the goals of faster computing speed and lower power consumption have led to ever smaller transistor feature sizes and ever thinner gate oxides thicknesses. Unacceptable leakage current for SiO_2 on silicon[14] led to a search for other gate oxide materials and ultimately channel materials other than silicon. For high dielectric constant materials, the *k* value should be over 12, preferably 25 to 35.[15] Previous work in our group has studied the deposition of crystalline $SrHfO_3$ (SHO), STO and $SrHf_xTi_{1-x}O_3$ (SHTO) on Ge (001) by atomic layer deposition (ALD). The titanium-based perovskites display a large leakage current because of the negligible conduction bandset offset with the Ti 3*d* states and Si and Ge.[16–18] While the STO/Ge heterojunction achieved *k*~90 and an equivalent oxide thickness (EOT) of 0.7 nm, the leakage current was around 10 A/cm^2 at 0.7 MV/cm.[19] Substituting Hf onto the Ti sites led to a lower dielectric constant, larger EOT and lower leakage current with values of *k*~30, an EOT of 1.8 nm, and a leakage current of 0.1 A/cm^2 at 1 MV/cm for $SrHf_{0.55}Hf_{0.45}O_3$.[9] SHO displayed *k*~17, an EOT of 1.0 nm and a leakage current of ~6.3×10^{-6} A/cm^2 at 1.0 MV/cm1.0 nm.[10] While the

leakage current and EOT for SHO/Ge were comparable to state-of-the-art Ge-based metal oxide semiconductor field effect transistors (MOSFETs), the interface trap density (D_{it}) ~5×10^{13} $cm^{-2}eV^{-1}$ of crystalline $SrHfO_3$ on Ge needed improvement.[20] Annealing temperatures above 650 °C were required to realize crystalline SHO films and this led to an amorphous interfacial layer of several Angstroms that may have contributed to the D_{it} values. Zirconium, with an atomic mass ~0.5 that of Hf, is expected to reduce the crystallization temperature of thin $SrZrO_3$ (SZO) when compared to SHO.[9]

Strontium zirconate has a comparable conduction band offset (CBO) to SHO with Ge, with values of 1.41-1.77 eV and 2.17 eV for SZO/Ge and SHO/Ge, respectively, and SHO has a dielectric constant *k* around 30.[10,13,21] Several groups have studied growth of crystalline SZO deposition by molecular beam epitaxy (MBE) or pulse laser deposition (PLD).[13,21,22] Herein we report ALD growth of crystalline SZO, and approaches to lower the D_{it} through steps taken prior to ALD and by annealing in a flux of atomic deuterium. Comparison of various Column 4 B-site cations in ALD-grown crystalline ABO_3 perovskites shows Zr to perform the best among Ti, Zr and Hf in terms of leakage current and D_{it}.

The channel material also plays a significant role in MOSFET performance. Silicon is the most common substrate and further transistor scaling requires the channel material have higher mobility, which can lead to higher drive current.[23–25] Compared to Si, the electron mobility and hole mobility for Ge are 3900 vs 1400 cm^2/Vs and 1900 vs 500 cm^2/Vs, respectively, which makes Ge viable as a next generation channel material. [25,26] In addition, Ge has a more unstable oxide than Si and making it easier to remove the native oxide to achieve a clean surface.[27–29]

A high D_{it} can affect the channel mobility and negate the mobility advantages of Ge.[25] Defects at the interface of Ge-based heterojunctions are mainly formed by dangling

bonds.[25,30] Ge substrate roughness also increases D_{it}.[9,31] Several groups have employed different methods to lower the interface trap density;[20,32–39] one method uses GeO_x as a passivation layer to yield D_{it} values in the low 10^{11} cm^{-2} eV^{-1} range.[34,37–41] However the passivation layer increases the EOT. The smoothness of a Ge surface can be improved with oxygen plasma treatment.[28] Zhang et al., used used post-deposition annealing to treat $Al_2O_3/GeO_x/n$-Ge in ambients of N_2, forming gas, H_2, D_2, atomic H, and atomic D to heal dangling bonds; the the atomic D treatment led to the best effective electron mobility.[42] D desorption yields are 50 times lower than the H yields on Si;[43] and a lower yield should also be expected for D on Ge. Atomic deuterium treatment is reported herein for crystalline SZO/Ge interfaces that do not feature an interfacial oxide.

5.2. EXPERIMENT

5.2.1. GE SUBSTRATE PREPARATION

The growth facility has been previously described.[44] It includes an ALD chamber, a surface analysis chamber, a molecular beam epitaxy chamber, and a deuterium dosing chamber (described below) all connected with a transfer tube so the samples remain *in situ* between treatment, growth and analysis. The 4-inch Ge wafers (n-type, Sb-doped, 0.1-0.5 Ω·cm resistivity) were purchased from MTI Corp. and diced into 18×20 mm^2 pieces. After degreasing the Ge substrate with acetone, isopropyl alcohol and deionized water in an ultrasonic bath, two preparation methods were used to remove the residual carbon contamination and produce the 2×1-reconstructed Ge (001) surface that is the necessary template for perovskite growth by ALD.[19] Method A is the same procedure as previous work,[9,10,19,45] in which a 30-min UV/ozone exposure is followed with 1 h thermal annealing at 700°C in vacuum (<2×10^{-9} torr) to remove any native oxide. Method B uses an oxygen

plasma to remove the residual carbon contamination instead of UV/ozone exposure and to lower the surface roughness. In Method B the sample is loaded into the vacuum system after degreasing and is transferred to the MBE chamber. An oxygen plasma with 1.2×10^{-5} torr background oxygen pressure and 300 W forward power is estimated to produce an atomic oxygen flux of $\sim5\times10^{13}$ cm^{-2} s^{-1}.[28] During the 30-min oxygen plasma exposure the substrate temperature is 100 °C. Following plasma treatment, 1 h thermal annealing at 700 °C is applied to remove the native GeO_2.

In situ reflection high-energy electron diffraction (RHEED) (Staib Instruments operating at 21 keV) is used to verify the reconstructed surface structure for Methods A and B. The clean Ge (001) sample is transferred *in vacuo* to the surface analysis chamber fitted with an x-ray photoelectron spectrometer to verify the Ge surface composition. Following the thermal deoxidization process at 700 °C some samples were heated to 600 °C for Zintl template preparation.[45] The Zintl template consisting of 0.5 monolayer (ML) of Ba is prepared by depositing atomic Ba in the MBE chamber on the dexoxidized Ge (001) surface. *In situ* RHEED confirmed the 2×1 reconstructed surface structure for the Zintl template and the Ba flux rate was calibrated to 1ML/min by a quartz crystal monitor in MBE.[45]

5.2.2. FILM GROWTH

The bare Ge and Zintl-templated Ge substrate were transferred *in situ* to the ALD chamber for $SrZrO_3$ (SZO) seed layer growth at 225 °C with 1 torr Ar flow as the carrier gas. Strontium bis(triisopropylcyclopentadienyl) from Air Liquid and tetrakis (dimethylamido) zirconium (IV) from Sigma-Aldrich were used as the Sr and Zr precursor

and were heated to 130 and 60 °C, respectively. H_2O, maintained at room temperature, was used as the oxygen source. Each unit cycle includes 2-s precursor dosing, 1-s H_2O dosing and 20-s Ar purging following each reactant exposure. When growing the slightly Sr rich film, the cycle ratio was Sr: Zr = 3:2 on bare Ge (001). On Zintl-templated Ge (001), a cycle ratio of Sr: Zr=2:1 was found to work best.

The first seed layer (20 ALD cycles and ~3 nm thick) always grew as an amorphous film, so post deposition annealing is required to obtain the single crystalline film. The sample was transferred back to the MBE chamber in vacuum and heated to the crystallization temperature with a 10°C min^{-1} heating rate. The onset of crystalline is defined as the initial appearance of a diffraction spot in RHEED as described in previous work.[9] The sample temperature was then ramped up another 30 °C and maintained for 5 min to achieve better crystallinity. During the annealing process, RHEED was used to observe transformation from an amorphous to a crystalline film in real time. Attaining single crystalline SZO film above 3 nm thickness required a two-step growth process. After annealing the 3-nm amorphous SZO film to achieve single crystalline SZO, the sample was transferred back to ALD chamber for thicker film growths with a Sr:Zr=3:2 cycle ratio. The second SZO layer was crystalline as deposited and the crystallinity was improved with post deposition annealing to around 550 °C without pausing.

5.2.3. ATOMIC DEUTERIUM TREATMENT

An atomic deuterium source chamber was home-built built. Atomic deuterium was generated by the tungsten filament of a 400-W Osram Xenophot bulb, which had part of the glass enclosure removed to expose the filament. A current of 5.2 A was supplied by

a DC power supply (KEPCO, MSK10-10M) to the tungsten filament and filament temperature was ~1800 K, which was calibrated by a thermal pyrometer. At this temperature, the tungsten filament could crack deuterium molecule to generate atomic deuterium.[46] The pressure of deuterium gas (99.999%; Matheson) was controlled by a leak valve and maintained at 5.0×10^{-6} torr in the chamber. The flux of atomic deuterium was estimated around 2×10^{13} D/cm^2·s based on the previous work.[47] The sample was positioned approximately 4 cm above, and faced toward the tungsten filament. A pyrolytic boron nitride heater from Momentive was fixed 2 cm above the sample and maintained the sample temperature at 350 °C during the treatment. The treatment time ranging from 1 to 3 h was adjusted for different sample thicknesses.

5.2.4. CHARACTERIZATION

In addition to RHEED that was used to monitor the Ge surface reconstruction and the film surface order that is used to track the crystalline process, *in situ* x-ray photoelectron spectroscopy (XPS) was also applied to confirm the Ge surface composition and stoichiometry of SZO films. The XPS was equipped with a monochromatic Al Kα source at 1486.6 eV and a VG Scienta R3000 electron energy analyzer, which is calibrated by a clean Ag foil. To obtain the spectra of Sr 3*d*, Zr 3*d*, Ge 3*d* and C 1*s* core levels, the basic settings were 100 eV pass energy with a 0.4 mm analyzer slit width and 50 meV steps with 157 ms/step dwell time. At this condition, the spectrometer yielded around 350 meV effective resolution. CasaXPS (Version 2.3.16 PR 1.6) was used to analyze the results. The atomic sensitivity factors for Sr 3*d* and Zr 3*d* were set as 1.843 and 2.576, respectively.[48]

For *ex situ* characterization, the film thickness was measured by x-ray reflectivity (XRR) and crystallinity was analyzed by x-ray diffraction (XRD) and rocking curve on a Rigaku Ultima IV system with a Cu Kα source. The high-angle annular-dark-field scanning transmission electron microscopy (HAADF-STEM) was employed here to investigate the grown film and interface. The samples were prepared via standard cross-section method with Ar ion milling and STEM images were taken with a JEOL ARM 200F operated at 200 kV.

Metal oxide semiconductor capacitor (MOS capacitor) structures fabricated by a lift-off process to study the electrical properties, which include dielectric constant *k*, leakage current *J* and interface trap density D_{it}.[23,25] The 100 μm×100 μm square top electrode contacts of Pt were applied by E-beam evaporation. The back side of the substrate was scratched and silver paste was applied to form the bottom electrode. The capacitance-voltage (C-V) and current-voltage (I-V) measurements were performed on an Agilent B1500A semiconductor device parameter analyzer with a Cascade Microtech probe station. A cryogenic probe stations from Lakeshore Cryotronics was used for low temperature D_{it} measurement at 250K.

5.3. Results and Discussion

5.3.1. Ge substrate pretreatment

Figure 5.1 shows the RHEED images indicating the surface structure changes during the Ge substrate pretreatment process. The Ge surface structure is transformed from a 1×1- to 2×1-reconstructed structure after thermal annealing to remove oxygen, which demonstrates Ge surface dimer formation. The 2×1-reconstructed Ge substrate was found

to be necessary for ALD and MBE growth of crystalline perovskites.[19,49] The samples treated by UV/ozone and by the oxygen plasma have the same RHEED patterns after oxygen treatment Figure 5.1.(b) and after thermal annealing to remove oxygen Figure 5.1.(c) as illustrated for an oxygen plasma-treated sample. The weaker 1×1 pattern in Figure 5.1.(b) than Figure 5.1.(a) is a consequence the thicker oxide layer that forms during oxygen plasma treatment. Any native carbon contamination of Ge (001) is removed by either the UV/ozone or oxygen plasma process[19,28] and the native oxide is removed after thermal annealing.[9,19] Oxygen plasma treatment was used to achieve a flatter reconstructed Ge (001) surface with fewer steps than are found using a UV/ozone treatment.[28] Fewer surface steps can help to reduce the defects at the interface and lower the anti-phase boundary (APB) formation in films.[9,50]

Over time the ALD chamber accumulates $^{i}Pr_3Cp$ ligands or $^{i}Pr_3Cp$-derived molecules on the chamber surfaces that likely adsorb on bare Ge (001) and produce about 1 ML-equivalent of carbon contamination on the Ge (001) surface.[45] A recent study found a Zintl template formed by adsorbing 0.5 ML Ba on Ge (001) by MBE, could prevent the carbon adsorption in the ALD chamber.[51] The Zintl templated-surface formed with Ba retains the reconstructed surface structure as shown in Figure 5.1.(d). The sharper 2×1 pattern following Zintl layer formation indicates the long range order and cleanliness of the Ge surface. *In situ* XPS was used to check the surface composition for both Zintl-templated and clean bare Ge.[51] XPS results also verify the Zintl template is free of carbon and oxygen.[45]

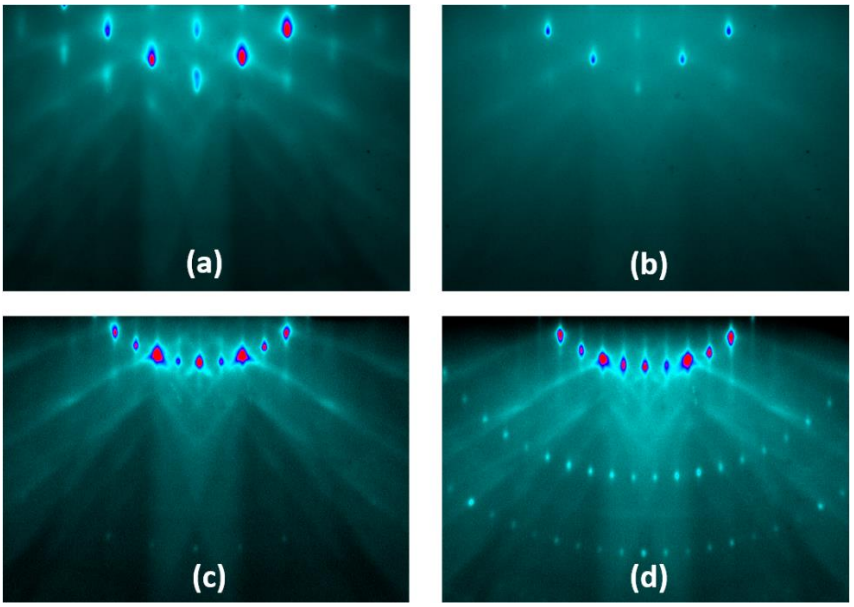

Figure 5.1. Ge (001) surface observation by RHEED along the [110] zone axis, (a) prior to oxygen plasma treatment (b) after oxygen plasma treatment for 30 min (c) after 1 h vacuum annealing at 700°C. (d) Zintl template formation by 0.5-ML Ba deposition on Ge. All images are taken at a 200 °C substrate temperature with the same filament intensity.

5.3.2. DEPOSITION AND CRYSTALLIZATION OF $SrZrO_3$

The SZO films above 3 nm thickness required a two-step growth procedure in which thicker films are deposited on a crystallized layer of SZO. As shown in Figure 5.2.(a), the first seed layer grows as an amorphous film on Zintl template. With vacuum annealing at 630 °C for 5 min, the first layer of SZO transforms from amorphous to crystalline. The second layer grows as a crystalline layer at 225 °C. Sharper RHEED patterns can be realized by annealing at 550 °C (Figure 5.2.(b)). Similar results were found with STO where a crystalline seed layer enabled subsequent STO growth as a crystalline film.[52] The SZO films grown on bare Ge (001) required the same two-step procedure in

which the 2-3 nm amorphous films were annealed to crystallize the film (RHEED images not shown). The crystallization temperature for the seed layer on bare Ge is around 590°C, which is lower than $SrHfO_3$ (at~650 °C) but higher than $SrTiO_3$ (at ~510 °C) on bare Ge (001).[9] This is consistent with the observation that the crystallization temperature in $SrMO_3$ amorphous thin films is be influenced by the atomic weight of atom M.[9]

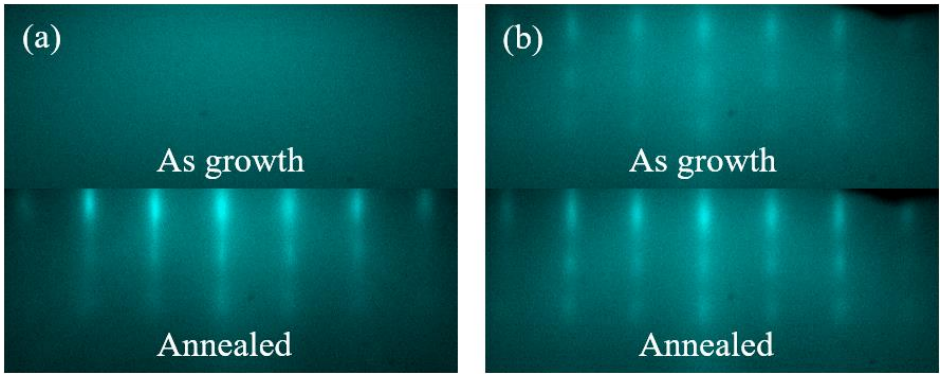

Figure 5.2. RHEED images of two step growth for a 6.2-nm $SrZrO_3$ film on Zintl template Ge before and after annealing, (a) the first layer is around 2 nm (b) the second layer is 4.2 nm. All images were taken by the beam was aligned along <110> directions.

On bare Ge (001), the SZO seed layer is grown with cycle ratio of Sr: Zr= 3:2 and 20 unit cycles in total (~3nm), which results in 49.3% Sr+Ba and 50.7% Zr (metals basis) by XPS. On Zintl-templated Ge, the same cycle ratio of Sr:Zr=3:2 will lead to SZO stoichiometry of 45.9% of Sr+Ba and 55.1% Zr, Films with this stoichiometry crystallize at 640°C. A higher Sr cycle is needed on Zintl-templated Ge. With a Sr:Zr=2:1 cycle ratio and total 20 unit cycles, the stoichiometry is 49.9% Sr and 50.1% Zr and the crystallization temperature is around 600°C.

The previous study showed that the bare 2×1 Ge (001) surface could decompose the Sr precursor to form adsorbed Sr atoms that feature many of the same binding energy

shifts as MBE-deposited Sr or Ba atoms.[45] However, higher-order reconstructions of Ge (001) were found with Sr than the 2×1 reconstruction with 0.5-ML Ba that creates the Zintl template. This Ba-based Zintl template protects the Ge (001) surface from C incorporation from the precursor ligands and oxide formation from the H_2O ALD oxidant.[51] For reasons beyond the scope of this study strontium bis(triisopropylcyclopentadienyl) appears less reactive on a Zintl-templated surface than on a bare Ge (001) surface necessitating the higher Sr cycle of Sr:Zr=2:1 to obtain stoichiometric films. The amorphous SZO on the Zintl-templated surface starts to crystallize at 640 °C while the amorphous SZO on the bare surface starts to crystallize at 590 °C. The annealing temperature, which we adopt as 30 °C higher than crystallization temperature, is a significant factor to determine the interface quality. Higher annealing temperature will increase the possibility to form a blurry interface.[9,10] As shown in Figure 5.3.(a) the SZO seed layer annealed at 620 °C features sharp interface in HAADF-STEM with Sr atoms located between the dimer rows as expected of a Zintl layer.[45,53] The SZO seed layer annealed at 670°C does not feature a sharp at the interface interface in HAADF-STEM (Figure 5.3.(b)). The amorphous region at interface could indicate the Ge mixed or diffused into the SZO film at the higher annealing temperature. A similar interfacial reaction was observed when $SrHfO_3$ was annealed on Ge above 650 °C. Since the interfacial reaction might lead to higher interface trap density, the annealing temperature is controlled below 640°C in this work by using 2:1 of Sr to Zr ALD cycle ratio on Zintl template and 3:2 on bare Ge (001).

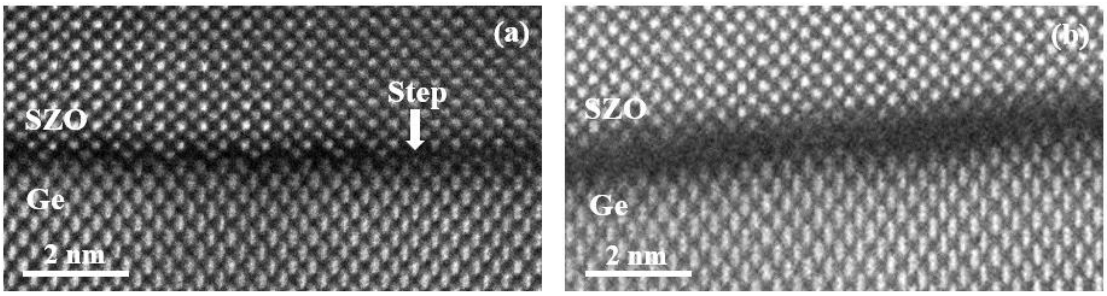

Figure 5.3. HAADF-STEM images of (a) $SrZrO_3$ on bare Ge (001) annealed at 620 °C, (b) $SrZrO_3$ on Zintl-templated Ge (001) annealed at 670 °C.

Regardless of bare Ge or a Zintl template, the second layer of SZO has the same growth cycle ratio of Sr:Zr=3:2 and crystallizes as it grows. Post deposition annealing at 550°C is applied for all second-layer SZO films to improve the crystal quality. Based on the XPS the composition for the SZO films is 53.0% of Sr and 47.0% of Zr. This result is consistent with previous work that showed Sr-rich composition helped the crystallization process.[10,19] Figure 5.4 presents the Sr *3d* and Zr 3*d* X-ray photoelectron spectra. There are no obvious chemical shifts or low oxidization state for Sr^{2+} and Zr^{4+}, which indicates that the vacuum annealing does not lead to detectable oxygen vacancies in the SZO films.

Film thickness was confirmed by XRR and calculated by Bragg's law. The sample for X-ray measurement was grown with 80 unit cycles in total on bare Ge and eventually reached to 11.5 nm thickness. The growth rate for SZO on Ge was around 1.4 Å per cycle. The XRD results in Figure 5.5.(a) reveal the (002) peak is located at 43. 83°, which indicates that the out-of-plane lattice constant for SZO is 4.13 Å and implies the film is compressively strained. The lattice constant for cubic SZO is 4.10 Å at room temperature.[54] Since the Ge-Ge distance is 3.992 Å[55–57] at the Ge (001) surface, a heteroepitaxial SZO film on Ge will lead to in-plane compressive strain of -2.6%. Figure 5.5.(b) shows the rocking curve for the for the (002) reflection of the same sample. The full width at half

maximum (FWHM) is 1.4°, which is a comparable crystalline SHO films grown by ALD on Ge (001).[10]

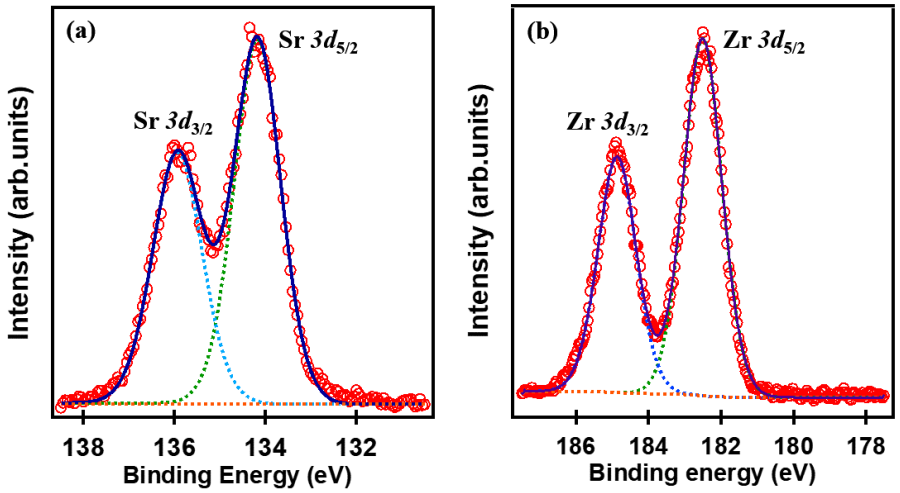

Figure 5.4. X-ray photoelectron spectra for Sr 3*d* (a) and Zr 3*d* (b) in 11.5 nm $SrZrO_3$ film after post deposition annealing at 550 °C.

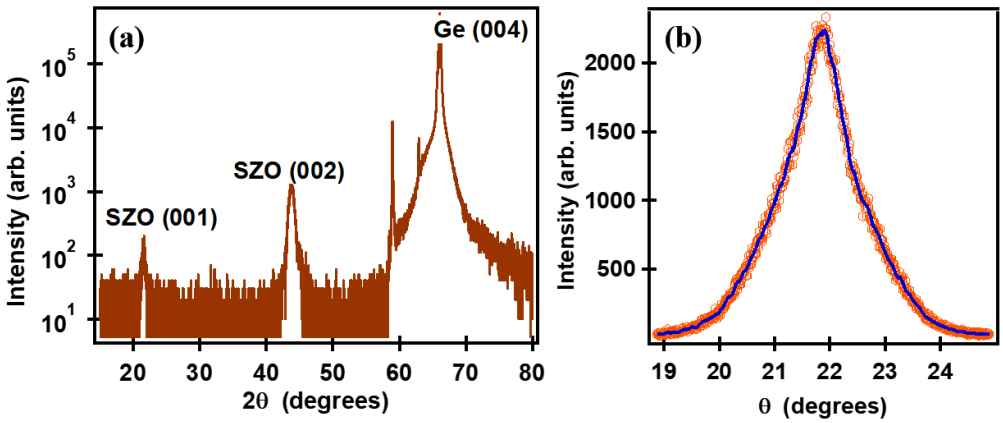

Figure 5.5. X-ray diffraction pattern (a), and rocking curve (b), for 11.5-nm $SrZrO_3$ film grown on bare Ge by ALD. The 3-nm thick seed layer was post-deposition annealed at 620 °C in vacuum and the final film was annealed at 550 °C. The peak of the SZO (002) reflection is at $2\theta = 43.83 \pm 0.5°$ and the rocking curve for the (002) reflection has a full width at half maximum (FWHM) of 1.4°.

5.3.3. ELECTRIC PROPERTIES

Experiments were conducted to compare the effects of different starting surfaces and post-deposition exposure to atomic D on D_{it}. Figure 5.6 presents a schematic of treatment protocols discussed herein. An amorphous SZO film of different thicknesses was used and that had no impact on the crystal quality. Device C used the thinnest first SZO layer to minimize the SZO film through which atomic D would need to diffuse to heal dangling bonds at the Ge-SZO interface. More functional and stable devices are detected on the Zintl template samples than bare Ge samples, which indicates the non-uniform carbon contamination at the interface might be the reason to cause some device failure on bare Ge samples. So to prepare better performance device, the Zintl template is still required. Since a thicker film would require longer gas diffusion time to reach the interface for treatment, the atomic D treatment was applied after obtaining the first crystalline 3nm-SZO layer instead of treating the 15 nm SZO film on Device B. Device A corresponds to an 11.5-nm film grown directly on bare Ge (001) that was treated with UV/ozone. Only Device C was subjected to the oxygen plasma pretreatment protocol.

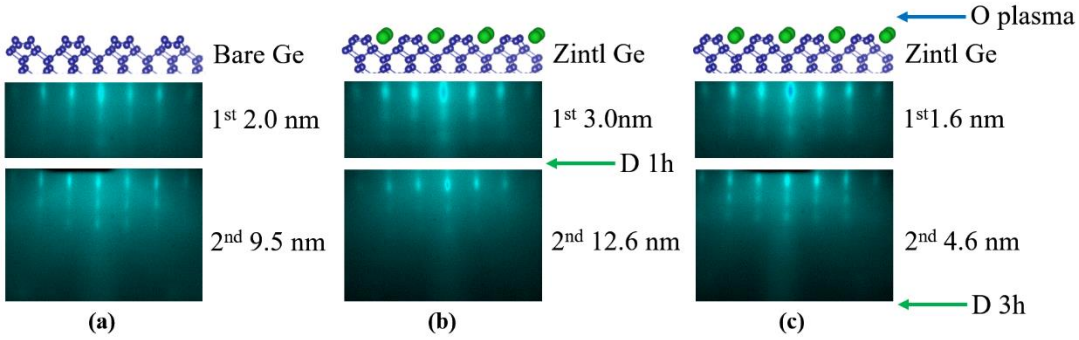

Figure 5.6. Schematic of the treatment procedures for Devices A, B and C. (a) Device A, two-step SZO deposition on bare Ge, (b) Device B, two-step SZO deposition on Zintl-templated Ge with 1 hr atomic deuterium post treatment, and (c) Device C, two-step SZO growth on Zintl-templated Ge with an oxygen plasma pretreatment and 3 hr atomic deuterium post treatment.

For all three devices, both C-V and I-V measurements were performed at room temperature and D_{it} was measured at 250K.[58] Figure 5.7 shows the C-V characteristics for Device C at frequencies from 1kHz to 1000kHz. The capacitance is normalized by the area of top 100 μm×100 μm square Pt electrode. The saturated C_{ox} at accumulation was 3.92 μF/cm^2 with the 1kHz C-V scan, which results in a dielectric constant of 27.6. A more accurate C_{ox} should be determined by C-V scans at low frequency around 20Hz but noisy signals were obtained. A quasi-static method[59] was applied to correct the C_{ox} to estimate the dielectric constant. The final estimation for this device is around 30, which is consistent with the reports in the literature.[22] The same measurement and correction method were applied to Device A and B. Both devices yield *k* of 30. As shown in Figure 5.8, all devices behave very insulating at the applied voltages. The leakage current is normalized by the area of top electrode to get the leakage current density. Table 5.1 lists the leakage current density (*J*) at applied electric field (*E*) of 1 MV/cm along with the corresponding equivalent oxide thickness for the devices. The electrical properties in a previous study on STO/Ge, SHO/Ge and SHTO/Ge heterojunctions are also listed for comparison. The $SrBO_3$ indicates the Sr based perovskite, B indicates the elements of Ti, Zr or Hf in Titanium group.

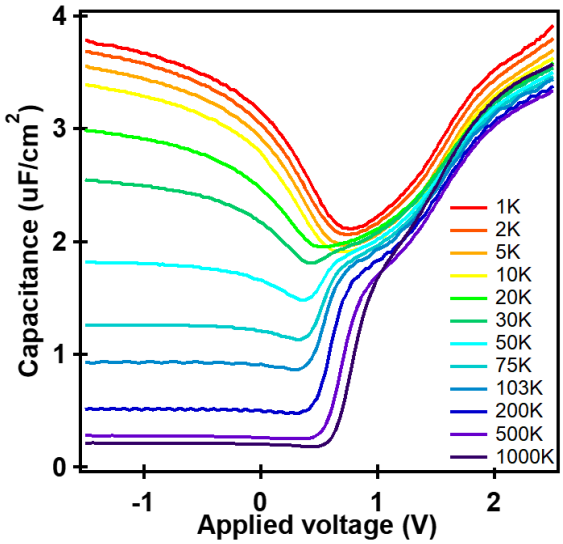

Figure 5.7. Capacitance-voltage (C-V) characteristics of 6.2 nm-SZO on Zintl template (Device C) for frequencies from 1 kHz to 1000kHz. The capacitance is normalized by the area of top 100 μm×100 μm square Pt electrode.

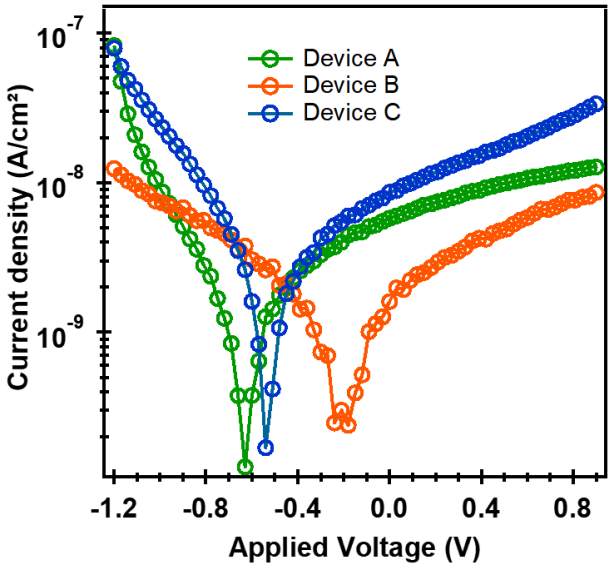

Figure 5.8. Leakage current-voltage (I-V) characteristics of the 11.5 nm-SZO on Ge (Device A), 15.6 nm-SZO on Zintl template (Device B) and 6.2 nm-SZO on Zintl template (Device C). All devices exhibit low leakage current density. The leakage current density is normalized by the area of top 100 μm×100 μm square Pt electrode.

Table 5.1: Electrical properties for $SrBO_3$/Ge heterojunctions

Material		J (A/cm^2)	EOT (nm)	k	E (MV/cm)
$SrZrO_3$	Device A	1.45×10^{-8}	1.5	30	1.0
	Device B	1.52×10^{-8}	2.0		
	Device C	2.14×10^{-8}	0.8		
$SrTiO_3$[19]		~10	0.65	~90	0.7
$SrHfO_3$[10]		6.3×10^{-6}	1.0	17	1.0
$SrHf_{0.55}Ti_{0.45}O_3$[9]		0.1	1.8	30	1.0

SZO has better performance on electrical properties than STO, SHO and SHTO (Hf=0.55). The leakage current of SZO/Ge is about nine orders of magnitude less than STO/Ge, which is consistent with the conduction band offset (CBO) for these heterojunctions. The CBO for STO/Ge, SZO/Ge and SHO/Ge heterojunctions are 0.12, 1.77 and 2.17eV, respectively.[10,19,22] Even though SHO/Ge has a higher CBO than SZO/Ge, the leakage current for SZO/Ge is approximately two order of magnitudes less than SHO/Ge. The main reason may be that SZO is easier to crystalize and obtain better crystallinity than SHO. The annealing temperature for SZO/Ge is about 50 °C less than SHO/Ge. Higher temperature post deposition annealing could cause more oxygen vacancies in SHO films. When comparing the leakage current performance and the EOT with other gate oxides on Ge that re reported in literatures,[20] shows crystalline SZO has a lower leakage current without sacrificing the EOT. This suggests crystalline SZO could be a competitive high-*k* gate oxide material for field-effect transistor device applications.

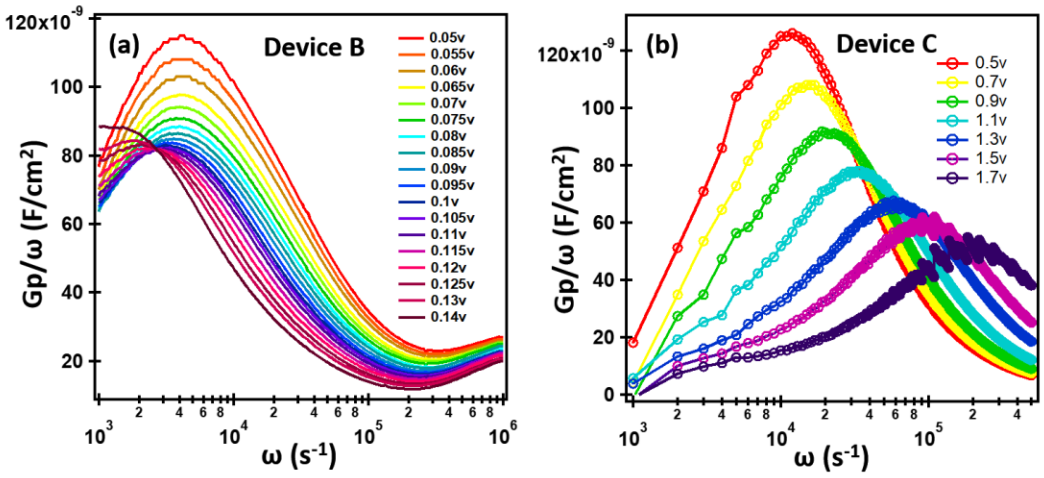

Figure 5.9. The conductance G_P is measured as a function of frequency and plotted as G_P/ω versus ω. (a) The G_P/ω versus ω plot for Device B, (b) The G_P/ω versus ω plot for Device C. G_P/ω is normalized by the area of top 100 μm×100 μm square Pt electrode.

The interface trap density is also an important consideration for high performance field-effect transistor applications. The previous study of crystalline SHO on Ge (001) revealed D_{it} was $4\times10^{13}cm^{-2}eV^{-1}$,[10] which is too high a value for device applications. The D_{it} of SHO/Ge was measured at room temperature and was estimated by the conductance method.[10,20] The conductance model was set up based on Si, which assumes small minority carrier concentration of 1.45×10^{10}. Ge has a much higher minority carrier concentration of 2.4×10^{13}, contributing strong conductance loss in weak inversion. Therefore D_{it} measurements on oxide/Ge heterojunctions should be performed at lower temperature around 250K.[58,60] In conductance method for D_{it} measurement, the conductance G_P is measured as a function of frequency and plotted as G_P/ω versus ω. Figure 5.9 presents the results for Devices B and C in depletion region and weak inversion region. The plot of Device A is not shown here. Based on the conductance method, in the depletion and weak

inversion regions, one takes the minimal peak value among the G_P/ω versus ω curves and substitutes it into the following equation to estimate the D_{it} value.[59]

$$D_{it} \approx \frac{2.5}{q}\left(\frac{\mathrm{Gp}}{\omega}\right)_{max}$$

The estimated D_{it} values for three devices are listed in Figure 5.10. Device A is expected to have the roughest starting surface and carbon contamination at the interface and it has the largest D_{it} value of the three devices. Crystalline SZO in Device A comes closest to crystalline SHO with respect to the starting interface and contamination levels, and SZO has a D_{it} value that is less than the ~4×10^{13}cm^{-2}eV^{-1} for SHO.[10] $D_{it,}$ improved with a Zintl-templated surface and some form of atomic D treatment. The lowest the D_{it} value of 8.56×10^{11}cm^{-2}eV^{-1} was observed when an oxygen plasma was used to generate a flatter Ge (001) surface and lower the the Ge surface steps.[28] The steps could cause the dangling bond at the interface and anti-phase boundary formation within the epitaxial films.[9] The $D_{it,}$ investigation illustrates steps can be taken to improve the electrical properties of crystalline perovskite-germanium interfaces and additional studies may find more optimal treatment conditions.

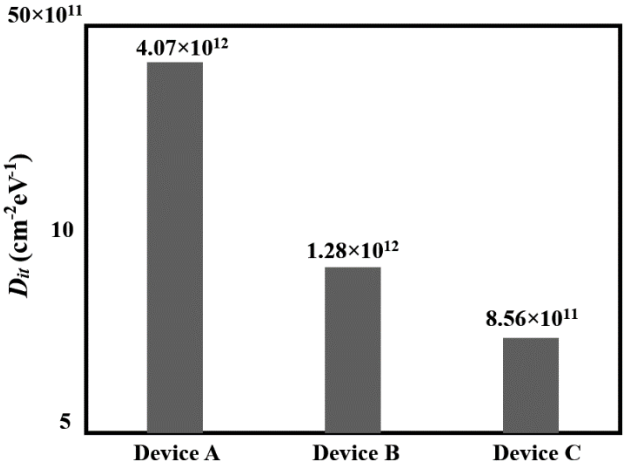

Figure 5.10. D_{it} values for the three devices

5.4. SUMMARY

Heteroepitxial growth of crystalline $SrZrO_3$ (SZO) on Ge (001) by atomic layer deposition is reported in this work. Ge (001) surfaces are pretreated with 0.5 monolayers (ML) of Ba atoms and an amorphous 3-nm SZO layer is grown from strontium bis(triisopropylcyclopentadieynl), tetrakis (dimethylamido) zirconium and water at 225 °C. This 3-nm layer crystallizes at 590 °C and subsequent SZO growth at 225 °C leads to crystalline films that do not require further annealing. The film properties are measured using x-ray photoelectron spectroscopy, x-ray diffraction, transmission electron microscopy and metal-oxide semiconductor capacitor structures. The electrical properties for $SrZrO_3$/Ge heterojunctions are a dielectric constant of 30 and leakage current of 2.14×10^{-8} A/cm^2 at 1 MV/cm with an EOT＝0.8 nm. Ozone plasma pretreatment of Ge (001), Zintl layer formation with 0.5 ML Ba, and atomic deuterium post growth treatment were explored to lower interface traps. The lowest D_{it} was 8.56×10^{11}cm^{-2}eV^{-1}.

5.5. REFERENCES

1 M. D. McDaniel, T. Q. Ngo, S. Hu, A. Posadas, A. A. Demkov, and J. G. Ekerdt, Appl. Phys. Rev. **2**, 041301 (2015).

2 S. R. Singamaneni, J. T. Prater, and J. Narayan, Appl. Phys. Rev. **3**, 031301 (2016).

3 R. A. Mckee, F. J. Walker, and M. F. Chisholm, Phys. Rev. Lett. **81**, 3014 (1998).

4 K. Kukli, M. Ritala, T. Sajavaara, T. Hänninen, and M. Leskelä, Thin Solid Films **500**, 322 (2006).

5 L. Ji, M. D. McDaniel, S. Wang, A. B. Posadas, X. Li, H. Huang, J. C. Lee, A. A. Demkov, A. J. Bard, J. G. Ekerdt, and E. T. Yu, Nat. Nanotechnol. **10**, 84 (2015).

6 Y. Guo, K. Suzuki, K. Nishizawa, T. Miki, and K. Kato, J. Cryst. Growth **284**, 190 (2005).

7 Y. Shichi, S. Tanimoto, T. Goto, K. Kuroiwa, and Y. Tarui, Jpn. J. Appl. Phys. **33**, 5172 (1994).

8 Y. Chu, L.W. Martin, M. B. Holcomb, M. Gajek, S. Han, Q. He, N. Balke, C. Yang, D. Lee, W. Hu, Q. Zhan, P. Yang, A. Fraile-rodríguez, A. Scholl, S.X. Wang, and R. Ramesh, Nat. Mater. Lond. **7**, 478 (2008).

9 S. Hu, M. D. McDaniel, A. Posadas, C. Hu, H. Wu, E. T. Yu, D. J. Smith, A. A. Demkov, and J.G. Ekerdt, MRS Commun. **6**, 125 (2016).

10 M. D. McDaniel, C. Hu, S. Lu, T. Q. Ngo, A. Posadas, A. Jiang, D. J. Smith, E. T. Yu, A. A. Demkov, and J. G. Ekerdt, J. Appl. Phys. **117**, 054101 (2015).

11 M. Okuyama and Y. Hamakawa, Ferroelectrics **63**, 243 (1985).

12 J. H. Ngai, K. Ahmadi-Majlan, J. Moghadam, M. Chrysler, D. Kumah, F. J. Walker, C. H. Ahn, T. Droubay, Y. Du, S. A. Chambers, M. Bowden, X. Shen, and D. Su, J. Mater. Res. **32**, 249 (2017).

13 Z. H. Lim, K. Ahmadi-Majlan, E. D. Grimley, Y. Du, M. Bowden, R. Moghadam, J. M. LeBeau, S. A. Chambers, and J. H. Ngai, J. Appl. Phys. **122**, 084102 (2017).

14 D. A. Muller, T. Sorsch, S. Moccio, F. H. Baumann, K. Evans-Lutterodt, and G. Timp, Nature **399**, 758 (1999).

15 J. Robertson and R. M. Wallace, Mater. Sci. Eng. R Rep. **88**, 1 (2015).

16 S. A. Chambers, Y. Liang, Z. Yu, R. Droopad, and J. Ramdani, J. Vac. Sci. Technol. Vac. Surf. Films **19**, 934 (2001).

17 F. Amy, A. S. Wan, A. Kahn, F. J. Walker, and R. A. McKee, J. Appl. Phys. **96**, 1635 (2004).

18 X. Zhang, A. A. Demkov, H. Li, X. Hu, Y. Wei, and J. Kulik, Phys. Rev. B **68**, 125323 (2003).

19 M. D. McDaniel, T. Q. Ngo, A. Posadas, C. Hu, S. Lu, D. J. Smith, E. T. Yu, A. A. Demkov, and J. G. Ekerdt, Adv. Mater. Interfaces **1**, 1400081 (2014).

20 C. Hu, M.D. McDaniel, A. Jiang, A. Posadas, A. A. Demkov, J. G. Ekerdt, and E. T. Yu, ACS Appl. Mater. Interfaces **8**, 5416 (2016).

21 M. Yang, W. S. Deng, Q. Chen, Y. P. Feng, L. M. Wong, J. W. Chai, J. S. Pan, S. J. Wang, and C. M. Ng, Appl. Surf. Sci. **256**, 4850 (2010).

22 M. Jahangir-Moghadam, K. Ahmadi-Majlan, X. Shen, T. Droubay, M. Bowden, M. Chrysler, D. Su, S. A. Chambers, and J. H. Ngai, Adv. Mater. Interfaces **2**, 1400497 (2015).

23 P. S. Goley and M. K. Hudait, Materials **7**, 2301 (2014).

24 M. Kobayashi, J. Mitard, T. Irisawa, T. Hoffmann, M. Meuris, K. Saraswat, Y. Nishi, and M. Heyns, IEEE Trans. Electron Devices **58**, 384 (2011).

25 R. Pillarisetty, Nature **479**, 324 (2011).

26 D. P. Brunco, B. D. Jaeger, G. Eneman, A. Satta, V. Terzieva, L. Souriau, F. E. Leys, G. Pourtois, M. Houssa, K. Opsomer, G. Nicholas, M. Meuris, and M. Heyns, ECS Trans. **11**, 479 (2007).

27 X.-J. Zhang, G. Xue, A. Agarwal, R. Tsu, M.-A. Hasan, J. E. Greene, and A. Rockett, J. Vac. Sci. Technol. A **11**, 2553 (1993).

28 P. Ponath, A. B. Posadas, R. C. Hatch, and A. A. Demkov, J. Vac. Sci. Technol. B **31**, 031201 (2013).

29 J. Oh and J.C. Campbell, J. Electron. Mater. **33**, 364 (2004).

30 S. Baldovino, A. Molle, and M. Fanciulli, Appl. Phys. Lett. **93**, 242105 (2008).

31 S. Mohsenifar, M.H. Shahrokhabadi, S. Mohsenifar, and M. H. Shahrokhabadi, Microelectron. Solid State Electron. **4**, 12 (2015).

32 I. Oh, M.-K. Kim, J. Lee, C.-W. Lee, C. Lansalot-Matras, W. Noh, J. Park, A. Noori, D. Thompson, S. Chu, W.J. Maeng, and H. Kim, Appl. Surf. Sci. **287**, 349 (2013).

33 S. Swaminathan, M. Shandalov, Y. Oshima, and P. C. McIntyre, Appl. Phys. Lett. **96**, 082904 (2010).

34 R. Xie, T. H. Phung, W. He, M. Yu, and C. Zhu, IEEE Trans. Electron Devices **56**, 1330 (2009).

35 M. Caymax, M. Houssa, G. Pourtois, F. Bellenger, K. Martens, A. Delabie, and S. Van Elshocht, Appl. Surf. Sci. **254**, 6094 (2008).

36 K. Kita, T. Takahashi, H. Nomura, S. Suzuki, T. Nishimura, and A. Toriumi, Appl. Surf. Sci. **254**, 6100 (2008).

37 C. H. Lee, C. Lu, T. Tabata, W. F. Zhang, T. Nishimura, K. Nagashio, and A. Toriumi, Electron Devices Meet. IEDM 2013 IEEE Int. p. 2.5.1-2.5.4 (2013).

38 R. Zhang, P. C. Huang, N. Taoka, M. Takenaka, and S. Takagi, Symp. VLSI Technol. VLSIT, pp. 161–162 (2012).

39 C. H. Lee, C. Lu, T. Tabata, T. Nishimura, K. Nagashio, and A. Toriumi, Symp. VLSI Technol. VLSIT, pp. T28–T29 (2013).

40 H. Matsubara, T. Sasada, M. Takenaka, and S. Takagi, Appl. Phys. Lett. **93**, 032104 (2008).

41 A. Delabie, F. Bellenger, M. Houssa, T. Conard, S. Van Elshocht, M. Caymax, M. Heyns, and M. Meuris, Appl. Phys. Lett. **91**, 082904 (2007).

42 R. Zhang, J.C. Lin, X. Yu, M. Takenaka, and S. Takagi, Symp. VLSI Technol. VLSIT, pp. T26–T27 (2013).

43 P. Avouris, R. E. Walkup, A. R. Rossi, T.-C. Shen, G. C. Abeln, J. R. Tucker, and J. W. Lyding, Chem. Phys. Lett. **257**, 148 (1996).

44 M. D. McDaniel, A. Posadas, T. Wang, A. A. Demkov, and J. G. Ekerdt, Thin Solid Films **520**, 6525 (2012).

45 S. Hu, E. L. Lin, A. K. Hamze, A. Posadas, H-W. Wu, D. J. Smith, A. A. Demkov, and J. G. Ekerdt, J. Chem. Phys. **146**, 052817 (2016).

46 U. Bischler and E. Bertel, J. Vac. Sci. Technol. Vac. Surf. Films **11**, 458 (1993).

47 J. M. McCrate and J. G. Ekerdt, Chem. Mater. **26**, 2166 (2014).

48 C. D. Wagner, W. M. Riggs, L. E. Davis, and J. F. Moulder, Perkin-Elmer Phys. Electron. Div. (1979).

49 P. Ponath, K. Fredrickson, A. B. Posadas, Y. Ren, X. Wu, R. K. Vasudevan, M. Baris Okatan, S. Jesse, T. Aoki, M. R. McCartney, D. J. Smith, S. V. Kalinin, K. Lai, and A. A. Demkov, Nat. Commun. **6**, 6067 (2015).

50 H. Wu, T. Aoki, A. B. Posadas, A. A. Demkov, and D. J. Smith, Appl. Phys. Lett. **108**, 091605 (2016).

51 S. Hu, A. B. Posadas, A. A. Demkov and J. G. Ekerdt, "The function of Zintl layer for atomic layer deposition on Ge (001)" in preparation, (2017)

52 M. D. McDaniel, A. Posadas, T. Q. Ngo, A. Dhamdhere, D. J. Smith, A. A. Demkov, and J. G. Ekerdt, J. Vac. Sci. Technol. A **31**, 01A136 (2013).

53 K. D. Fredrickson, P. Ponath, A. B. Posadas, M. R. McCartney, T. Aoki, D. J. Smith, and A. A. Demkov, Appl. Phys. Lett. **104**, 242908 (2014).

54 D. de Ligny and P. Richet, Phys. Rev. B **53**, 3013 (1996).

55 A. S. Cooper, Acta Cryst **Vol: 15**, (1962).

56 M. E. Straumanis and E. Z. Aka, J. Appl. Phys. **23**, 330 (1952).

57 Y. Okada and Y. Tokumaru, J. Appl. Phys. **56**, 314 (1984).

58 K. Martens, C. O. Chui, G. Brammertz, B. D. Jaeger, D. Kuzum, M. Meuris, M. Heyns, T. Krishnamohan, K. Saraswat, H.E. Maes, and G. Groeseneken, IEEE Trans. Electron Devices **55**, 547 (2008).

59 D. K. Schroder, *Semiconductor Material and Device Characterization* (John Wiley & Sons, 2006).

60 K. Saraswat, D. Kim, T. Krishnamohan, D. Kuzum, A. K. Okyay, A. Pethe, and H.-Y. Yu, ECS Trans. **16**, 3 (2008).

Chapter 6: Research Summary

6.1. SUMMARY AND CONCLUSIONS

This work reports the growth of crystalline $SrHf_xTi_{1-x}O_3$ (SHTO) films on Ge (001) substrates by atomic layer deposition. Samples were prepared with different Hf content x to explore if strain, from tensile ($x = 0$) to compressive ($x = 1$), affected film crystallization temperature and how composition affected properties. Amorphous films grew at 225 °C and crystallized into epitaxial layers at annealing temperatures that varied monotonically with composition from ~530 °C ($x = 0$) to ~660 °C ($x = 1$). Transmission electron microscopy revealed abrupt interfaces. Electrical measurements revealed 0.1 A/cm^2 leakage current at 1 MV/cm for $x = 0.55$.

Using in situ X-ray photoelectron spectroscopy, reflection high-energy electron diffraction and density functional theory, we analyzed the surface core level shifts and surface structure during the initial growth of ABO_3 perovskites on Ge (001) by atomic layer deposition, where A = Ba, Sr and B = Ti, Hf, Zr. We find that the initial dosing of the barium- or strontium- bis(triisopropylcyclopentadienyl) precursors on a clean Ge surface produces a surface phase that has the same chemical and structural properties as the 0.5-monolayer Ba Zintl layer formed when depositing Ba by molecular beam epitaxy. Similar binding energy shifts are found for Ba, Sr and Ge when using either chemical or elemental metal sources. The observed germanium surface core level shifts are consistent with the flattening of the initially-tilted Ge surface dimers using both molecular and atomic metal sources. Similar binding energy shifts and changes in dimer tilting with alkaline earth metal adsorption are found with density functional theory calculations. High angle angular dark field scanning transmission microscopy images of $BaTiO_3$, $SrZrO_3$, $SrHfO_3$ and

$SrHf_{0.55}Ti_{0.45}O_3$ reveal the location of the Ba (or Sr) atomic columns between the Ge dimers. The results imply that the organic ligands dissociate from the precursor after precursor adsorption on the Ge surface, producing the same Zintl template critical for perovskite growth on Group IV semiconductors during molecular beam epitaxy.

Heteroepitxial growth of crystalline $SrZrO_3$ (SZO) on Ge (001) by atomic layer deposition is reported. Ge (001) surfaces are pretreated with 0.5 monolayers (ML) of Ba atoms and an amorphous 3-nm SZO layer is grown from strontium bis(triisopropylcyclopentadieynl), tetrakis (dimethylamido) zirconium and water at 225 °C. This 3-nm layer crystallizes at 590 °C and subsequent SZO growth at 225 °C leads to crystalline films that do not require further annealing. The film properties are measured using x-ray photoelectron spectroscopy, x-ray diffraction, transmission electron microscopy and metal-oxide semiconductor capacitor structures. The electrical properties for $SrZrO_3$/Ge heterojunctions are a dielectric constant of 30 and leakage current of 2.14×10^{-8} A/cm^2 at 1 MV/cm with an EOT＝0.8 nm. Oxygen plasma pretreatment of Ge (001), Zintl layer formation with 0.5 ML Ba, and atomic deuterium post growth treatment were explored to lower interface traps. The lowest D_{it} was 8.56×10^{11}cm^{-2}eV^{-1}.

6.2. RECOMMENDATIONS FOR FUTURE WORK

This research implied that $SrZrO_3$ has the best electrical properties in $SrBO_3$ perovskite for high-*k* gate oxides applications in transistors. An efficient treatment strategy, which combines Zinlt template preparation, oxygen plasma pre-treatment and post atomic deuterium treatment, has been employed here to reduce the D_{it} value. The lowest D_{it} value (8.56×10^{11}cm^{-2}eV^{-1}) has met the requirement for device fabrication.[1] Since high quality interfaces can result in higher channel mobility and driving current I_{on}. Tagaki has reported

the high effective electron mobility of 488 cm^2/Vs for $Al_2O_3/GeO_x/Ge$ nMOSFETs with atomic deuterium PDA at 400 °C.[2] So the performance of MOSFET device based on the materials of this dissertation could be very promising. The MOSFET fabrication process could follow the procedure shown in Figure 6.1.[3] Following the same process and replacing the step 3) with the $SrZrO_3$ deposition and treatment process as discussed in Chapter 5 can easily obtain the MOSFET for further electrical measurements.

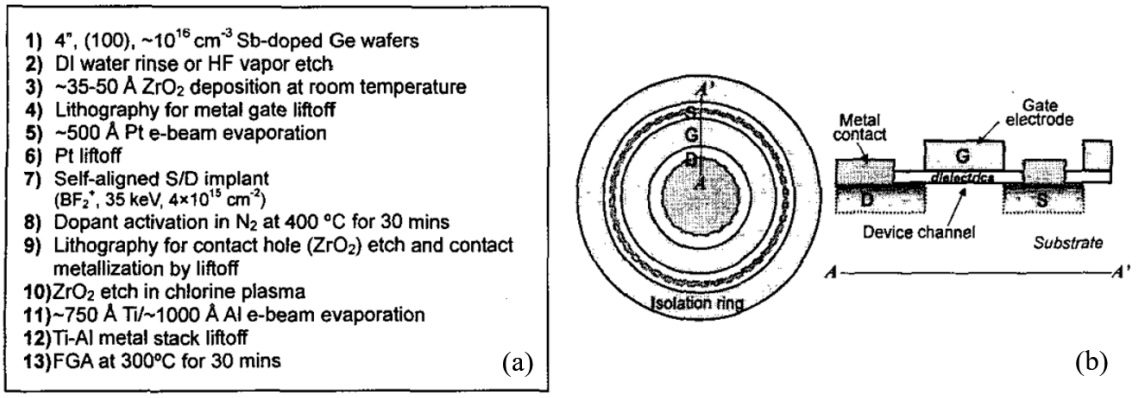

Figure 6.1. (a)The procedure for nMOSFET fabrication process based on ZrO_2/Ge gate stack, (b) the top-view of the ring MOSFET structure (lefl) and the cross-sectional side view of AA' (right). Taken from "A Sub-400 °C Germanium MOSFET Technology with High-*k* Dielectric and Metal Gate." *Electron Devices Meeting (IEDM*), International. IEEE, 437-440, (2002).[3]

Though the $SrZrO_3$ study obtained the desired electrical properties and acceptable D_{it} value. The influence from the relatively high compressive strain, which is around -2.6% of $SrZrO_3$ on Ge, has not been estimated. High strain could cause the bond length changes at the interface and possibly lead to dangling bonds. The work in Chapter 3 presents the strain of $SrHf_xTi_{1-x}O_3$ and it can be adjusted by the Hf content *x.* But since the Ti content will eliminate the conduction band offset (CBO) between $SrHf_xTi_{1-x}O_3$ and Ge and can lead to higher leakage current, so the influence of strain on D_{it} still hasn't been explored

yet. There is another perovskite $CaHfO_3$ gives an opportunity here. Since $CaHfO_3$ has a simple cubic perovskite lattice parameter a_p=3.991 Å,[4] with the 3.992 Å Ge-Ge distance on (001) surface, the pseudocubic unit cell of $CaHfO_3$ can perfectly match with Ge (001) substrate.

The large band gap of $CaHfO_3$=6.4 eV also enables the $CaHfO_3$/Ge heterojunction to be insulating enough for the D_{it} measurement. In addition, the suitable precursors of Ca and Hf are available as bis(tri-isopropylcyclopentadienyl) calcium 1,2-dimethoxyethane and hafnium formamidinate [$Hf(fmd)_4$] (Hf-FAMD), respectively for ALD deposition. Also the deposition of $CaHfO_3$ on Ge by ALD has never been reported before.

Last but not the least, this research offers a very insulating materials $SrZrO_3$ on Ge (001) and a good strategy to achieve lower interface trap density. We can further apply this work for ferroelectric switching study of $BaTiO_3$ by building up $BaTiO_3$/ $SrZrO_3$/Ge.

6.3. REFERENCES

1 P. S. Goley and M. K. Hudait, Materials **7**, 2301 (2014).

2 R. Zhang, J. C. Lin, X. Yu, M. Takenaka, and S. Takagi, Symp. VLSI Technol, pp. T26–T27 (2013).

3 C. O. Chui, H. Kim, D. Chi, B. B. Triplett, P. C. McIntyre, and K. C. Saraswat, Dig. Int. Electron Devices Meet, pp. 437–440 (2002).

4 K. Shibuya, T. Ohnishi, M. Lippmaa, M. Kawasaki, and H. Koinuma, Appl. Phys. Lett. **84**, 2142 (2004).

Appendix

First-Author Publications

[1] S. Hu, A. B. Posadas, A. A. Demkov and J. G. Ekerdt, "The function of Zintl layer for atomic layer deposition on Ge (001)" **In preparation**.

[2] S. Hu, L. Ji, P-Y Chen, H-L Chang, A. Posadas, H-W Wu, E. T. Yu, D. J. Smith, A. A Demkov, and J. G. Ekerdt, "Crystalline $SrZrO_3$ deposition on Ge (001) by atomic layer deposition for high-k dielectric application" **In preparation.**

[3] S. Hu, E. L. Lin, A. K. Hamze, A. Posadas, H-W Wu, D. J. Smith, A. A Demkov, and J. G. Ekerdt, "Zintl layer formation during perovskite atomic layer deposition on Ge (001)" J. Chem. Phys. **146**, 052817 (2016).

[4] S. Hu, M. D. McDaniel, A. Posadas, C. Hu, H. Wu, E. T. Yu, D. J. Smith, A. A. Demkov, and J.G. Ekerdt, "Monolithic Integration of Perovskites on Ge(001) by Atomic Layer Deposition: A Case Study with $SrHf_xTi_{1-x}O_3$" MRS Commun. **6**, 125 (2016).

Co-Author Publications

[1] F. Cheng, A. D. Johnson, Y. Tsai, P-H Su, S. Hu, J. G. Ekerdt, and C-K. Shih, "Enhanced Photoluminescence of Monolayer WS_2 on Ag Films and Nanowire−WS_2−Film Hybrids" ACS Photonics, **4**, 1421 (2017).

[2] E. L. Lin, S. Hu, and J. G. Ekerdt, "Monolithic integration of metal-ferroelectric-semiconductor heterostructure using atomic layer deposition" In Proc. of SPIE **10105**, 1010519 (2017).

[3] E. L Lin, B. I. Edmondson, S. Hu, and J. G. Ekerdt, "Epitaxial Growth of Perovskite Strontium Titanate on Germanium via Atomic Layer Deposition" JoVE (Journal of Visualized Experiments), **113**, e54268-e54268 (2016).

[4] M. D. McDaniel, T. Q. Ngo, S. Hu, A. Posadas, A. A. Demkov, and J. G. Ekerdt, "Atomic layer deposition of perovskite oxides and their epitaxial integration with Si, Ge, and other semiconductors" Appl. Phys. Rev. **2**, 041301 (2015).

Technical Presentation

[1] (Presentation) *Zintl template formation and function during atomic layer deposition growth of crystalline perovskites on Ge (001)*, AVS 64th International Symposium & Exhibition 2017, Tampa, Florida, October 29-November 3, 2017.

[2] (Poster) *Structural and Electrical Characterization of Epitaxial Sr(Hf,Ti)O_3 grown on Ge (001) by Atomic Layer Deposition*, The 15th International Conference on Atomic Layer Deposition, Portland, Oregon June 28 – July 1, 2015.

Bibliography

1 P.S. Goley and M.K. Hudait, Materials **7**, 2301 (2014).

2 D.A. Muller, T. Sorsch, S. Moccio, F.H. Baumann, K. Evans-Lutterodt, and G. Timp, Nature **399**, 758 (1999).

3 R. Chau, S. Datta, M. Doczy, J. Kavalieros, and M. Metz, in Ext. Abstr. Int. Workshop Gate Insul. IEEE Cat No03EX765, pp. 124–126 (2003).

4 M. Kobayashi, J. Mitard, T. Irisawa, T. Hoffmann, M. Meuris, K. Saraswat, Y. Nishi, and M. Heyns, IEEE Trans. Electron Devices **58**, 384 (2011).

5 International Roadmap for Semiconductors (2012 Edition).

6 D.P. Brunco, B.D. Jaeger, G. Eneman, A. Satta, V. Terzieva, L. Souriau, F.E. Leys, G. Pourtois, M. Houssa, K. Opsomer, G. Nicholas, M. Meuris, and M. Heyns, ECS Trans. **11**, 479 (2007).

7 R. Pillarisetty, Nature **479**, 324 (2011).

8 E. Simoen, J. Mitard, G. Hellings, G. Eneman, B. De Jaeger, L. Witters, B. Vincent, R. Loo, A. Delabie, S. Sioncke, M. Caymax, and C. Claeys, Mater. Sci. Semicond. Process. **15**, 588 (2012).

9 X.-J. Zhang, G. Xue, A. Agarwal, R. Tsu, M.-A. Hasan, J.E. Greene, and A. Rockett, J. Vac. Sci. Technol. A **11**, 2553 (1993).

10 P. Ponath, A.B. Posadas, R.C. Hatch, and A.A. Demkov, J. Vac. Sci. Technol. B **31**, 031201 (2013).

11 J. Oh and J.C. Campbell, J. Electron. Mater. **33**, 364 (2004).

12 S. Mohsenifar, M.H. Shahrokhabadi, S. Mohsenifar, and M.H. Shahrokhabadi, Microelectron. Solid State Electron. **4**, 12 (2015).

13 S. Baldovino, A. Molle, and M. Fanciulli, Appl. Phys. Lett. **93**, 242105 (2008).

14 S. Hu, M.D. McDaniel, A. Posadas, C. Hu, H. Wu, E.T. Yu, D.J. Smith, A.A. Demkov, and J.G. Ekerdt, MRS Commun. **6**, 125 (2016).

15 A.I. Kingon, J.-P. Maria, and S.K. Streiffer, Nature **406**, 1032 (2000).

16 S.M. George, Chem. Rev. **110**, 111 (2010).

17 J. Provine and M. Rincon, NNIN ALD Road Show (2012).

18 M. Leskelä and M. Ritala, Thin Solid Films **409**, 138 (2002).

19 M.D. McDaniel, T.Q. Ngo, A. Posadas, C. Hu, S. Lu, D.J. Smith, E.T. Yu, A.A. Demkov, and J.G. Ekerdt, Adv. Mater. Interfaces **1**, 1400081 (2014).

20 M.D. McDaniel, C. Hu, S. Lu, T.Q. Ngo, A. Posadas, A. Jiang, D.J. Smith, E.T. Yu, A.A. Demkov, and J.G. Ekerdt, J. Appl. Phys. **117**, 054101 (2015).

21 K.D. Fredrickson, P. Ponath, A.B. Posadas, M.R. McCartney, T. Aoki, D.J. Smith, and A.A. Demkov, Appl. Phys. Lett. **104**, 242908 (2014).

22 A.A. Demkov and A.B. Posadas, Integration of Functional Oxides with Semiconductors (Springer, 2014).

23 N. Setter, D. Damjanovic, L. Eng, G. Fox, S. Gevorgian, S. Hong, A. Kingon, H. Kohlstedt, N.Y. Park, G.B. Stephenson, I. Stolitchnov, A.K. Taganstev, D.V. Taylor, T. Yamada, and S. Streiffer, J. Appl. Phys. **100**, 051606 (2006).

24 M. Jahangir-Moghadam, K. Ahmadi-Majlan, X. Shen, T. Droubay, M. Bowden, M. Chrysler, D. Su, S.A. Chambers, and J.H. Ngai, Adv. Mater. Interfaces **2**, 1400497 (2015).

25 R.A. McKee, F.J. Walker, and M.F. Chisholm, Science **293**, 468 (2001).

26 J.W. Reiner, A.M. Kolpak, Y. Segal, K.F. Garrity, S. Ismail-Beigi, C.H. Ahn, and F.J. Walker, Adv. Mater. **22**, 2919 (2010).

27 Z. Yu, Y. Liang, C. Overgaard, X. Hu, J. Curless, H. Li, Y. Wei, B. Craigo, D. Jordan, R. Droopad, J. Finder, K. Eisenbeiser, D. Marshall, K. Moore, J. Kulik, and P. Fejes, Thin Solid Films **462–463**, 51 (2004).

28 R. Droopad, Z. Yu, H. Li, Y. Liang, C. Overgaard, A. Demkov, X. Zhang, K. Moore, K. Eisenbeiser, M. Hu, J. Curless, and J. Finder, J. Cryst. Growth **251**, 638 (2003).

29 M. Sousa, C. Rossel, C. Marchiori, H. Siegwart, D. Caimi, J.-P. Locquet, D.J. Webb, R. Germann, J. Fompeyrine, K. Babich, J.W. Seo, and C. Dieker, J. Appl. Phys. **102**, 104103 (2007).

30 J.-G. Cheng, J.-S. Zhou, J.B. Goodenough, and C.-Q. Jin, Phys. Rev. B **85**, 184430 (2012).

31 G.H. Jonker and J.H. Van Santen, Physica **19**, 120 (1953).

32 C.H. Ahn, K.M. Rabe, and J.-M. Triscone, Science **303**, 488 (2004).

33 N. Nuraje and K. Su, Nanoscale **5**, 8752 (2013).

34 G. Catalan and J.F. Scott, Adv. Mater. **21**, 2463 (2009).

35 S. Dong and J.-M. Liu, Mod. Phys. Lett. B **26**, 1230004 (2012).

36 J.G. Bednorz and K.A. Müller, Rev. Mod. Phys. **60**, 585 (1988).

37 M.D. McDaniel, T.Q. Ngo, S. Hu, A. Posadas, A.A. Demkov, and J.G. Ekerdt, Appl. Phys. Rev. **2**, 041301 (2015).

38 R.A. Mckee, F.J. Walker, and M.F. Chisholm, Phys. Rev. Lett. **81**, 3014 (1998).

39 K. Kukli, M. Ritala, T. Sajavaara, T. Hänninen, and M. Leskelä, Thin Solid Films **500**, 322 (2006).

40 L. Ji, M.D. McDaniel, S. Wang, A.B. Posadas, X. Li, H. Huang, J.C. Lee, A.A. Demkov, A.J. Bard, J.G. Ekerdt, and E.T. Yu, Nat. Nanotechnol. **10**, 84 (2015).

41 Y. Guo, K. Suzuki, K. Nishizawa, T. Miki, and K. Kato, J. Cryst. Growth **284**, 190 (2005).

42 Y. Shichi, S. Tanimoto, T. Goto, K. Kuroiwa, and Y. Tarui, Jpn. J. Appl. Phys. **33**, 5172 (1994).

43 Y. Chu, L.W. Martin, M.B. Holcomb, M. Gajek, S. Han, Q. He, N. Balke, C. Yang, D. Lee, W. Hu, Q. Zhan, P. Yang, A. Fraile-rodríguez, A. Scholl, S.X. Wang, and R. Ramesh, Nat. Mater. Lond. **7**, 478 (2008).

44 M. Okuyama and Y. Hamakawa, Ferroelectrics **63**, 243 (1985).

45 J.W. Reiner, A. Posadas, M. Wang, M. Sidorov, Z. Krivokapic, F.J. Walker, T.P. Ma, and C.H. Ahn, J. Appl. Phys. **105**, 124501 (2009).

46 A.A. Demkov, A.B. Posadas, H. Seo, M. Choi, K.J. Kormondy, P. Ponath, R.C. Hatch, M.D. McDaniel, T.Q. Ngo, and J.G. Ekerdt, ECS Trans. **54**, 255 (2013).

47 M.P. Warusawithana, C. Cen, C.R. Sleasman, J.C. Woicik, Y. Li, L.F. Kourkoutis, J.A. Klug, H. Li, P. Ryan, L.-P. Wang, M. Bedzyk, D.A. Muller, L.-Q. Chen, J. Levy, and D.G. Schlom, Science **324**, 367 (2009).

48 S.-H. Baek and C.-B. Eom, Acta Mater. **61**, 2734 (2013).

49 V. Vaithyanathan, J. Lettieri, W. Tian, A. Sharan, A. Vasudevarao, Y.L. Li, A. Kochhar, H. Ma, J. Levy, P. Zschack, J.C. Woicik, L.Q. Chen, V. Gopalan, and D.G. Schlom, J. Appl. Phys. **100**, 024108 (2006).

50 Y. Liang, J. Kulik, T.C. Eschrich, R. Droopad, Z. Yu, and P. Maniar, Appl. Phys. Lett. **85**, 1217 (2004).

51 J. Robertson and R.M. Wallace, Mater. Sci. Eng. R Rep. **88**, 1 (2015).

52 A.S. Cooper, Acta Cryst Vol: 15, (1962).

53 M.E. Straumanis and E.Z. Aka, J. Appl. Phys. **23**, 330 (1952).

54 Y. Okada and Y. Tokumaru, J. Appl. Phys. **56**, 314 (1984).

55 M. Yang, W.S. Deng, Q. Chen, Y.P. Feng, L.M. Wong, J.W. Chai, J.S. Pan, S.J. Wang, and C.M. Ng, Appl. Surf. Sci. **256**, 4850 (2010).

56 Z.H. Lim, K. Ahmadi-Majlan, E.D. Grimley, Y. Du, M. Bowden, R. Moghadam, J.M. LeBeau, S.A. Chambers, and J.H. Ngai, J. Appl. Phys. **122**, 084102 (2017).

57 C. Hu, M.D. McDaniel, A. Jiang, A. Posadas, A.A. Demkov, J.G. Ekerdt, and E.T. Yu, ACS Appl. Mater. Interfaces **8**, 5416 (2016).

58 I. Oh, M.-K. Kim, J. Lee, C.-W. Lee, C. Lansalot-Matras, W. Noh, J. Park, A. Noori, D. Thompson, S. Chu, W.J. Maeng, and H. Kim, Appl. Surf. Sci. **287**, 349 (2013).

59 S. Swaminathan, M. Shandalov, Y. Oshima, and P.C. McIntyre, Appl. Phys. Lett. **96**, 082904 (2010).

60 R. Xie, T.H. Phung, W. He, M. Yu, and C. Zhu, IEEE Trans. Electron Devices **56**, 1330 (2009).

61 M. Caymax, M. Houssa, G. Pourtois, F. Bellenger, K. Martens, A. Delabie, and S. Van Elshocht, Appl. Surf. Sci. **254**, 6094 (2008).

62 K. Kita, T. Takahashi, H. Nomura, S. Suzuki, T. Nishimura, and A. Toriumi, Appl. Surf. Sci. **254**, 6100 (2008).

63 C.H. Lee, C. Lu, T. Tabata, W.F. Zhang, T. Nishimura, K. Nagashio, and A. Toriumi, in Electron Devices Meet. IEDM 2013 IEEE Int. p. 2.5.1-2.5.4 (2013).

64 R. Zhang, P.C. Huang, N. Taoka, M. Takenaka, and S. Takagi, in 2012 Symp. VLSI Technol. VLSIT, pp. 161–162 (2012).

65 C.H. Lee, C. Lu, T. Tabata, T. Nishimura, K. Nagashio, and A. Toriumi, in 2013 Symp. VLSI Technol. VLSIT, pp. T28–T29 (2013).

66 H. Matsubara, T. Sasada, M. Takenaka, and S. Takagi, Appl. Phys. Lett. **93**, 032104 (2008).

67 A. Delabie, F. Bellenger, M. Houssa, T. Conard, S. Van Elshocht, M. Caymax, M. Heyns, and M. Meuris, Appl. Phys. Lett. **91**, 082904 (2007).

68 R. Zhang, J.C. Lin, X. Yu, M. Takenaka, and S. Takagi, in 2013 Symp. VLSI Technol., pp. T26–T27 (2013).

69 P. Avouris, R.E. Walkup, A.R. Rossi, T.-C. Shen, G.C. Abeln, J.R. Tucker, and J.W. Lyding, Chem. Phys. Lett. **257**, 148 (1996).

70 M.D. McDaniel, A. Posadas, T. Wang, A.A. Demkov, and J.G. Ekerdt, Thin Solid Films **520**, 6525 (2012).

71 U. Bischler and E. Bertel, J. Vac. Sci. Technol. Vac. Surf. Films **11**, 458 (1993).

72 J.M. McCrate and J.G. Ekerdt, Chem. Mater. **26**, 2166 (2014).

73 M. Choi, A. Posadas, R. Dargis, C.-K. Shih, A.A. Demkov, D.H. Triyoso, N.D. Theodore, C. Dubourdieu, J. Bruley, and J. Jordan-Sweet, J. Appl. Phys. **111**, 064112 (2012).

74 T.Q. Ngo, A.B. Posadas, M.D. McDaniel, C. Hu, J. Bruley, E.T. Yu, A.A. Demkov, and J.G. Ekerdt, Appl. Phys. Lett. **104**, 082910 (2014).

75 P.W. Loscutoff and S.F. Bent, Annu. Rev. Phys. Chem. **57**, 467 (2006).

76 Y. Kamata, Mater. Today **11**, 30 (2008).

77 G.D. Wilk, R.M. Wallace, and J.M. Anthony, J. Appl. Phys. **89**, 5243 (2001).

78 C.O. Chui, S. Ramanathan, B.B. Triplett, P.C. McIntyre, and K.C. Saraswat, IEEE Electron Device Lett. **23**, 473 (2002).

79 Y. Kamata, K. Ikeda, Y. Kamimuta, and T. Tezuka, in 2010 Symp. VLSI Technol. VLSIT, pp. 211–212 (2010).

80 A. Rollett, F.J. Humphreys, G.S. Rohrer, and M. Hatherly, Recrystallization and Related Annealing Phenomena (Elsevier, 2004).

81 R.A. McKee, F.J. Walker, and M.F. Chisholm, Phys. Rev. Lett. **81**, 3014 (1998).

82 L. Bjaalie, B. Himmetoglu, L. Weston, A. Janotti, and C.G.V. de Walle, New J. Phys. **16**, 025005 (2014).

83 S.A. Chambers, Y. Liang, Z. Yu, R. Droopad, and J. Ramdani, J. Vac. Sci. Technol. Vac. Surf. Films **19**, 934 (2001).

84 F. Amy, A.S. Wan, A. Kahn, F.J. Walker, and R.A. McKee, J. Appl. Phys. **96**, 1635 (2004).

85 X. Zhang, A.A. Demkov, H. Li, X. Hu, Y. Wei, and J. Kulik, Phys. Rev. B **68**, 125323 (2003).

86 C.D. Wagner, W.M. Riggs, L.E. Davis, and J.F. Moulder, Perkin-Elmer Phys. Electron. Div. (1979).

87 D. de Ligny and P. Richet, Phys. Rev. B **53**, 3013 (1996).

88 H.P. Singh, Acta Crystallogr. Sect. A **24**, 469 (1968).

89 S. Yamanaka, T. Maekawa, H. Muta, T. Matsuda, S. Kobayashi, and K. Kurosaki, J. Solid State Chem. **177**, 3484 (2004).

90 A. Meldrum, L.A. Boatner, W.J. Weber, and R.C. Ewing, J. Nucl. Mater. **300**, 242 (2002).

91 C.M. Brooks, L.F. Kourkoutis, T. Heeg, J. Schubert, D.A. Muller, and D.G. Schlom, Appl. Phys. Lett. **94**, 162905 (2009).

92 H. Ledbetter, M. Lei, and S. Kim, Phase Transit. **23**, 61 (1990).

93 J.F. Moulder, W.F. Stickle, P.E. Sobol, and K.D. Bomben, Perkin-Elmer Phys. Electron. Div. (1993).

94 M.P. Seah and W.A. Dench, Surf. Interface Anal. **2** (1979).

95 X. Jiang, R.Q. Zhang, G. Yu, and S.T. Lee, Phys. Rev. B **58**, 15351 (1998).

96 C.M. Foster, Z. Li, M. Buckett, D. Miller, P.M. Baldo, L.E. Rehn, G.R. Bai, D. Guo, H. You, and K.L. Merkle, J. Appl. Phys. **78**, 2607 (1995).

97 H. Wu, T. Aoki, A.B. Posadas, A.A. Demkov, and D.J. Smith, Appl. Phys. Lett. **108**, 091605 (2016).

98 A.A. Demkov and Z. Xiaodong, J. Appl. Phys. **103**, (2008).

99 H. Seo, M. Choi, A.B. Posadas, R.C. Hatch, and A.A. Demkov, J. Vac. Sci. Technol. B **31**, 04D107 (2013).

100 J. Wang, J.A. Hallmark, D.S. Marshall, W.J. Ooms, P. Ordejón, J. Junquera, D. Sánchez-Portal, E. Artacho, and J.M. Soler, Phys. Rev. B **60**, 4968 (1999).

101 M. Choi, A.B. Posadas, H. Seo, R.C. Hatch, and A.A. Demkov, Appl. Phys. Lett. **102**, 031604 (2013).

102 X. Yao, X. Hu, D. Sarid, Z. Yu, J. Wang, D.S. Marshall, R. Droopad, J.K. Abrokwah, J.A. Hallmark, and W.J. Ooms, Phys. Rev. B **59**, 5115 (1999).

103 X. Hu, X. Yao, C.A. Peterson, D. Sarid, Z. Yu, J. Wang, D.S. Marshall, J.A. Curless, J. Ramdani, R. Droopad, J.A. Hallmark, and W.J. Ooms, Surf. Sci. **457**, L391 (2000).

104 C.R. Ashman, C.J. Först, K. Schwarz, and P.E. Blöchl, Phys. Rev. B **69**, 075309 (2004).

105 Y. Liang, S. Gan, Y. Wei, and R. Gregory, Phys. Status Solidi B **243**, 2098 (2006).

106 K.D. Fredrickson, H. Seo, and A.A. Demkov, J. Appl. Phys. **120**, 065301 (2016).

107 Y. Wei, X. Hu, Y. Liang, D.C. Jordan, B. Craigo, R. Droopad, Z. Yu, A. Demkov, J.L.E. Jr, and W.J. Ooms, J. Vac. Sci. Technol. B **20**, 1402 (2002).

108 D.M. Goodner, D.L. Marasco, A.A. Escuadro, L. Cao, and M.J. Bedzyk, Phys. Rev. B **71**, 165426 (2005).

109 L.C. Allen, J. Am. Chem. Soc. **111**, 9003 (1989).

110 C.-P. Cheng, I.-H. Hong, and T.-W. Pi, Phys. Rev. B **58**, 4066 (1998).

111 E. Pehlke and M. Scheffler, Phys. Rev. Lett. **71**, 2338 (1993).

112 L. Spiess, A.J. Freeman, and P. Soukiassian, Phys. Rev. B **50**, 2249 (1994).

113 A. Cattoni, R. Bertacco, M. Cantoni, F. Ciccacci, H. Von Kaenel, and G.J. Norga, Appl. Surf. Sci. **254**, 2720 (2008).

114 B.R. Lukanov, J.W. Reiner, F.J. Walker, C.H. Ahn, and E.I. Altman, Phys. Rev. B **84**, 075330 (2011).

115 B. Lukanov, K. Garrity, S. Ismail-Beigi, and E.I. Altman, Phys. Rev. B **85**, 195316 (2012).

116 Manufactured and supplied by Air Liquide ALOHA Electronics Performance Materials, Air Liquide Electronics U.S. LP, Houston, TX.

117 S. Rentrop, T. Moebus, B. Abendroth, R. Strohmeyer, A. Schmid, T. Weling, J. Hanzig, F. Hanzig, H. Stöcker, and D.C. Meyer, Thin Solid Films **550**, 53 (2014).

118 G. Kresse and J. Hafner, Phys. Rev. B **47**, 558 (1993).

119 G. Kresse and J. Hafner, Phys. Rev. B **49**, 14251 (1994).

120 G. Kresse and J. Furthmüller, Comput. Mater. Sci. **6**, 15 (1996).

121 G. Kresse and J. Furthmüller, Phys. Rev. B **54**, 11169 (1996).

122 P.E. Blöchl, Phys. Rev. B **50**, 17953 (1994).

123 G. Kresse and D. Joubert, Phys. Rev. B **59**, 1758 (1999).

124 J.P. Perdew and A. Zunger, Phys. Rev. B **23**, 5048 (1981).

125 J.P. Perdew, K. Burke, and M. Ernzerhof, Phys. Rev. Lett. **77**, 3865 (1996).

126 J.P. Perdew, K. Burke, and M. Ernzerhof, Phys. Rev. Lett. **78**, 1396 (1997).

127 H.J. Monkhorst and J.D. Pack, Phys. Rev. B **13**, 5188 (1976).

128 R.E. Schlier and H.E. Farnsworth, J. Chem. Phys. **30**, 917 (1959).

129 D.J. Chadi, J. Vac. Sci. Technol. **16**, 1290 (1979).

130 P. Ponath, K. Fredrickson, A.B. Posadas, Y. Ren, X. Wu, R.K. Vasudevan, M. Baris Okatan, S. Jesse, T. Aoki, M.R. McCartney, D.J. Smith, S.V. Kalinin, K. Lai, and A.A. Demkov, Nat. Commun. **6**, 6067 (2015).

131 J.H. Ngai, D.P. Kumah, C.H. Ahn, and F.J. Walker, Appl. Phys. Lett. **104**, 062905 (2014).

132 C. Merckling, G. Saint-Girons, C. Botella, G. Hollinger, M. Heyns, J. Dekoster, and M. Caymax, Appl. Phys. Lett. **98**, 092901 (2011).

133 A.D. Katnani and G. Margaritondo, Phys. Rev. B **28**, 1944 (1983).

134 W.-J. Lee, J.W. Ma, J.M. Bae, S.H. Park, M.-H. Cho, and J.P. Ahn, CrystEngComm **13**, 5204 (2011).

135 W.F. Egelhoff, Surf. Sci. Rep. **6**, 253 (1987).

136 S. Lizzit, A. Baraldi, A. Groso, K. Reuter, M.V. Ganduglia-Pirovano, C. Stampfl, M. Scheffler, M. Stichler, C. Keller, W. Wurth, and D. Menzel, Phys. Rev. B **63**, 205419 (2001).

137 J.-H. Cho, S. Jeong, and M.-H. Kang, Phys. Rev. B **50**, 17139 (1994).

138 G. Le Lay, J. Kanski, P.O. Nilsson, U.O. Karlsson, and K. Hricovini, Phys. Rev. B **45**, 6692 (1992).

139 D. J. Smith, H.-W. Wu, S. Lu, T. Aoki, P. Ponath, K. Fredrickson, M. D. McDaniel, E. Lin, A. B. Posadas, A. A. Demkov, J. G. Ekerdt, and M. R. McCartney, J. Mater. Res. **0**, 1 (2016).

140 E. Zintl and W. Dullenkopf, Z Phys Chem Abt B **16**, 183 (1932).

141 E. Zintl, Angew. Chem. **52**, 1 (1939).

142 P.W. Loscutoff and S.F. Bent, Annu. Rev. Phys. Chem. **57**, 467 (2006).

143 J.-M. Mackowski, B. Cimma, R. Pignard, P. Colardelle, and P. Laprat, Window and Dome Technologies and Materials III, SPIE 1760, (San Diego, California, American), pp. 201–209 (1992).

144 S.R. Singamaneni, J.T. Prater, and J. Narayan, Appl. Phys. Rev. **3**, 031301 (2016).

145 J.H. Ngai, K. Ahmadi-Majlan, J. Moghadam, M. Chrysler, D. Kumah, F.J. Walker, C.H. Ahn, T. Droubay, Y. Du, S.A. Chambers, M. Bowden, X. Shen, and D. Su, J. Mater. Res. **32**, 249 (2017).

146 S. Hu, E. L. Lin, A. K. Hamze, A. Posadas, H-W. Wu, D. J. Smith, A. A. Demkov, and J. G. Ekerdt, J. Chem. Phys. **146**, 052817 (2016).

147 S. Hu, A. B. Posadas, A. A. Demkov and J. G. Ekerdt, "The function of Zintl layer for atomic layer deposition on Ge (001)" in preparation, (2017).

148 M.D. McDaniel, A. Posadas, T.Q. Ngo, A. Dhamdhere, D.J. Smith, A.A. Demkov, and J.G. Ekerdt, J. Vac. Sci. Technol. A **31**, 01A136 (2013).

149 K. Martens, C.O. Chui, G. Brammertz, B.D. Jaeger, D. Kuzum, M. Meuris, M. Heyns, T. Krishnamohan, K. Saraswat, H.E. Maes, and G. Groeseneken, IEEE Trans. Electron Devices **55**, 547 (2008).

150 D.K. Schroder, Semiconductor Material and Device Characterization (John Wiley & Sons, 2006).

151 K. Saraswat, D. Kim, T. Krishnamohan, D. Kuzum, A.K. Okyay, A. Pethe, and H.-Y. Yu, ECS Trans. **16**, 3 (2008).

152 C.O. Chui, H. Kim, D. Chi, B.B. Triplett, P.C. McIntyre, and K.C. Saraswat, in Dig. Int. Electron Devices Meet. pp. 437–440 (2002).

153 K. Shibuya, T. Ohnishi, M. Lippmaa, M. Kawasaki, and H. Koinuma, Appl. Phys. Lett. **84**, 2142 (2004).

Vita

Shen Hu was born and raised in Luzhou, Sichuan province of China. He went to Tianjin University to study Chemical Engineering from 2010 to 2014 and graduated with bachelor degree. He went to the McKetta Department of Chemical Engineering in the University of Texas at Austin to pursue Ph. D. degree and meanwhile joined Prof. John G. Ekerdt's research group in the Fall of 2014.

Then he started his research project on epitaxial crystalline perovskites growth on Ge (001) by atomic layer deposition. Since Shen Joined Ekerdt's group, to-date he has published six authored and co-authored journal articles (2 first-author and 4 co-author). And there are two more first-authored articles in preparation. Shen had his internship at Micron technology Inc. Boise, ID in the Fall of 2017 and worked as CVD/Diffusion process engineer.

Permanent address: hushentj@gmail.com

This dissertation was typed by Shen Hu